History matching hydromechanical models using time-lapse seismic time-shifts

David Charles Price

Department of Earth and Enivronment

University of Leeds

Submitted in accordance with the requirements for the degree of

Doctor of Philosophy

29th March 2018

The candidate confirms that the work submitted is his own and that appropriate credit has been given where reference has been made to the work of others.

'I have not failed. I've just found 10,000 ways that won't work'
Thomas A. Edison

Acknowledgements

In some ways a Ph.D. can be considered somewhat similar to cycling in Yorkshire. The journey is far from flat, straight or easy to navigate. The thrill of overcoming one obstacle never failing to be contrasted by a subsequent uphill struggle or wrong direction. Despite all this, the journey as a whole leaves you with a remarkable sense of achievement.

Throughout my Ph.D. journey I have been extremely fortunate to have had such wonderful supervisors. Without their support and guidance this work would not have been possible. To Professor Quentin Fisher and Dr. Doug Angus goes a large thank you, your help has been greatly appreciated. I hope my research has made your invested time worthwhile.

I would also like to thank TOTAL and the Earth and Environment department at the University of Leeds for funding my research. A special thank you must go to TOTAL for giving me the opportunity of completing an internship. Those four months provided me with such a great platform in which to build this research. My time in Scotland will always be remembered as an enjoyable one.

A personal thank you must go to Alejandro Garcia. Without your willingness to help and share your expertise, I would not have been able to produce this work. I have been lucky for you to have been involved in my project and your help has not gone unnoticed.

A special thank you must also go to Rockfield Software limited for proving me with a license to their modelling software ELFEN. The Wolfson multiphase flow laboratory must also get a thank you for providing me with such a great array of core data.

I don't think I could finish this Ph.D. without mentioning Dr Roger Clark, who, without his gamble of offering me a place on his Masters course, I would not have been where I am today. I will always be grateful to him for proving me with that opportunity.

Finally, how can I finish my acknowledgements without thanking my friends and family. Without the mental, physical and financial support of my family I would not have had the great academic opportunities in which I have been so luckily to have had and would not be where I am today. Thanks must also go to my friends as I am not sure I would have made it through these four years without the booze and banter. Last but not least, I would like to thank my partner Hannah for her constant support.

Abstract

Although time-lapse seismic data has been used to great success in the history matching of reservoir fluid properties (i.e. saturation in reservoir simulators), it has been used far less effectively for benchmarking geomechanical behaviour. The reason for this is twofold. Firstly, hydromechanical models are typically large, complex and highly nonlinear with considerably large runtimes. Secondly, isolating and extracting quantifiable mechanical information from seismic data is difficult. However, by not attempting to utilise numerical history matching techniques, are we making the most out of the geomechanical information stored in time-lapse seismic data?

In this Thesis I have attempted to answer this question by conducting a synthetic history matching study. I generate a hydromechanical model of a typical high pressure high temperature production scenario in the North Sea and utilise seismic history matching in an attempt to constrain the properties of the overburden and improve the models predictive capabilities. The study focuses primarily on overburden calibration as overburden time-shifts are not complicated by fluid effects, as in the reservoir, and hence can be considered as a purely geomechanical effect. Also the matching process is attempted utilising only a small, feasible number of model perturbations.

Before seismic history matching can be successfully attempted it is important to have an in depth working knowledge of the model behaviour. Therefore, I conduct a multi method Global Sensitivity Analysis (GSA) on over 4000 model perturbations, to evaluate the potential geomechanical information content of seismic time-shifts. Specifically, which model parameters cause the majority of the variation to overburden time-shifts. The results show that the majority of the variation in modelled shifts can be attributed to the Young's Modulus and Biot coefficient. These parameters appear the most influential for both near-offset time-shifts and the time-shift offset behaviour. However, the Poisson's ratio also becomes influential when considering the time-shift offset behaviour at long offsets. The results of the GSA also highlight that the over-parametrisation of material properties in the model can lead to unnecessary complexity in the model space. The simplification of complex rock properties (i.e. simplification of nonlinear relationships to single constants) will not significantly affect model performance whilst making seismic history matching more achievable.

A robust history matching study also requires the consideration of all forms of uncertainty. One of the main causes of uncertainty in the process is that of the relationship between effective stress and seismic velocity i.e. the rock physics model. I analyse a handful of the most popular rock physics models and assess their behaviour and stability when applied to a large dry core dataset of different lithologies. The results show that most

models are robust, well constrained and do a suitably good job at fitting velocity-stress data taken from core samples in a laboratory environment. However, slight discrepancies between different model approximations for the same core sample can cause significantly different time-lapse velocity predictions. The results also show that models are difficult to parameterise without the availability of velocity-stress core data. Attempting to do so can lead to even greater discrepancies in their time-lapse velocity predictions. The results also support the current belief that the velocity-stress core data may not be a good representation of the velocity-stress dependence of the subsurface

I utilise an iterative emulator based approach to history matching which makes it possible to perform a robust history match with a small number of model realisations. I utilise the results of the GSA to define the model parameters in which to focus the history match and also utilise the results of the rock physics model analysis to define suitable uncertainties. The results of the emulation process show it is possible to perform a successful history match utilising only a small number of model perturbations and to constrain the uncertainty in the most influential model parameters. The process is improved significantly when both near-offset time-shifts and the time-shift offset behaviour are considered simultaneously in the matching process. It becomes apparent that the matching process and hence final solution is limited by the number of model realisations, iterations and the extent of the available seismic data. The greater the number of realisations, the more accurate the emulators whilst the more seismic observations, the more data available in which to test predicted models. Also, it becomes increasingly clear that the uncertainty in rock physics modelling dominates the matching process. Taking into consideration it's uncertainty makes it extremely difficult to confidently constrain any properties of the hydromechanical model from time-lapse seismic data. It becomes increasingly apparent that there is a great need to improve our understanding of rock behaviour (i.e. rock physics) before the seismic history matching of mechanical behavior becomes suitably accurate and economically appealing.

Contents

Foreword

During the course of my Ph.D. I have written - and subsequently published - a number of journal articles and expanded abstracts. When considering how to structure my thesis, I considered an alternative style where these published articles are assembled together with an introduction and a conclusion. However, I personally feel that it is extremely difficult to narrate a thesis of this alternative style, and thus difficult to ensure that the reader feels as though they are reading a coherent document. By writing a classic style thesis I am able to create a more free-flowing document. I am able to expand on points that can often be otherwise written as passing comments in journal articles, and can also include additional work that I feel is relevant to the story of my research.

Below I have included a list of my Journal articles and expanded abstracts, many of which follow the work included in this thesis. I also include all co-authored material and the publication of my Masters degree thesis, as these have also been an integral part of my academic achievements during my Ph.D.

Journal Articles

- **Price D. C.**, Angus D. A., Garcia, A & Fisher, Q. J. 2017. A multi-method global sensitivity analysis to aid the calibration of geomechanical models via time-lapse seismic data. *Geophysical Journal International*, **2012**(3), 2031-2046.
- **Price D. C.**, Angus D. A., Garcia, A & Fisher, Q. J. 2017. Probabilistic analysis and comparison of stress-dependant rock physics models. *Geophysical Journal International*, **2010**, 196-209.
- **Price D. C.**, Angus D. A., Chambers, K & Jones G. 2015. Surface microseismic imaging in the presence of high-velocity lithological layers. *Geophysicsl*, **80**, WC117-WC131.

Conference Abstracts

- Parsons, S., Stuart, G. & **Price D. C**., 2018. Global sensitivity analysis on thermo-hydro-mechanical coupled processes in a low strength sedimentary rock. *Eurorock Conference*, Saint Petersburg.
- Saleh, H., Fisher, Q., **Price D. C.** & Angus D.A. 2017. Trends in micro-crack properties of sedimentary rocks in loading and unloading mechanism: Dry-core velocity-stress measurements. *4th EAGE workshop on Rock Physics*, Abu Dhabi.

- **Price D**. C. & Fisher, Q. 2017. Why you should take caution in using rock physics model approximations for time-lapse analysis. *79th EAGE Conference & Exhibition*, Paris.
- **Price, D**., Parsons, S. & Angus, D.A. 2016. Sensitivity analysis of a 4D geomechanical model for time-lapse seismic calibration. *86th SEG Conference & Exhibition, Houston.*
- **Price, D**., Parsons, S. & Angus, D.A. 2016. Analysis of uncertainty in seismic geomechanics workflow: towards 4D seismic calibration of 4D geomechanical models. *EAGE/SPE Workshop on Integrated Geomechanics in E&P, Abu Dhabi.*
- Angus, D., **Price, D**., Herwanger, J., Verdon, J. & Bissel, R. 2016. Assessing uncertainty in 4D seismic monitoring: application of seismic geomechanical models to several CCS pilot sites. *IEAGHG Monitoring and Modelling Research Network Combined Meeting*, Edinburgh.
- **Price, D**. & Angus, D.A. 2016. Probabilistic comparison of stress dependent rock physics models. *78th EAGE Conference & Exhibition, Vienna.*
- **Price, D**. Angus, D.A., Chambers, K. & Jones, G. 2015. Surface microseismic imaging-influence of high velocity layers. *77th EAGE Conference & Exhibition.*

List of Symbols

Below is a table that lists the frequently used mathematical sysmbols in this thesis. Other symbols, less frequently used, are defined in the text. Occasionally, the same symbol is used to represent different parameters. To which parameters a symbol is representing is made clear when used in the text.

Symbol	Nomenclature	Symbol	Nomenclature
σ	Direct stress/Standard deviation	q	Deviatoric stress
σ'	Effective stress	p	Effective mean stress
τ	Shear stress	P_p	Pore pressure
R	R-factor	t	Two-way travel time
V	P-wave velocity (unless stated otherwise)	Δt	Time-lapse time-shift (monitor − base)
$d\Delta t/dX$	Rate of change of time-shift with offset	$\Delta t/t$	Time-strain
ε	Strain /Thomsen parameter	ε_{zz}	Fractional change in layer thickness
ϕ	Porosity	K	Intrinsic permeability
ϵ	Experimental error	δ	Model discrepancy error
ξ	Observation i.e. data	ρ_g	Grain density
ρ_f	Fluid density	ρ	Bulk density
ν	Poisson's ratio	E	Young's Modulus
λ	Cam Clay constant	κ	Cam Clay constant
α	Biot coefficient	K_{xy}	Vertical-horizontal stress coefficient

List of Figures

List of Tables

1 . Introduction

No great discovery was ever made without a bold guess.
Sir Isaac Newton

1.1 Compacting Reservoirs

The production of hydrocarbons reduces the pore pressure within a subsurface reservoir. As a result, the reservoir compacts under the weight of the overlying sediment. This decrease in reservoir thickness causes the re-accommodation of the subsurface stress field and the deformation (i.e. straining) of the surrounding rock mass. This deformation can sometimes result in significant surface subsidence. Production induced compaction and surface subsidence have been reported in many reservoirs around the world from Southeast Asia (e.g. van Ditzhuijzen *et al.*, 1984) to the Gulf of Mexico (e.g. Rickett *et al.*, 2006). The consequences of which have often been far from favourable.

One of the most widely recognised and reported cases is that of the Ekofisk reservoir in the Norwegian sector of the North Sea. After approximately 14 years of production (from 1971 to 1985) the platform was recorded to be sitting at around 2.5 meters deeper in the water. After an investigation it became clear that the seabed was sinking at a rate of up to 50cm per year (Kvendseth, 1988), far surpassing any previous estimates (e.g. Sulak & Danielsen, 1988). This surprising rate of subsidence had a detrimental effect on the integrity of the platform. Remediation consisted of lifting and re-securing the platform which had large economic implications for Phillips Petroleum Co, who were operating the field at the time. Other subsidence cases include the Goose Creek field in Texas and the Groningen field of the Netherland, where subsidences on the order of tens of centimetres (Nagel, 2001) caused significant flooding due to low lying land.

As well as surface subsidence, production induced changes to the subsurface stress field can induce other mechanical effects that can cause significant challenges. For example: 1) Reduction in the reservoir permeability due to pore collapse can hinder the flow of hydrocarbons (e.g. Marek, 1979), 2) fracturing of the caprock and fault reactivation can induce hydrocarbon migration and compartmentalization (e.g. Munns, 1985; Wiprut & Zoback, 2000) and 3) bedding parallel slip, and overburden extension can result in well failure (e.g. Bruno, 2002; Dusseault *et al.*, 1998). Figure 1.1 depicts some of these issues. The mechanical effects induced in the overburden are a result of what is known as stress arching. This occurs when the compacting reservoir causes the vertical extension of the overburden with maximum displacement occurring directly above the reservoir. As a result, most of the load is redistributed to the flanks. This significantly reduces the vertical

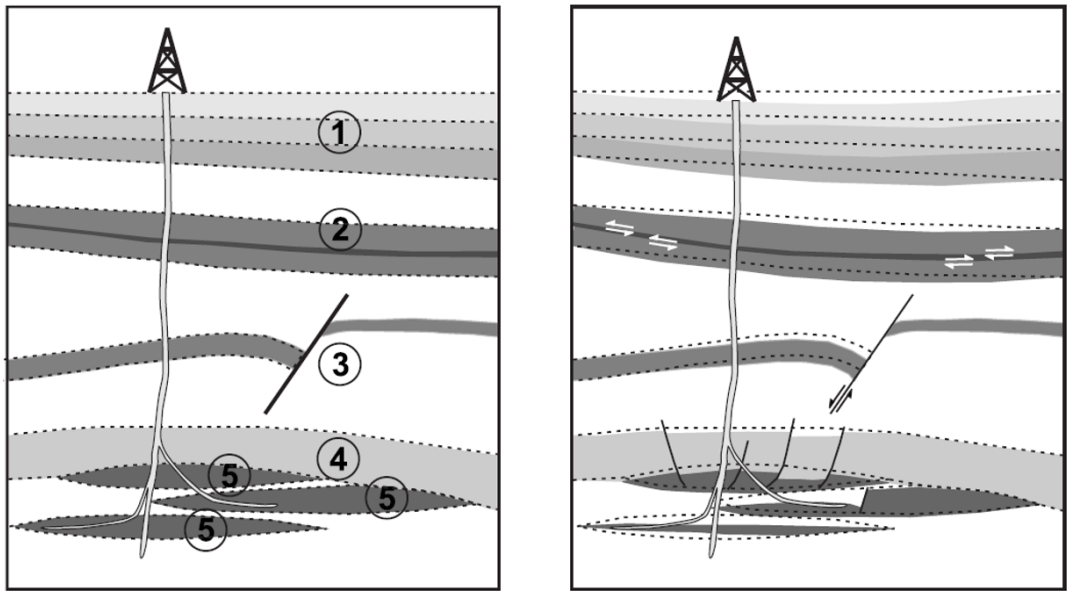

Figure 1.1: Herwanger *et al.* (2009). Sketch of the mechanical consequences of production. The left image shows the subsurface in its pre-production state whilst the right image after substantial production. Production can cause (1) surface subsidence, (2) bedding parallel slip, (3) fault reactivation, (4) breach of seal integrity and (5) reservoir compaction.

stress directly above the reservoir whilst it simultaneously increases at the reservoir flanks. The horizontal stress on the other hand increases above the reservoir whilst decreasing at the flanks. The shear stress also increases within the overburden which can result in the possible (re)activation of faults and shearing along bedding planes. If the change in stresss are large enough, fault (re)activation can be exacerbated by localised changes to the faulting regime (i.e. from a reverse faulting regime where the horizontal stress is greater than the vertical, to a normal faulting regime where the vertical stress is greater than the horizontal). Stress arching is shown schematically in Figure 1.2.

1.2 Hydromechanical Modelling

The mechanical implications associated with compacting reservoirs has made geomechanical modelling an essential reservoir monitoring tool. Understanding and anticipating the spatial changes to the *in situ* stress field can aid production (i.e. predict the migration of fluids), help maintain well and platform integrity and help prevent environmental complications.

A standalone geomechanical model describes the *in situ* subsurface stress state. This essentially depends on three things (Herwanger *et al.* (2009), e.g. Figure 1.3):

1. Subsurface structure: *Reservoir and overburden geometry, fault location and orien-*

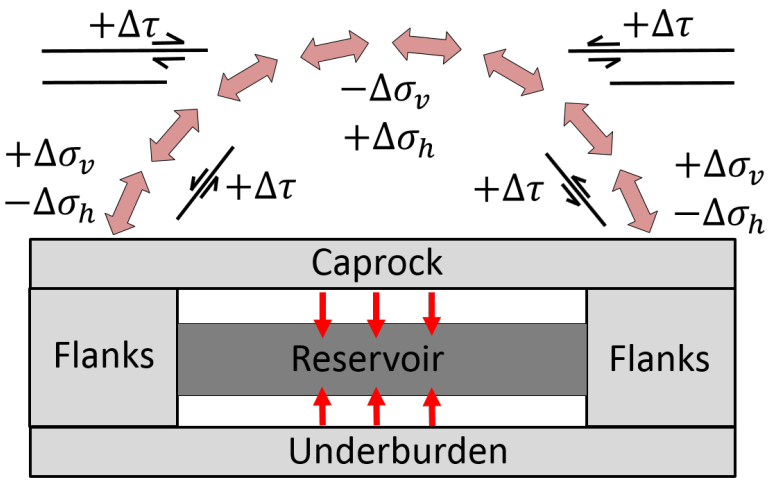

Figure 1.2: Schematics example of production induced stress arching. The compaction of the reservoir causes the vertical extension of the overburden and the re-distribution of the load to the reservoir flanks. As a result, there is a significant reduction in the vertical stress σ_v directly above the reservoir whilst an increase in σ_v at its flanks. The horizontal stress σ_h on the other hand, increase above the reservoir, as the rock falls in on itself, whilst decreasing at the flanks. This also causes an increase in shear stress τ which can cause bedding parallel slip.

tation.

2. Distribution of material properties: *Elastic and strength properties of the rocks.*

3. External stresses: *Overburden stresses, tectonic stresses, pore pressure.*

The simulation will account for each of these three factors simultaneously and calculate the *in situ* (i.e. present day) subsurface stress state.

Modelling production induced changes to this stress field requires the coupling of the geomechanical model to a reservoir simulator (e.g. De Gennaro *et al.*, 2008; Minkoff *et al.*, 2003; Samier *et al.*, 2003). The coupled model allows the modelling of pore pressure and saturation change within the reservoir (in the fluid domain) whilst additionally simulating change in stress and strain (in the mechanical domain) to the reservoir and surrounding rock mass. The physics describing fluid flow and geomechanics are interrelated. Variations in pore pressure (fluid domain) will induce a stress change (mechanical domain), whilst a change in stress can lead to changes in permeability and porosity (fluid domain). Neglecting this mutual feedback can lead to inaccurate modelling results (e.g. Dean *et al.*, 2006; Minkoff *et al.*, 2004). The coupled dynamic simulator is often referred to as a 4-D geomechanical model. However, for the purpose of this Thesis, I refer to it as a hydromechanical model.

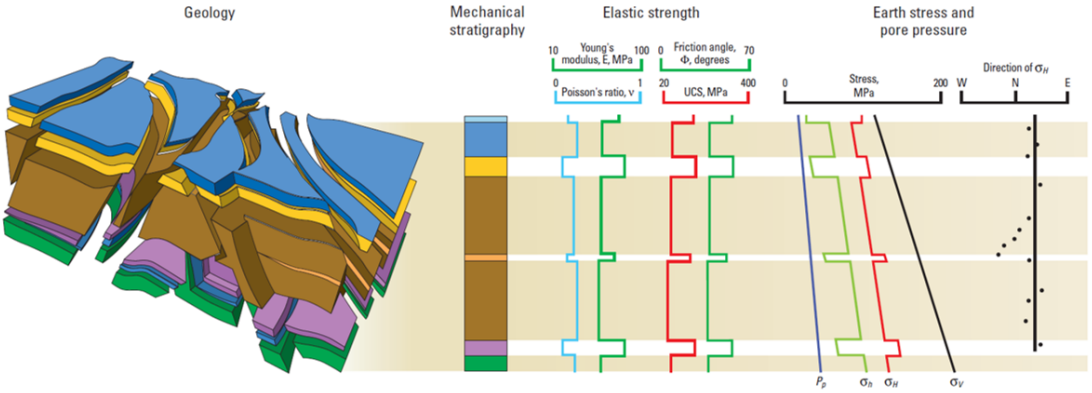

Figure 1.3: Ali *et al.* (2003). Concept of constructing a geomechanical model. Detailed knowledge of the mechanical stratigraphy is required along with each unit's mechanical properties (i.e. elastic and strength properties). These are then used to predict the pore pressure and *in situ* stress state.

1.3 Monitoring Compacting Reservoirs with Time-lapse Seismic

Production induced changes in stress, strain, fluid saturation, pore pressure and temperature alter the arrival time and amplitude of seismic reflections. These changes can be monitored by taking repeat (i.e. monitor) seismic surveys throughout production and comparing the data to a pre-production (i.e. base) seismic survey. This process is typically referred to as time-lapse (4-D) seismic monitoring. Originally, time-lapse seismic was intended to be used solely as a reservoir monitoring tool. The recorded changes in reflection amplitude (i.e. changes in velocity and density) being a direct indicator of fluid saturation. The first recorded case of time-lapse seismic being used for this purpose was that of Greaves & Fulp (2001). They successfully managed to produce seismic amplitude difference volumes to monitor and map gas saturation within a reservoir during production.

The geomechanical information stored within time-lapse seismic (i.e. changes in stress and strain) were not exploited till Guilbot & Smith (2002) published their study on Ekofisk. They were the first to isolate and measure differences in reflection arrival times (i.e. time-shifts) and use them to estimate the magnitude of compaction. Previously, observed time-shifts were considered a direct consequence of poor repeatability with the inability to accurately reposition sources and receivers being responsible for travel time differences. Since Guilbot & Smith (2002), many more cases of compaction related time-shifts followed in quick succession (e.g. Hawkins *et al.*, 2007; Staples *et al.*, 2007a; Tura *et al.*, 2005).

Time-lapse time-shifts are caused by a combination of changes to seismic velocities and raypath length as shown in Figure 1.4. Considering vertical wave propagation, Landrø&

Stammeijer (2004) expressed the fractional change in travel-time t across a layer (referred to as the time-strain) as the difference between the fractional change in path length z and P-wave velocity V,

$$\frac{\Delta t}{t} = \frac{\Delta z}{z} - \frac{\Delta V}{V} = \varepsilon_{zz} - \frac{\Delta V}{V}. \tag{1.1}$$

In geomechanical terms, the fractional change in path length is equivalent to the average vertical strain over the layer ε_{zz}. After collating several time-lapse seismic datasets from different fields around the world, Hatchel & Bourne (2005) propose a simple linear model relating the fractional change in velocity to the average vertical strain,

$$\frac{\Delta V}{V} = -R\varepsilon_{zz}. \tag{1.2}$$

The dimensionless parameter R denotes the ratio in which travel time changes are affected by changes in V and z. The total change in P-wave travel time over a finite sequence of layers is then,

$$\Delta t = \int_0^z (1+R)\frac{\varepsilon_{zz}}{V} dz. \tag{1.3}$$

From their study, Hatchel & Bourne (2005) proposed typical R values of between 1 to 6. However, values as high as 50 have been documented in literature (e.g. Garcia *et al.*, 2010; Staples *et al.*, 2007a).

It is well understood that V increases with stress (e.g. Nur & Simmons, 1969). Therefore, in the reservoir, compaction results in a decrease in raypath length whilst an increase in velocity and hence the travel times across the reservoir in the monitor survey are less than those of the base. For the purpose of this Thesis I refer to this scenario as generating negative time-shifts Δt. (i.e. monitor − base). Whereas in the overburden and underburden, extension causes an increase in ray path length and a reduction in velocity, hence positive Δt (e.g. Figure 1.4). However, depending on the magnitude of the stress arching, negative shifts are possible in the overburden at the flanks of the reservoir.

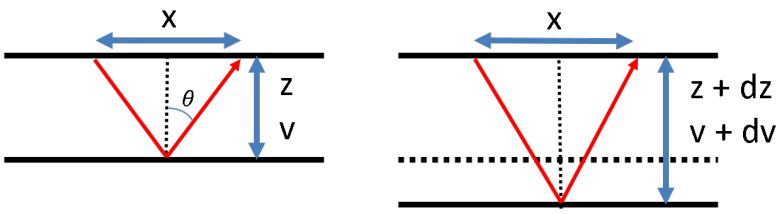

Figure 1.4: Seismic raypaths across an overburden layer for the base (left) and monitor (right) survey. Re-drawn after Landrø& Stammeijer (2004).

Considering reservoir compaction causes triaxial stress change (e.g. Figure 1.2) it is reasonable to assume that time-shifts are offset dependant. This offset dependence is illustrated in Figure 1.5. In the overburden, directly above the reservoir, a decrease in vertical stress and an increase in horizontal stress causes anisotropic velocity changes. Specifically, an increase in horizontal velocity and a decrease in the vertical velocity. As offset increases and the raypaths become more horizontal, the greater the influence of the horizontal velocity. This generates a more elliptical wavefront as seen in Figure 1.5. Consequently, time-shifts are expected to decrease (i.e. get less negative) with offset, a behaviour indeed observed in certain time-lapse seismic datasets (e.g. Hawkins, 2008; Herwanger *et al.*, 2007).

In the reservoir, the stress changes are compressive in all directions (e.g. Figure 1.5), hence all propagation directions experience an increase in velocity. Therefore, the time-shifts differ with offset depending on the magnitude of each compressive stress change. Typically, in the reservoir the vertical velocity increase is larger than the horizontal and hence a similar reduction in time-shift is observed with offset.

The magnitude and direction of the produced anisotropy is typically defined in terms of the Thomsen Parameter ε (Thomsen, 1986). It describes the difference between the horizontal and vertical P-wave velocities. In the overburden, the increase in horizontal velocity and a decrease in vertical velocity generates a positive $\Delta\varepsilon$. The reservoir on the other hand experiences a decrease in $\Delta\varepsilon$, assuming the increase in vertical velocity is greater than the horizontal. The magnitude of $\Delta\varepsilon$ describes the extent of the induced anisotropy.

Rodriguez-Herrera *et al.* (2015) explained the time-shift offset dependency through extending the normal incidence model of Hatchel & Bourne (2005). They generalize the model such that the velocity change depends upon the strain component along the ray path ε_{pp},

$$\Delta t = \frac{1}{V_0 cos(\theta)} \int_{z_1}^{z_2} (cos^2(\theta)\varepsilon_{zz} + R\varepsilon_{pp})dz. \tag{1.4}$$

In this equation, θ defines the angle of incidence (shown in Figure 1.4) and V_0 the base survey velocity. As a result, the shift vs offset behaviour can be used as an additional form of geomechanical information.

In the overburden, the production induced change in seismic velocity can be attributed to purely geomechanical effects. The fractional change in velocity related to fractional change in stress. However, inside the reservoir the changes in velocity are a combined effect of both geomechanical and fluid effects. Changes in fluid saturation, pore pressure and temperature all contribute to the velocity change. This makes it extremely difficult to

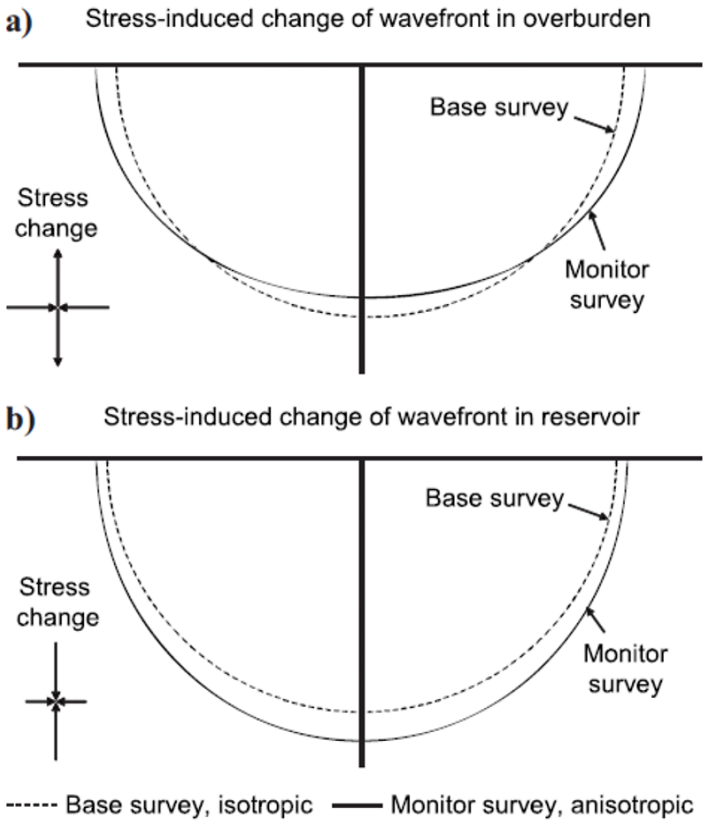

Figure 1.5: Herwanger *et al.* (2009). Typical wavefront for base and monitor surveys in (a) the overburden just above the reservoir, and (b) inside the reservoir. In the reservoir, the stress change is compressive in all directions and hence the velocity increases in every direction. The overburden on the other hand experiences compressive horizontal stress change whilst tensional vertical stress change, hence an increase in horizontal velocity and a decrease in vertical velocity.

isolate the exact contribution of each effect to the observed time-lapse seismic time-shifts within the reservoir.

1.4 History Matching Hydromechanical Models

Hydromechanical models (like any other model) need to be benchmarked with field observations. Without observations there can be no way to determine if the model is successful and providing accurate predictions of future behaviour. History matching can be considered as a form of model benchmarking, where the model is adjusted such that it closely reproduces a set of historical observations. Therefore, geophysically monitoring a reservoir through production can provide essential information with which to history match a hydromechanical model. One of the most attractive geophysical monitoring methods is time-lapse seismic. Its ability to observe production related fluid and geomechanical

changes outside of the localised well regions makes it an ideal monitoring tool for field wide history matching.

To implement a reliable history match it is important to understand the relationship between a complex computer simulator and the physical system. This relationship can be generalised via a simple relationship, as expressed by Vernon *et al.* (e.g. 2010). Consider a set of physical observations ξ. The relationship between these observations and the true values of the system y can be expressed as:

$$\xi = y + \epsilon, \tag{1.5}$$

where ϵ is the *experimental error* assumed to be uncorrelated with y.

The computer simulator can be considered as a function which maps the inputs x to the outputs $f(x)$. However, if we input the true physical properties of the system x^* we would not expect our computer simulator $f(x^*)$ to reproduce the true physical system y perfectly. Although complex computer models are highly sophisticated, mathematical simplifications and various assumptions mean that we would still expect a slight discrepancy between $f(x^*)$ and y:

$$y = f(x^*) + \delta, \tag{1.6}$$

where δ represents a *model discrepancy error* which is assumed to be uncorrelated with $f(x^*)$. Note that this error is typically difficult to quantify and may have a complicated covariance structure across different outputs.

History matching a computer simulator can be more specifically defined as the process of identifying a set of simulator input values x such that its output $f(x)$ gives an acceptable match to a set of historical observations ξ given ϵ and δ. Attaining an acceptable match between model and system does not mean that the set of inputs x are the true physical properties of the system x^*. It means that these inputs produce acceptable outputs $f(x)$ that are within a given tolerance. It should also be noted that history matching may lead to the conclusion that there are no, or many, acceptable matches between model and observation. A conclusion that there are no acceptable matches is one of great interest. It means that there are possible fundamental flaws in the science of the simulator which might require addressing. Therefore, history matching can be considered a form of model evaluation in which it is determined if a match is achievable and within what regions of the input space are acceptable matches located. If an optimum set of inputs x is desired (i.e. model calibration), then it is good practice to first implement a history match to authenticate the process and reduce the model space in which you perform the final calibration.

History matching has been used extensively in industry on reservoir simulators to match production and pressure observations at wells (e.g. Ballester & Carter., 2007; Craig *et al.*, 1997). Time-lapse seismic data, in particular time-lapse amplitude changes, have also been successfully incorporated into the matching process to monitor reservoir saturation change (e.g. Emerick & Reynolds, 2012; Gosselin *et al.*, 2003; Staples *et al.*, 2005).

1.5 Thesis Overview

Although time-lapse seismic data has been used to great success in the history matching of reservoir fluid properties (i.e. saturation), it has been used far less effectively for benchmarking geomechanical behaviour. In industry, the most widely employed use of overburden time-shift data is for the visual (i.e. qualitative) inspection of the models behaviour. It is used primarily as a subsidiary indicator to highlight any large discrepancies between model prediction and observed data (e.g. De Gennaro *et al.*, 2008, 2010; Hatchel & Bourne, 2005; Herwanger *et al.*, 2010). This is because, geomechanical models are often large, complex and highly nonlinear with long computational runtimes. Therefore, running a large number of models, typically required for history matching, is generally unfeasible. Also, isolating and extracting meaningful mechanical information from time-shift data is difficult. However, by not attempting to utilise numerical history matching techniques, are we making the most out of the geomechanical information stored in time-lapse seismic data?

In this study I aim to assess the potential closer integration of time-lapse seismic data with hydromechanical models. Specifically, the process of history matching geomechanical properties using time-lapse seismic time-shifts. The main focus of this study will be on overburden behaviour as its production induced time-shifts are not complicated by fluid effects as is the case within the reservoir. These seismic anomalies can be classed as a purely mechanical effect. However, the mechanical properties, and hence behaviour, of the overburden is often as unknown as those of the reservoir rock whilst being considered to be equally as important. A suitable example of this being the uncertain mechanical properties of overburden chalks seen in North Sea reservoirs. Monitoring and forecasting changes to the overburden stress field during production is essential for predicting the future integrity of platforms (i.e. surface subsidence) and the possibility of well failure (e.g. Bruno, 2002; Vudovich *et al.*, 1989). The information is also vitally important during the planned drilling of new wells.

In this Thesis, I generate a synthetic production scenario whereby I assume that the mechanical properties of the overburden are greatly uncertain. As a result, the influence of production on the integrity of the production well is assumed to be virtually unknown. I develop a hydromechanical model of the reservoir to model production and utilise seismic

history matching in an attempt to improve the models prediction of the stress and strain (i.e. subsidence) change along the production well. Specifically, I choose a High Pressure High Temperature (HPHT) production scenario in the North Sea. In the model I place multiple thick layers of chalk into the overburden whose mechanical properties are assumed vastly uncertain. I then attempt to history match the mechanical properties of these chalks using time-lapse seismic time-shifts. As this Thesis focuses on a synthetic scenario, the time-lapse seismic data is forward modelled directly from an original (i.e. truth) case scenario via a simple raytracing methodology. As this study will use a large number of model perturbations to statistically study seismic history matching, the model is reduced to two dimensions (2-D). This greatly reduces its runtime by orders of magnitude and allows for an in depth statistical investigation into seismic history matching. However, this study does take into consideration the application of conducting such a history match on more computationally expensive 3-D scenarios.

1.5.1 Thesis Outline

In Chapter 2 I describe, in detail, the process of creating my synthetic hydromechanical model of a North Sea HPHT reservoir. I describe the procedure of characterising material properties and the optimization of the numerical method used for simulation. I also describe how each step in the process is typically carried out in industry and discuss potential ambiguous procedures that can give rise to large uncertainties. I also describe the process of forward modelling seismic time-shifts and validate the results by comparing them to other North Sea HPHT scenarios published in literature.

Before history matching is attempted it is important to have an in-depth working knowledge of the models behaviour. To investigate this, I utilise over 4000 model perturbations to undertake a Global Sensitivity Analysis (GSA). The results of the GSA are shown and discussed in Chapter 3. I use the GSA to examine the sensitivity of overburden time-shifts to various overburden mechanical properties. The results of which allow me to gain an initial insight into the complexity of the model space and to highlight influential parameters which will most likely be the main focus of the history match. It also provides an insight into the most beneficial times for acquiring monitor surveys.

As discussed in Section 1.4, for a robust history match it is important to consider all forms of error and uncertainty. The two main sources of error are the experimental error ϵ and the model discrepancy error δ. A large proportion of δ can be associated with the uncertain relationship between effective stress and seismic velocity expressed via a rock physics model. An inaccurate rock physics model can cause large discrepancies between the model output and the recorded seismic data. In Chapter 4 I explore rock physics modelling in greater detail. I assess the behaviour and stability of different models when applied to

laboratory measurements of a large core dataset and compare their time-lapse velocity predictions when subject to my HPHT production scenario. It should be noted that in this study the seismic data used in the history matching is forward modelled directly from the model results. Therefore, throughout this Thesis I assume there is no experimental error i.e. ϵ=0. However, in reality this is not the case, as poor seismic repeatability can cause significant experiment error. When analysing the results of the history match, it is made sure that the potential implications of ϵ are considered and discussed.

In Chapters 5 I perform a seismic history match using an iterative emulation approach. I take the results of the GSA to describe a suitable model space and time-shift data matrix (forward modelled from a truth case scenario), and attempt to history match the mechanical properties of the overburden chalks whilst considering a suitable δ derived from Chapter 4. Utilising the history matching results I then make a final model calibration and assess its predictive capabilities by analysing the geomechanical changes along the production well.

Finally, in Chapter 6, I present the main conclusions of this Thesis. I discuss the feasibility and potential economic benefits of mechanical seismic history matching paying particular attention to its potential usefulness in improving well and platform integrity. I also outline the novelty of this work and discuss potential avenues for interesting further research.

2 . Creating a Hydromechanical Model

Essentially, All models are wrong, but some are useful
George E. P. Box

2.1 Introduction

In this chapter I use the Finite Element (FE) software ELFEN (Rockfield Software Ltd) to create a synthetic hydromechanical model of a High Pressure High Temperature (HPHT) reservoir in the North Sea. The large production related compaction associated with HPHT scenarios create significant time-lapse seismic anomalies (e.g. Guilbot & Smith, 2002). This renders it an ideal scenario in which to focus this history matching feasibility study. The North Sea is chosen as a location due its hydrocarbon reservoirs and their production related effects (geomechanical and seismic) being well documented in literature (e.g. Hansen *et al.*, 2009; Staples *et al.*, 2007a). As this study will use a large number of model perturbations to perform an in depth analysis of seismic history matching, the model must be able to generate suitably accurate results within a reasonable timeframe.

Throughout this chapter I outline the process of creating the synthetic hydromechanical model. I discuss, in detail, its parameterisation and how certain properties are derived from different forms of data. I provide a 20 year production schedule and model production related geomechanical effects and associated seismic time-shifts. I finally compare the results to other HPHT reservoirs in the North Sea to validate my synthetic production scenario.

2.2 Numerical Modelling Software

To create a hydromechanical model requires both a reservoir and geomechanical simulator (see Chapter 1). Many reservoir and geomechanical simulators are available. Typically, contrasting software packages differ by the numerical methods they use for the simulation. Choosing the right programme and numerical method is problem specific. The required precision of the output, problem complexity (e.g. number of fractures, size of model domain etc.) and time/budget constraints, will all affect which numerical scheme, and hence software, is most appropriate.

The most common numerical method used in the hydrocarbon industry for geomechanical problems is that of a continuum method. Of this method, the Finite Element

(FE) technique is the most widely used due to its flexibility and relative computational efficiency (e.g. De Gennaro *et al.*, 2010; Hawkins *et al.*, 2007; Herwanger *et al.*, 2009). However, other numerical methods, such as the discrete method, have also been used to great success (e.g. Alassi, 2008). For an excellent introduction into the most commonly used numerical methods for rock mechanics the reader is directed to the review paper of Jing & Hudson (2002).

In regards to the reservoir simulator, continuum methods are also commonly used but Finite Difference (FD) techniques are most popular. FD techniques are used due to their ease of application and their compatibility with 3-D multiphase (i.e. simultaneous flow of oil, water and gas) flow problems (e.g. Kasiri & Bashiri, 2010). However, FE and Finite Volume (FV) numerical techniques for modelling fluid dynamics also exist and have been successfully applied to production scenarios (e.g. Jackson *et al.*, 2015). For an introduction to different numerical techniques for reservoir simulation the reader is directed to the book of Iske & Randen (2006).

To create a hydromechanical model and simulate production related geomechanical effects requires the coupling of the reservoir simulator to a geomechanical solver. Typically, a modular approach is used in which the physical equations governing fluid flow and geomechanics are solved independently and information passed between the two. The popularity of this approach is due to the flexibility of using pre-existing, standalone fluid flow and geomechanical solvers. However, fully coupled methods have also been developed in which the physical equations of the two domains are solved simultaneously under one formulation. For this approach, the reservoir simulator and geomechanical solver must be integrated into the same platform. Each method of coupling has its advantage and disadvantages and thus choosing the right coupling scheme is problem dependant. Dean *et al.* (2006) and Settari & Walters (2001) discuss these two different coupling methods in greater detail. Generally the choice of coupling scheme is heavily dependent upon which programs and software packages you have available.

For this Thesis I use the FE software ELFEN (Rockfield Software Ltd) and utilize its single phase reservoir simulator to create my hydromechanical model. Both the modelling of fluid flow and mechanical behaviour in ELFEN is discretized via an FE approach. Although both fluid and geomechanical solvers are integrated into the same software package, hydromechanical coupling in ELFEN is conducted via an explicit modular approach. This is explained in greater detail in Section 2.8. Typically the fluid domain is simulated only within the reservoir region via a reservoir simulator. Therefore coupling only occurs within the reservoir. However, ELFEN is unique as it performs full domain coupling. Fluid dynamics are modelled across the whole model domain.

2.3 Subsurface Structure: The Model Geometry

The initial stage of building a hydromechanical model is to define the basic subsurface structure (i.e. mechanical stratigraphy). This is typically derived from seismic data (e.g. Brown, 2011). Interpreted horizons are used to define different geological units, or layers, and the location and orientation of faults.

As no seismic data is available in which to define horizons and faults, the model geometry is devised loosely on North Sea geology with the reservoir interval located at a depth of 5km with a production well penetrating its centre. Multiple overburden layers and faults are included to enhance model complexity. As there is a need to run a large number of model perturbations the model domain is reduced to two dimensions (2-D). The modelled subsurface region is $20 \times 9 \text{km}^2$. Figure 2.1 shows the complete model geometry.

As ELFEN uses a continuum numerical method, the model domain must be discretized into small elements. This collection of small elements is referred to as a mesh. The mesh may be structured (squares in 2-D, or cubes in 3-D) or unstructured (triangles in 2-D, or tetrahedrons in 3-D) and the size of the elements chosen based on a trade-off between computation time and the required resolution of the solution. The smaller the element size, the more detailed the analysis but with the burden of an increased computational workload. Typically, the mesh is refined around particular areas of interest, such as faults or bedding planes, where the stress pattern might be required in greater detail.

For this model, the mesh is unstructured with triangular elements approximately 70m

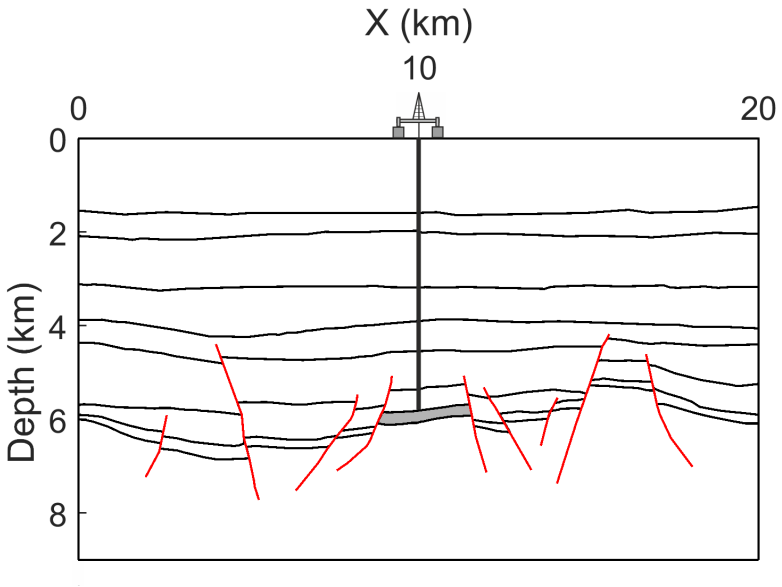

Figure 2.1: Model geometry with the reservoir region highlighted in grey and faults in red. The production well is located in the centre of the model domain (i.e. X =10km).

in size. Element size was determined such that the model produced stable results (free from unwanted dynamic effects), had acceptable computation time, and yielded suitable resolution (considering typical vertical and lateral resolution of seismic data between 1 and 5km depth). Figure 2.2 shows the CPU time for varying mesh sizes. Note the exponential increase in CPU time per relatively small increments in mesh size. Figure 2.2 also demonstrates the substantial increase in model runtime you would expect if the model was extended to 3-D.

Creating a numerically stable mesh in 2-D is relatively simple. However, for complex geometries in 3-D this process becomes more difficult. The pinching of horizons and reverse faults being some of the most difficult geology to mesh. At these locations elements often become small and their shape distorted. This leads to numerical instability in the FE analysis. Typically, a large amount of time is spent creating numerically stable meshes for complex scenarios. Once finished, this mesh is usually fixed and changing the underlying model geometry becomes difficult. However, for the case of a 2-D model, meshing becomes simpler and hence I was able to generate and test different sized meshes relatively easily for this relatively complex geometry (e.g. Figure 2.2). This also enables the underlying model geometry to be changed relatively easily if required for future analysis.

It is important to note that 2-D analyses will often produce different results to 3-D analyses. It is widely accepted that 2-D analyses produce more conservative results. The main reason for this difference is the ability of a 3-D analysis to account for the 3-D nature of the model inputs such as model geometry, *in situ* stresses, orientation of geological structures and the distribution of pore pressure. Wines (2016) outlines and describes this discrepancy in great detail by comparing slope stability modelling in two and three dimensions. A potentially significant conclusion from this study is the increase in the *in situ* horizontal stress found by modelling a concave slope in 3-D as opposed to 2-D. This increase in horizontal stress is a result of the larger confining effects generated by the shape of a 3-D concaved slope. This indicates a potential greater increase in horizontal stress above the reservoir when modelling in 3-D as a greater volume of rock mass falls in on itself as the overburden subsides. This discrepancy in horizontal stress change will have implications when considering the time-shift offset dependence as far offset travel times are increasingly influenced by horizontal velocities. The discrepancy between the modelled vertical stress is likely to be much less and hence reducing the problem to 2-D less detrimental when considering near-offset time-shifts. For the purpose of this study, a 2-D analysis is considered a reasonable representation of a production scenario. Also, as the seismic data used throughout this study is forward modelled directly from a 2-D truth case scenario the discrepancy between 2- and 3-D modelling is less significant. However,

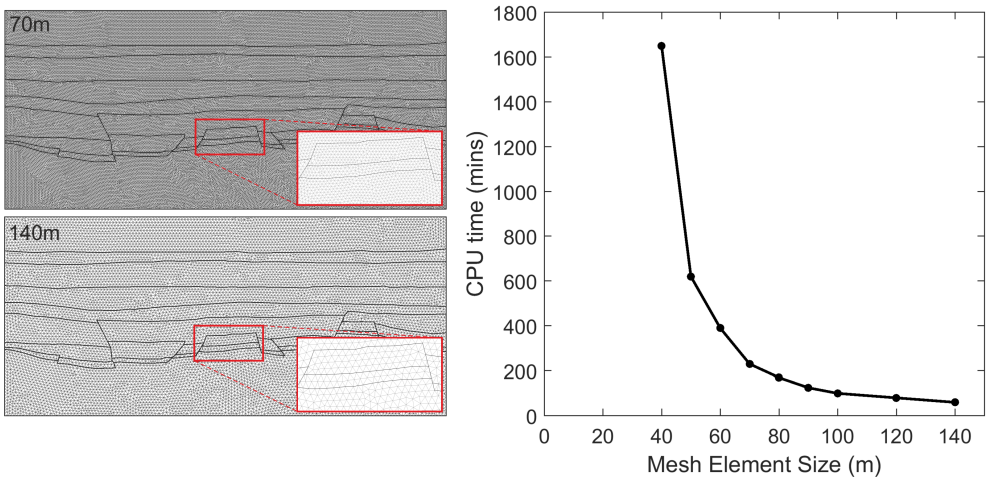

Figure 2.2: The model geometry is discretized with two meshes of differing element size (left). Also shown (right), are the model runtimes for these two meshes along with the runtime for a handful of other mesh sizes.

it is important to understand the implications of reducing production problems to 2-D, especially if modelling horizontal stress change is of great interest.

2.4 Elasto-plastic Material Properties

Once meshed, each stratigraphic layer in the model is populated with relevant mechanical and fluid properties. The mechanical properties primarily consist of elastic moduli and strength parameters whilst fluid properties consist of permeability and porosity. Elastic moduli control the amount of deformation (i.e. strain) as a result of an applied stress and is commonly described in terms of Young's Modulus, (ratio of axial stress and resultant axial strain) and Poisson's ratio (ratio of vertical and radial strain). Strength properties describe the critical stress values at which the rock will fail (i.e. stop behaving elastically) and is commonly characterised by a failure envelope.

Parameterising the mechanical and fluid properties requires laboratory testing on a large number of rock samples (e.g. Chapter 7 of Fjær & Kristiansen, 2009). Unfortunately, a large number of rock samples that adequately sample the entire subsurface area of interest is often not available due to the cost of coring (i.e. extracting rock samples). This is especially true for deep water reservoirs where drilling and rig-time are both expensive and difficult (Herwanger *et al.*, 2009). Fortunately, rock properties can also be determined through well log data or the inversion of seismic velocities. Seismic data is particularly useful in providing an insight to inter-well regions and possible spatial heterogeneity. However, properties derived using these methods are often inconsistent with those measured in the laboratory. For example, mechanically measured elastic properties

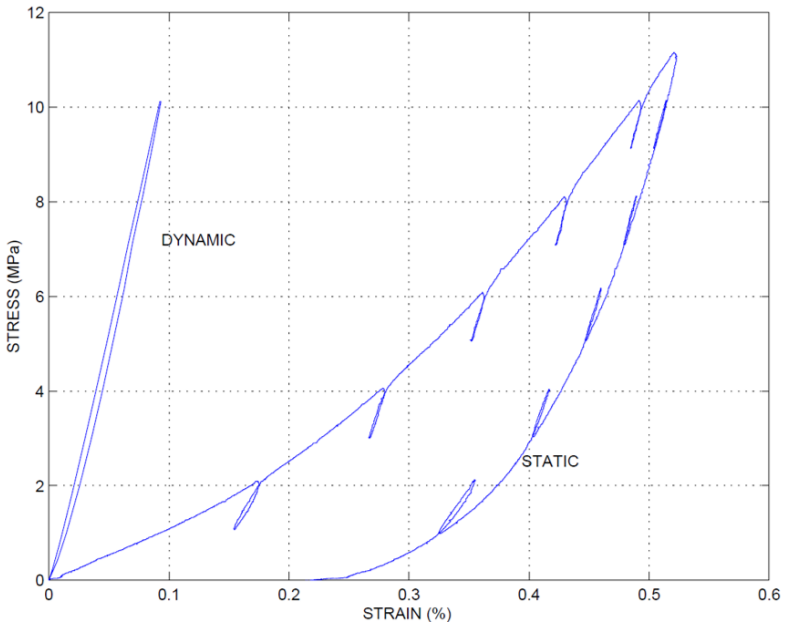

Figure 2.3: Plona & Cook (1995). Stress-strain curves for a room dry Castlegate sandstone sample calculated dynamically and statically in the laboratory. Static calculations of strain are made by taking direct displacement measurements from the sample using strain gauges. Dynamic strains are calculated by the stress divided by the dynamic Young's Modulus determined through ultrasonic P- and S-wave velocities.

are classed as static moduli and are typically smaller than the dynamic elastic moduli determined through velocities (be it ultrasonic wireline or low frequency seismic velocities). An example of this is shown in Figure 2.3. This phenomena is a result of a frequency dependence and thus specific correlation functions are required to convert between the two. Often these correlation functions, along with others for calculating fluid and strength properties, are empirical and lithology specific. Ideally, these would be derived using laboratory data taken from samples within the area of interest. However, when suitable data is unavailable, application of previously established functions must be used. Luckily, a large number of published correlation functions exist in literature (e.g. Dynamic to static: Asef & Najibi (2013); Gommesen & Fabricius (2001), Strength properties: Khaksar *et al.* (2009); Vernik *et al.* (1993), Fluid properties: Ijasan *et al.* (2013); Nicolaysen & Svendsen (1991)). It should be noted that care must be taken to use suitable functions that are consistent with the local geology and rock architecture. The application of unsuitable correlation functions can lead to the derivation of inaccurate rock properties.

I design nine different elasto-plastic materials, one for each of the nine stratigraphic layers of my model (Figure 2.1). In keeping with North Sea geology, I assume a sandstone reservoir with an impermeable shale caprock and multiple thick layers of stiff chalk in the overburden. To simplify model behaviour, a complex salt underburden (typically seen

in the North Sea) is substituted for a simple mechanically strong rock, typical of unfractured limestone/dolostone. As no data is available to characterise the properties of each material, I use a selection of the extensive literature available on North Sea geology and generic materials designed by Rockfield in their a generic material database (Rockfield Software Limited, 2012). A detailed description of all the material property relationships and associated parameters is described in the remainder of this section, whilst a definitive summary found in Table 2.1. It should be noted that I initially define isotropic materials. However, ELFEN does have the capability to deal with anisotropic properties. Also, fluid properties such as porosity and permeability, are defined for all rocks, even outside of the reservoir as ELFEN performs whole domain coupling (see Section 2.2).

2.4.1 Basic Properties

Grain density ρ_g and fluid density ρ_f make up the basic properties of a material in ELFEN. I assume all non-reservoir rocks to have a fluid density of 1.02g.cc^{-1} (Japsen, 1998), whilst the reservoir rock a fluid density of 0.81g.cc^{-1} to represent the density of light crude oil in the North Sea (Jones, 2010). The grain density of each shale is assumed to be 2.69g.cc^{-1} (Okiongbo, 2011), chalk assumed to be purely calcite with a grain density of 2.71g.cc^{-1} (Japsen, 1998), each sandstone to be composed mainly of quartz, 2.65g.cc^{-1}, and the stiff underburden a grain density of 2.81g.cc^{-1} typical of dolostone.

2.4.2 State Boundary Surface

The state boundary surface, or failure envelope, defines the stress at which a rock will fail (i.e. the limits of elastic behaviour). State boundary surfaces are typically defined in $p-q$

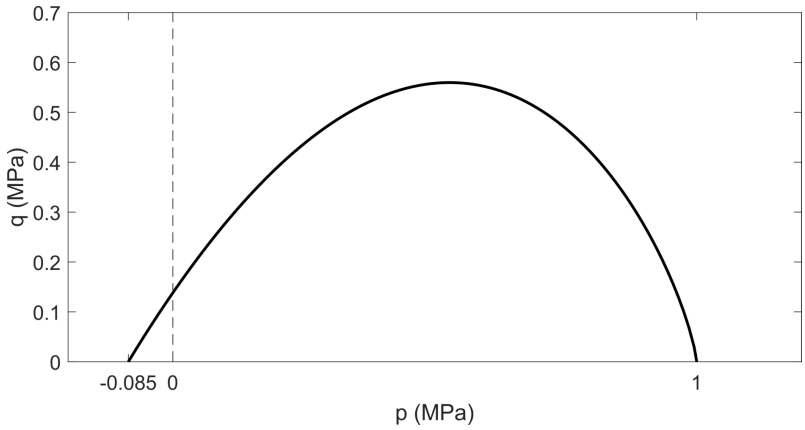

Figure 2.4: Yield surface in $p-q$ space for a generic sandstone in the material database of Rockfield Software Limited (2012) at surface conditions. For this particular material $p_{c0} = 1$, $p_{t0} = -0.085$, $\beta = 60°$, $n = 1.3$, $g = 1$ in equation 2.3.

space. The term p refers to the effective mean stress, which is defined as the mean of the principle stresses:

$$p = (\sigma'_1 + \sigma'_2 + \sigma'_3)/3. \tag{2.1}$$

Principle stresses correspond to the three normal stresses at a particular angle in which the shear stress becomes zero. σ'_1 being the largest principle stress and σ'_3 the smallest. The magnitude and direction of these stresses can be found by calculating the eignenvalues and eigenvectors of the effective stress tensor $\sigma'_{\mathbf{ij}}$.

The term q refers to the deviatoric stress which is defined (for 2-D triaxial conditions) as the difference between the maximum and minimum principle stress:

$$q = \sigma'_1 - \sigma'_3. \tag{2.2}$$

The envelope used for each material is the Soft Rock (SR3) model of Crook *et al.* (2006). The SR3 yield function is a smooth, three-invariant surface defined in $p - q$ space that intersects the p axis in both tension p_{t0}, and compression p_{c0}. It is defined as:

$$\Phi(p) = g(\theta, p)q + (p - p_{t0})tan\beta\left(\frac{p - p_{c0}}{p_{t0} - p_{c0}}\right)^{1/n}, \tag{2.3}$$

where β and n are material constants and θ the lode angle. Finally, $g(\theta, p)$ is the deviatoric plane correction term that controls the shape of the yield surface in the deviatoric plane. An example SR3 failure envelope is shown in Figure 2.4. The evolution of the plastic flow is defined by a non-associated flow rule:

$$\dot{\varepsilon^p} = \dot{\lambda}\frac{\partial \Psi}{\partial \sigma}, \tag{2.4}$$

where $\dot{\lambda}$ is the plastic multiplier and Ψ is the plastic potential defined as:

$$\Psi(p) = g(\theta, p)q + (p - p_{t0})tan\psi\left(\frac{p - p_{c0}}{p_{t0} - p_{c0}}\right)^{1/n}. \tag{2.5}$$

Note that equation 2.5 is of identical form to that of the state boundary surface defined in equation 2.3. However, the plastic potential is defined in terms of the angle $tan\psi$, where ψ is the dilation parameter controlling the shape of the plastic potential surface. The deviatoric plane correction term g is scaled to be 1 such that the strength in triaxial compression directly corresponds to the strength calibrated using compressive triaxial (CTC) tests (Crook *et al.*, 2006). The initial state boundary surface is defined at a reference porosity ϕ_{ref} (i.e. surface conditions). To define the state boundary surface for each material, a compilation of test data presented in the generic material database of Rockfield Software Limited (2012) is used. A summary of the final chosen parameter values is presented in Table 2.1.

2.4.3 Yield Surface Evolution

The evolution (or hardening) of the primary yield surface is determined through relationships that define p_c and p_t as a function of volumetric plastic strain ε_v^p:

$$p_c = p_{c0} + (p_{c0} - p_{c(resid)})\left[exp\left(-\frac{v\Delta\varepsilon_v^p}{(\lambda-\kappa)}\right) - 1\right], \tag{2.6}$$

$$\begin{aligned} p_t^* &= p_{t0} + (p_{t0} - p_{t(resid)})\left[exp\left(-\frac{v\Delta\varepsilon_v^p}{(\lambda-\kappa)}\right) - 1\right], \\ p_t &= max[p_{t0}, p_t^*]. \end{aligned} \tag{2.7}$$

Here, κ and λ are Cam-Clay hardening constants and v is the specific volume. v can be related to porosity via $1/(1-\phi)$. Note that $p_{c(resid)} = p_{c0}/100$ and $p_{t(resid)} = p_{c0}/100$ to ensure the yield surface is always of finite size. The volumetric plastic strain ε_v^p can also be defined in terms of porosity via:

$$\varepsilon_v^p = log\left[\frac{1-\phi_{ref}}{(1-\phi_{init})}\right]. \tag{2.8}$$

These hardening relationships allow a material characterisation defined at surface conditions, with a specific reference porosity ϕ_{ref}, to be used to generate data suitable for a similar material at greater depth (subjected to compaction) with a different initialization porosity ϕ_{init}. The shape of the state boundary surface remains unchanged but its size is governed by the scaling of p_{c0} to $p_{c(init)}$ and p_{t0} to $p_{t(init)}$. Examples of the two evolution functions are shown in Figure 2.5.

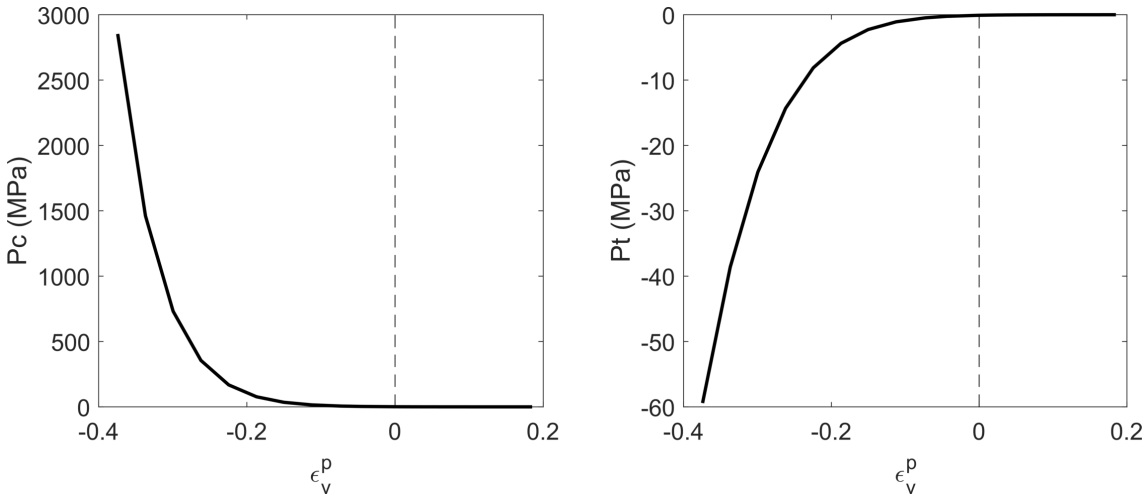

Figure 2.5: Yield surface evolution for a generic sandstone in the material database of Rockfield Software Limited (2012). The yield surface increases in size as p_c and p_t vary with volumetric strain ε_v^p. For this particular material $\kappa = 0.012$ and $\lambda = 0.086$ in equations 2.6 and 2.7.

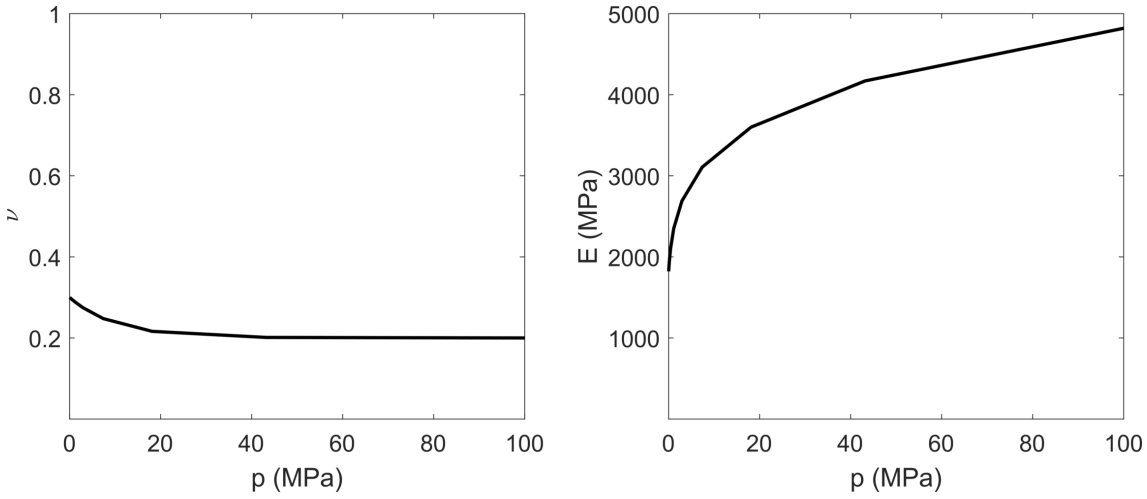

Figure 2.6: Elastic properties E and ν defined as functions of the effective mean stress p for a generic sandstone in the material database of Rockfield Software Limited (2012). For this particular material, $E_{ref} = 400$, $A = B = 0.276$, $n = 0.3$, $c = -2$, $\nu_{max} = 0.3$, $\nu_{min} = 0.2$ and $m = 0.1$ in equations 2.10 and 2.11.

κ and λ are defined from the compilation of test data presented in the generic material database of Rockfield Software Limited (2012). The initialisation porosity ϕ_{init} corresponds to the porosity of the material at the start of the simulation. Its value for each material is determined through either porosity-depth relationships for North Sea rocks (Bloch *et al.*, 2002; Mallon & Swarbrick., 2008) or estimated using typical North Sea bulk density ρ values (Japsen, 1998, 2000; Marcussen *et al.*, 2010; Okiongbo, 2011; Slagstad *et al.*, 2008) via:

$$\rho = \rho_g(1 - \phi_{init}) + \rho_f \phi_{init}. \tag{2.9}$$

A complete summary of yield surface evolution parameter values are presented in Table 2.1.

2.4.4 Elastic Properties

Young's modulus E and Poisson's ratio ν are defined in ELFEN as empirical functions of effective mean stress p:

$$E = E_{ref}\left[\frac{p + A}{B}\right]^n \phi(p)^c, \tag{2.10}$$

$$\nu = \nu_{min} + (\nu_{max} + \nu_{min})(1 - e^{mp}). \tag{2.11}$$

E_{ref} is the effective Young's Modulus while ν_{max} and ν_{min} are the Poisson's ratio values at high and low effective mean stress p respectively. n, c and m are material constants,

while A and B are also material constants used to prevent problems near zero values of p. Finally, $\phi(p)$ is the porosity, which itself is a function of effective mean stress p.

These elastic relationships are calibrated such that the *in situ* Young's Modulus and Poisson's ratio of each material, prior to production, resemble those stated in the Thesis of Garcia (2011) and their nonlinear behaviour calibrated using the generic material database of Rockfield Software Limited (2012). Again, all elastic parameters can be found in Table 2.1. Note that we have initially specified a constant ν for this study as we assume negligible changes to ν with effective mean stress. E and ν as a function of effective mean stress is demonstrated in Figure 2.6.

2.4.5 Porous Flow

ELFEN uses a porosity dependant intrinsic permeability K_{in} which is based upon the Kozeny-Carman (Carman, 1937; Kozeny, 1927) relationship

$$K_{in}(\phi) = K_0 \frac{\phi^x}{(1-\phi)^y}, \tag{2.12}$$

where K_0, x and y are material constants. The chosen parameters are provided in Table 2.1 and based on the values given by Schneider *et al.* (1996). An example porosity dependant permeability curve is shown in Figure 2.7.

2.4.6 Consolidation Properties

Additional material consolidation properties are also required by ELFEN. An effective stress coefficient (i.e. Biot) α is required which controls the fraction of the pore pressure

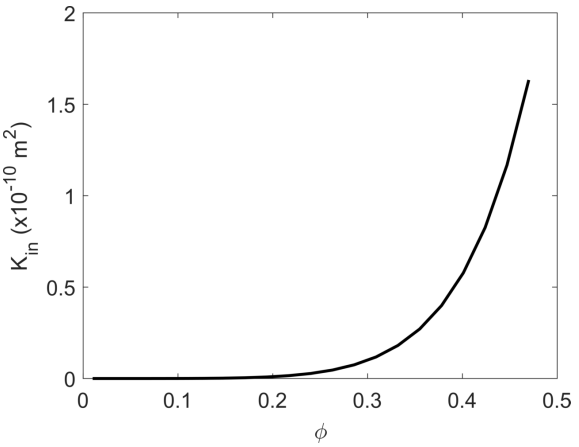

Figure 2.7: Intrinsic permeability K_{in} expressed as a function of the porosity ϕ for a generic sandstone in the material database of Rockfield Software Limited (2012). For this particular material, $K_0 = 2 \times 10^{-9}$, $x = 5$ and $y = 2$ in equation 2.12.

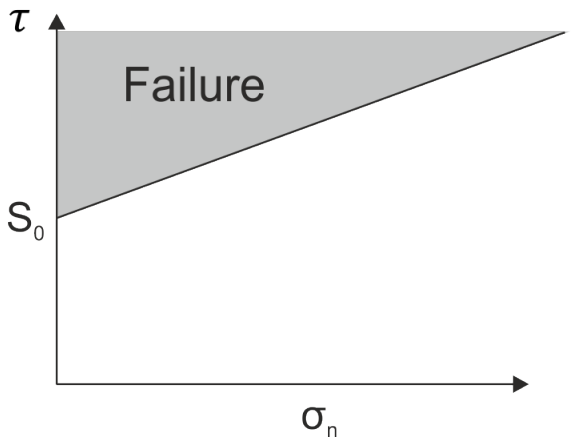

Figure 2.8: Coulomb failure criteria

that contributes to the effective stress σ':

$$\sigma' = \sigma - \alpha P_p. \tag{2.13}$$

Here, σ corresponds to the direct stress whilst P_p the pore pressure. An α value of 1 is chosen for all rock types (a parameter usually set to 1 in most modelling scenarios). A fluid viscosity η is also required and set to 1×10^{-9}MPa.s^{-1} (typical of pure water) in all non-reservoir layers. Within the reservoir $\eta = 0.638\times10^{-9}$MPa.s^{-1}, similar to the viscosity of hydrocarbons from the North Sea Forties field (Jones, 2010). Fluid K_f and grain K_s stiffnesss are also required. For these we use typical values found in North Sea literature (Jackson & Richardsons, 2007; Jaeger *et al.*, 2009; Wright, 1967; Zang & Reeder, 1999). Finally a horizontal to vertical stress ratio K_{xy} is set at 0.6 for all materials.

In addition to the required consolidation properties, I include an over/under-pressure parameter ΔP_p. This alters the settled *in situ* (see Section 2.6) pore pressure state of each material. Within the North Sea, it is predicted that overburden chalks are overpressured. Therefore, within the model, two chalk layers are overpressured, one by +20MPa and another by +5MPa (see Figure 2.10). A summary of all the consolidation properties can be found in Table 2.1.

2.5 Fault Properties

The subsurface is beset with fractures of different sizes and orientations. These pre-existing planes of weakness have different failure properties to areas of unfractured or intact rock. Therefore, it is important to include large faults within the hydromechanical model and simulate their behaviour throughout production. Faults in ELFEN are modelled as discrete

contacts with a Coulomb failure criteria. Faults will slip if the shear stress τ on the fracture exceeds:

$$\tau = S_0 + \sigma_n \mu. \tag{2.14}$$

Here, S_0 is the cohesion (shear strength at zero normal stress), σ_n the fracture normal stress and μ the coefficient of static friction (balance between shear and normal stress). Equation 2.14 is shown graphically in Figure 2.8. In this particular model, faults are included, (see Figure 2.1) but not initialised. They are left as simple lithological discontinuities. This is done to initially simplify the model and the production related geomechanical effects but are included in the geometry and mesh such that they can be initiated, if required, at a later date.

Layer N°	Lithology	Grain & fluid densities		SR3 model (equations 2.3-2.5)				Yield Surface Evolution (equations 2.6-2.9)				Elastic Properties (equations 2.10 & 2.11)						Permeability Properties (equation 2.12)			Consolidation Properties						
		ρ_g ($g.cc^{-1}$)	ρ_f ($g.cc^{-1}$)	p_c (Mpa)	p_t (Mpa)	β	n	ψ	κ	λ	ϕ_{ref}	ϕ_{init}	E_{ref} (MPa)	A	B	n	ν_{min}	ν_{max}	m	c	K_0 (m^2)	x	y	K_f (MPa)	K_s (MPa)	α	η ($MPa.s^{-1}$)	K_{xy}	ΔP_p (MPa)
1	Shale	2.69	1.02	0.17	-1	60	1.3	51	0.012	0.106	0.55	0.38	910	-0.2758	-0.2758	0.085	0.31	0.31	1	-0.9	$4.20x10^{-19}$	3	2	2400	36000	1	1	0.6	0
2	Sandstone	2.65	1.02	0.28	-1	66	1.7	56	0.012	0.174	0.55	0.33	1850	-0.2758	-0.2758	0.15	0.31	0.31	1	-0.5	$6.61x10^{-11}$	5	2	2400	26000	1	1	0.6	0
3	Chalk	2.71	1.02	2	-100	67	1.76	55	0.008	0.06	0.35	0.2	410	-0.2758	-0.2758	0.38	0.31	0.31	1	-2	$1x10^{-22}$	3	2	2400	130000	1	1	0.6	0
4	Chalk	2.71	1.02	2	-100	67	1.76	55	0.008	0.06	0.2	0.105	30000	-0.2758	-0.2758	0.038	0.31	0.31	1	-0.015	$1x10^{-22}$	3	2	2400	130000	1	1	0.6	5
5	Chalk	2.71	1.02	2	-100	67	1.76	55	0.008	0.06	0.3	0.06	30500	-0.2758	-0.2758	0.02	0.33	0.33	1	-0.1	$1x10^{-22}$	3	2	2400	130000	1	1	0.6	20
6	Chalk	2.71	1.02	2	-100	67	1.76	55	0.008	0.06	0.3	0.12	6000	-0.2758	-0.2758	0.27	0.31	0.31	1	-0.13	$1x10^{-22}$	3	2	2400	130000	1	1	0.6	0
7	Shale	2.71	1.02	0.6	-1	56	1.3	47	0.012	0.077	0.29	0.03	3800	-0.2758	-0.2758	0.059	0.33	0.33	1	-0.21	$1x10^{-22}$	3	2	2400	36000	1	1	0.6	0
8	Sandstone	2.65	1.02	0.65	-1	66	1.7	56	0.012	0.129	0.5	0.12	395	-0.2758	-0.2758	0.15	0.13	0.13	1	-1.2	$6.61x10^{-11}$	5	2	2100	36000	1	1	0.6	set to 110
8	Sandstone (Pay)	2.65	0.81	0.65	-1	66	1.7	56	0.012	0.129	0.5	0.12	225	-0.2758	-0.2758	0.23	0.13	0.13	1	-1.28	$6.61x10^{-11}$	5	2	2400	36000	1	0.638	0.6	set to 110
9	Dolostone	2.811	1.02	2	-100	67	1.76	55	0.008	0.06	0.005	0.01	59500	-0.2758	-0.2758	0	0.25	0.25	1	-0.03	$4.20x10^{-19}$	5	2	2400	200000	1	1	0.6	0

Table 2.1: Material properties for each layer in Figure 2.1. The layer number represents increasing depth from surface.

2.6 Model Equilibration

Once the model is populated with the relevant material properties it must then be equilibrated and the *in situ* (i.e. current day), stress state determined. This requires the application of external loads such as gravity, pore pressure, and horizontal tectonic stresses. This process is typically calibrated to both world stress maps (e.g. Heidbach *et al.*, 2016) and stress/pore pressure observations made in wells (e.g. Zoback, 2010). Alterations to the *in situ* stress can be made by varying the pore pressure of certain regions or by varying tectonic stresses by altering the model boundary conditions. Boundary conditions are varied by increasing/decreasing boundary forces applied to the sides of the model which mimic regional tectonic forces. The equilibration process is often difficult to calibrate as there is limited knowledge of the subsurface stress and pore pressure state.

In ELFEN, the *in situ* stress and pore pressure is determined through a period of settling time steps in which the model is loaded under gravity. Any disequilibrium caused by the loading on the geometry is given time to relax, avoiding numerical oscillations (i.e. unwanted dynamic effects) in the modelling results. During this process, the model surface is free to displace whilst its other boundaries constrained with rolling (i.e. zero/fixed perpendicular displacement) boundary conditions. The vertical stress is calculated from the lithostatic gradient (i.e. vertical pressure due to weight of overlying rock) whilst the region, horizontal, tectonic forces derived using the vertical stress and provided K_{xy} ratio (see Section 2.4.6).

It is important to note that fixed boundary conditions are unphysical and hence can often result in inaccurate stress predictions close to the model boundaries. Therefore, it

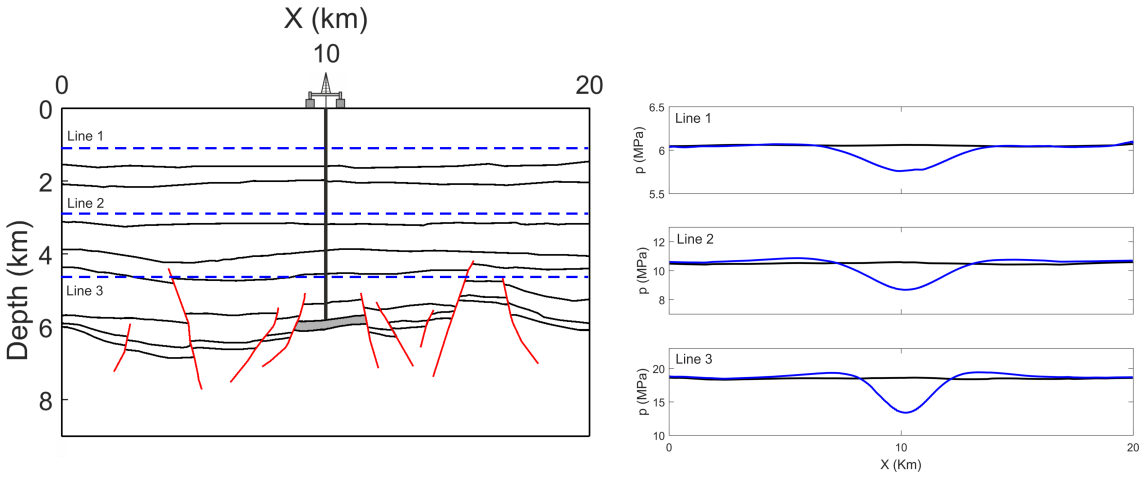

Figure 2.9: Initial pre-production mean effective stress p (black line) and p after 20 years of production (blue line) taken at three depth slices (1km, 2.5km and 4.5km) within the overburden. Note the negligible change in p at the boundaries of the model domain.

is important to extend the model domain far beyond the region of interest (i.e. reservoir vicinity) such that the boundary conditions have little influence on the modelled stress and displacement. However, to preserve computational efficiency it is typically desirable to make the modelled domain as small as possible but maintain the same stress and displacements within the region of interest as would occur if a much larger rockmass was modelled. Locating the model boundaries at approximately 10km away from the reservoir region proved optimal. This is demonstrated in Figure 2.9 whereby the extent of the mean effective stress change in the overburden caused by production is negligible at the model boundaries.

The pore pressure is calculated from the hydrostatic gradient (i.e. pressure exerted due to weight of overlying fluid) with the phreatic surface (pore pressure origin) set 50m

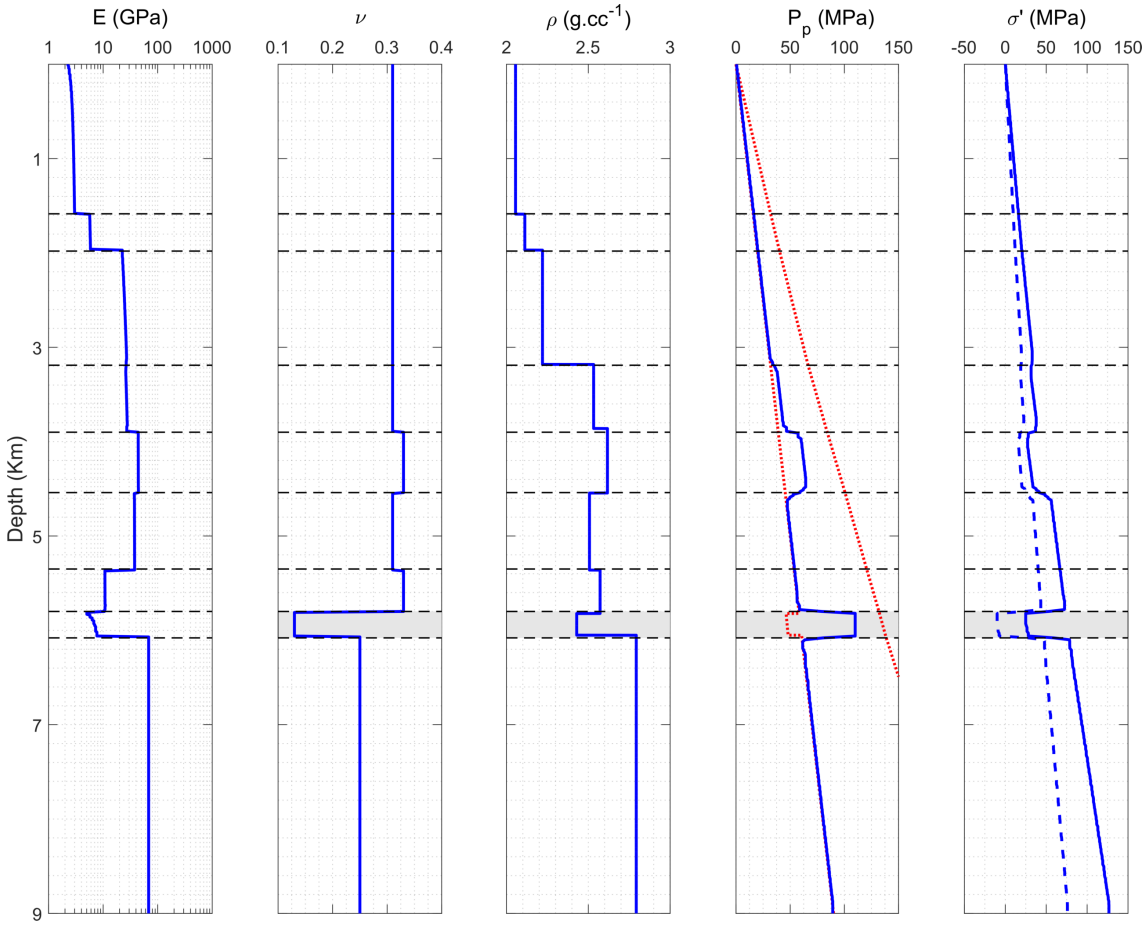

Figure 2.10: Logs of Young's Modulus E, Poisson's Ratio ν, Bulk density ρ, Pore pressure P_p and horizontal (dotted) and vertical (solid) effective stress σ' through the final hydromechanical model, post model equilibration and prior to reservoir production (i.e. 0 years). Layer boundaries are marked via dotted horizontal lines. The lithostatic and hydrostatic gradients are plotted in red on the P_p log. Note the two overpressured chalk layers in the overburden. The reservoir layer is shaded. Logs are taken at the production well location (see Figure 2.1).

above the surface of the model to mimic a shallow North Sea environment. Figure 2.10 show logs of the final geomechanical model properties, post geostatic initialisation and prior reservoir production.

2.7 Production Schedule

The final piece of information required for a hydromechanical model is the location and trajectory of all wells along with their production schedules. Typically, the production schedules are given in barrels of oil produced per day and is provided by the petroleum engineers. In this particular model the production schedule is defined in terms of a pore pressure loading curve. The reservoir interval is initially overpressured to 110MPa prior to production and uniformly depleted by roughly 50% over a period of 20 years. The rate of depletion is shown in Figure 2.11 and is based on the production profile of the HPHT reservoir given by Hawkins *et al.* (2007).

2.8 Coupling

For stability purposes, Rockfield suggest that solutions for the mechanical domain are solved explicitly whereas solutions for the fluid domain solved implicitly via a nonlinear Newton-Raphson approach (e.g. Tarantola, 2005). As the two sets of physical equations are solved via different numerical approximations, hydromechanical modelling in ELFEN involves iterative modular coupling of the whole model domain. Solutions for both fields

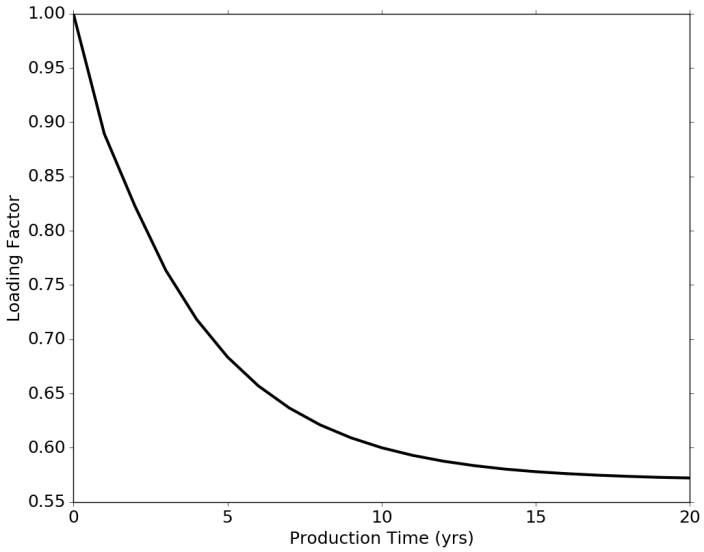

Figure 2.11: Reservoir pore pressure reduction given in normalised units, 1=110MPa.

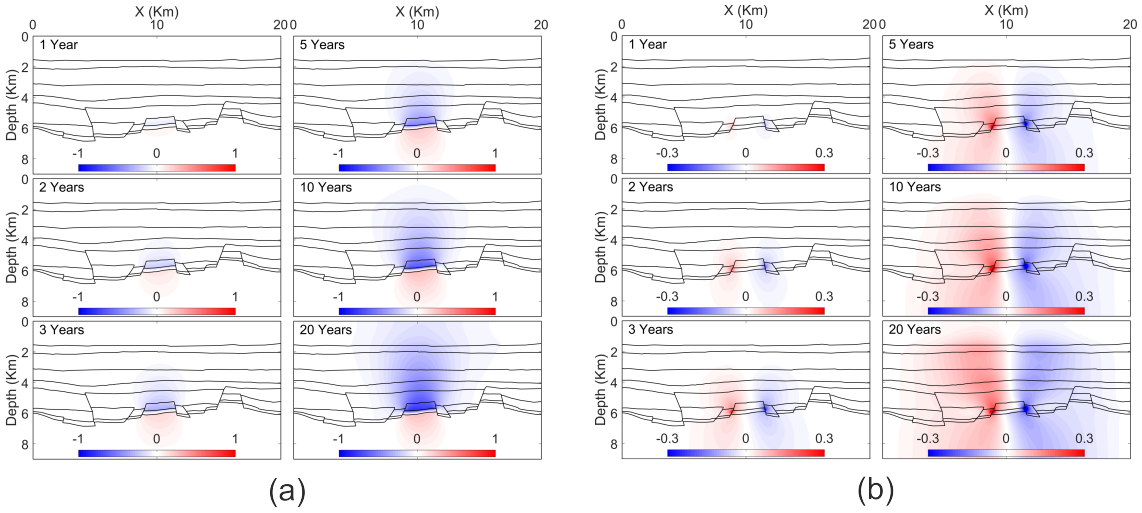

Figure 2.12: Predicted change in vertical displacement Δz (a) and horizontal displacement Δx (b) in meters from the initial pre-production state (i.e. 0 years) for six separate production years: 1, 2, 3, 5, 10 and 20. Note the difference in the colourbar, changed for visual purposes.

are solved simultaneously and compared at specified coupling intervals. Numerous iterations of each simulator occur until the coupled solution has converged.

The coupling rate for the hydromechanical process is similar to that of the implicit time step. This is typically 400-500 times larger than the explicit step. A robust explicit time step Δt can be estimated via:

$$\Delta t = f_{crit} \times min \left| l^e \sqrt{\frac{\rho^e}{E^e}} \right|. \tag{2.15}$$

$l^e \sqrt{\rho^e / E^e}$ is defined as the critical time step where E^e, ρ^e and l^e are the Young's Modulus, density and characteristic length of the minimum element respectively. The critical time step is a stability condition which prevents the magnification of round-off errors caused by the explicit scheme (e.g. Rao, 2010). Its calculation is approximate and therefore the factor of critical step f_{crit} is introduced. Rockfield suggests that for 2-D hydromechanical models $f_{crit} = 0.9$. Using the approximated mechanical time-step, a coupling rate of 0.01 time steps is chosen. This is well within the model's stability threshold whilst not being too small such that it compromises computational runtime or numerical stability.

2.9 Time-lapse Geomechanical Results

The time-lapse model results for six different production years is shown Figures 2.12 and 2.13. Shown are plots of the vertical Δz and lateral Δx displacement (Figure 2.12) and the change in vertical effective stress $\Delta \sigma'_v$, horizontal effective stress $\Delta \sigma'_h$ and shear stress

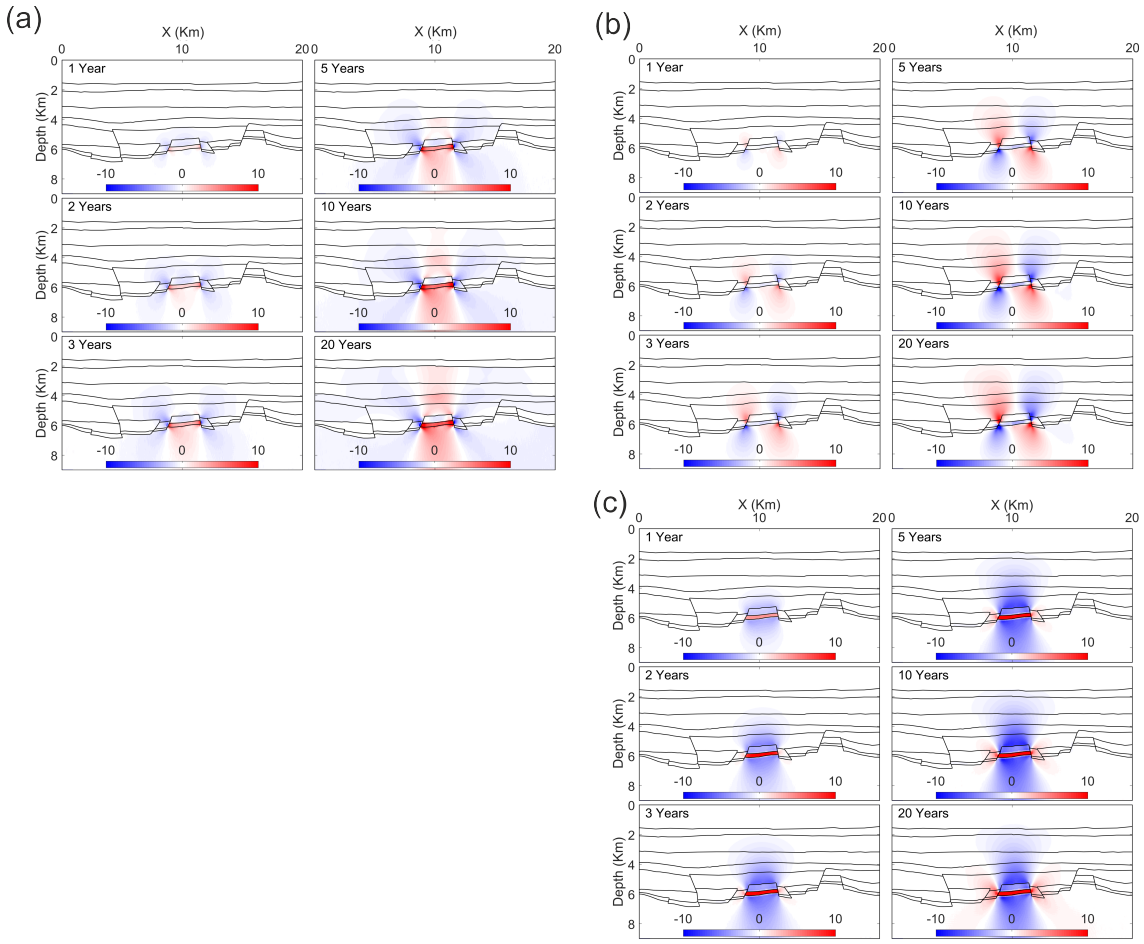

Figure 2.13: Predicted change in vertical effective stress $\Delta\sigma'_v$ (c), horizontal effective stress $\Delta\sigma'_h$ (a) and shear stress $\Delta\tau$ (b) in MPa from the initial pre-production state (i.e. 0 years) for six separate production years: 1, 2, 3, 5, 10 and 20.

$\Delta\tau$ (Figure 2.13) between the initial model state (at time 0) and the corresponding production year (i.e. monitor - baseline). The geomechanical model estimates total reservoir compaction of roughly 0.8m, surface subsidence of up to 0.2m and a reduction in overburden effective stresses within the range 0-7MPa. These values are typical of HPHT scenarios in the North Sea (e.g. Figure 2.14) and thus renders my synthetic model a good representation of a true production scenario.

2.10 Forward Modelling Time-lapse Seismic Data

To estimate production induced seismic time-shift requires a P-wave velocity model and a corresponding rock physics model. Using Young's Modulus E, Poisson's ratio ν and bulk

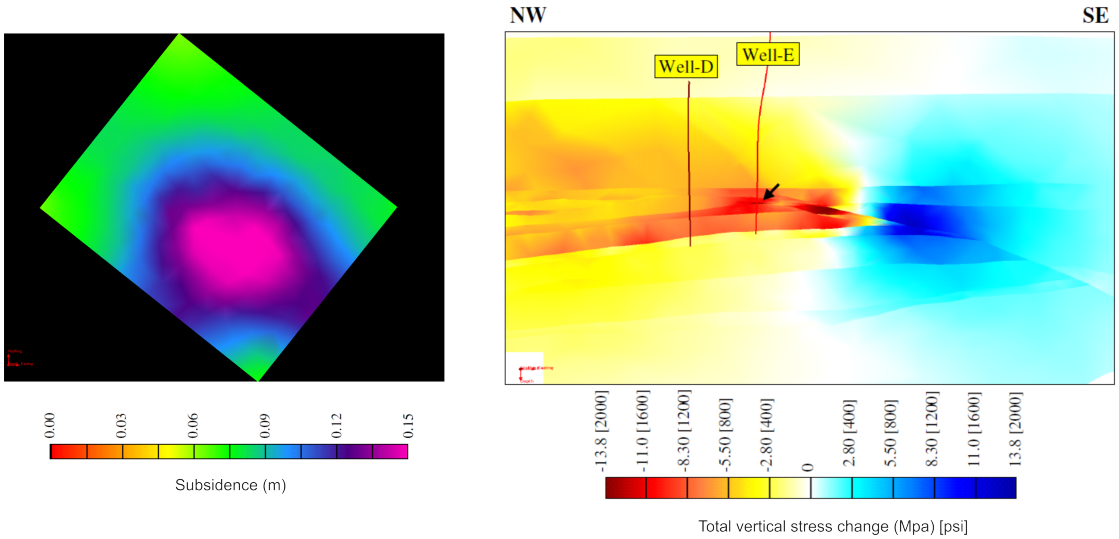

Figure 2.14: De Gennaro *et al.* (2008). Subsidence (left) and total vertical effective stress change (right) predicted by a hydromechanical model of a HPHT faulted gas condensate field located in the UK Central Graben of the North Sea.

density ρ (Figure 2.10) the P-wave velocity V can be calculated via:

$$V = \sqrt{\frac{E(1-\upsilon)}{\rho(1+\upsilon)(1-2\upsilon)}}. \tag{2.16}$$

Equation 2.16 estimates P-wave velocities using static elastic moduli. Hence, these velocities are typically slower than those expected (see Section 2.4). To obtain more realistic dynamic speeds requires a dynamic to static conversion. However, in this case no static to dynamic conversion was used as the static mechanical properties give rise to credible dynamic seismic velocities. The initial velocity model is assumed to be isotropic and is shown in Figure 2.15.

To relate a change in effective stress $\Delta\sigma'$ to a change in seismic velocity requires knowledge of the velocity-stress relationship. This is represented in the form of a rock physics model and is typically derived from laboratory core data and is lithology dependant. Rock physics modelling is an important step in coupling observed time-lapse anomalies to mechanical subsurface changes and will be discussed in greater detail in Chapter 4. For this scenario, it is assumed that each lithological layer in the model has the same simple, linear, effective stress-velocity relationship of $dV/d\sigma' = 0.004km.s^{-1}.MPa^{-1}$. This is a fair representation of a velocity-stress relationship considering typical core-measurements (e.g. Angus *et al.*, 2009, 2012).

The chosen rock physics model is also assumed to be isotropic i.e. independent of the direction in which the wave is propagating. The horizontal and vertical velocities have the same stress dependence. Therefore, production induced velocity anisotropy can be

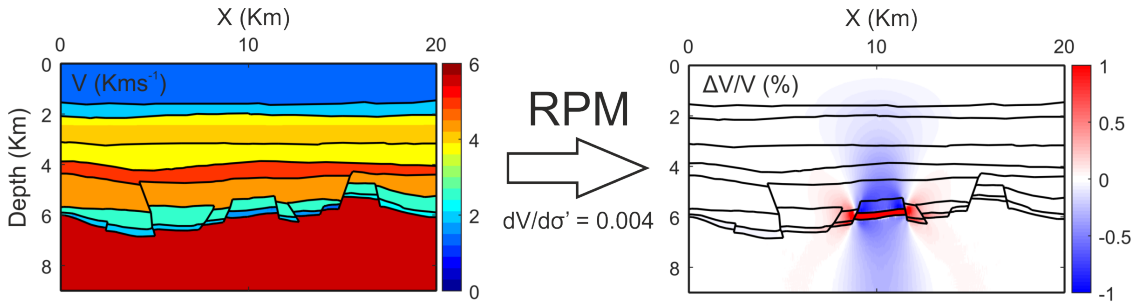

Figure 2.15: Pre-production (i.e. 0 years) P-wave velocity V model derived from equation 2.16 (left) and the fractional change in vertical P-wave velocity after 20 years of production assuming a rock physics model of $dV/d\sigma' = 0.004km.s^{-1}.MPa^{-1}$. Note that the fraction change in vertical P-wave velocity shown in this Figure is calculated from the modelled change in vertical effective stress $\Delta\sigma'_v$.

assumed to be directly related to the anisotropic change in the effective stress as opposed to any anisotropy introduced by the rock physics model. For example, Figure 2.15 shows the fractional change in vertical seismic velocity after 20 years of production derived from the modelled $\Delta\sigma'_v$.

2.10.1 Near-offset Time-strains

Near-offset seismic travel times are estimated by vertically integrating the *in situ* P-wave velocity model. This is an adequate numerical approximation considering the relatively flat geometry. The resultant pre-production vertical two-way travel times can be seen in Figure 2.16 along with the resultant near-offset (i.e. vertical) time-shifts Δt_v calculated assuming vertically propagating seismic waves are affected by changes in Δz and $\Delta\sigma'_v$.

Using these results it is possible to derive overburden layer time-strains $\Delta t_v/t_v$ along with each layer's average fractional change in seismic velocity $\Delta V/V$ and thickness ε_{zz}. These are shown in the logs of Figure 2.16 along with each layer's R-factor (equation 1.2). Over the entire 20 years of production the model predicts a total vertical time-shift to top reservoir of approximately 10ms. This is similar to the time shifts observed in the HPHT Elgin and Franklin fields of the North Sea as demonstrated in Figure 2.17. Overburden layer R-factors do appear large compared to those suggested by Hatchel & Bourne (2005). However, similar R-values of up to 50 have been documented in literature (e.g. Garcia *et al.*, 2010).

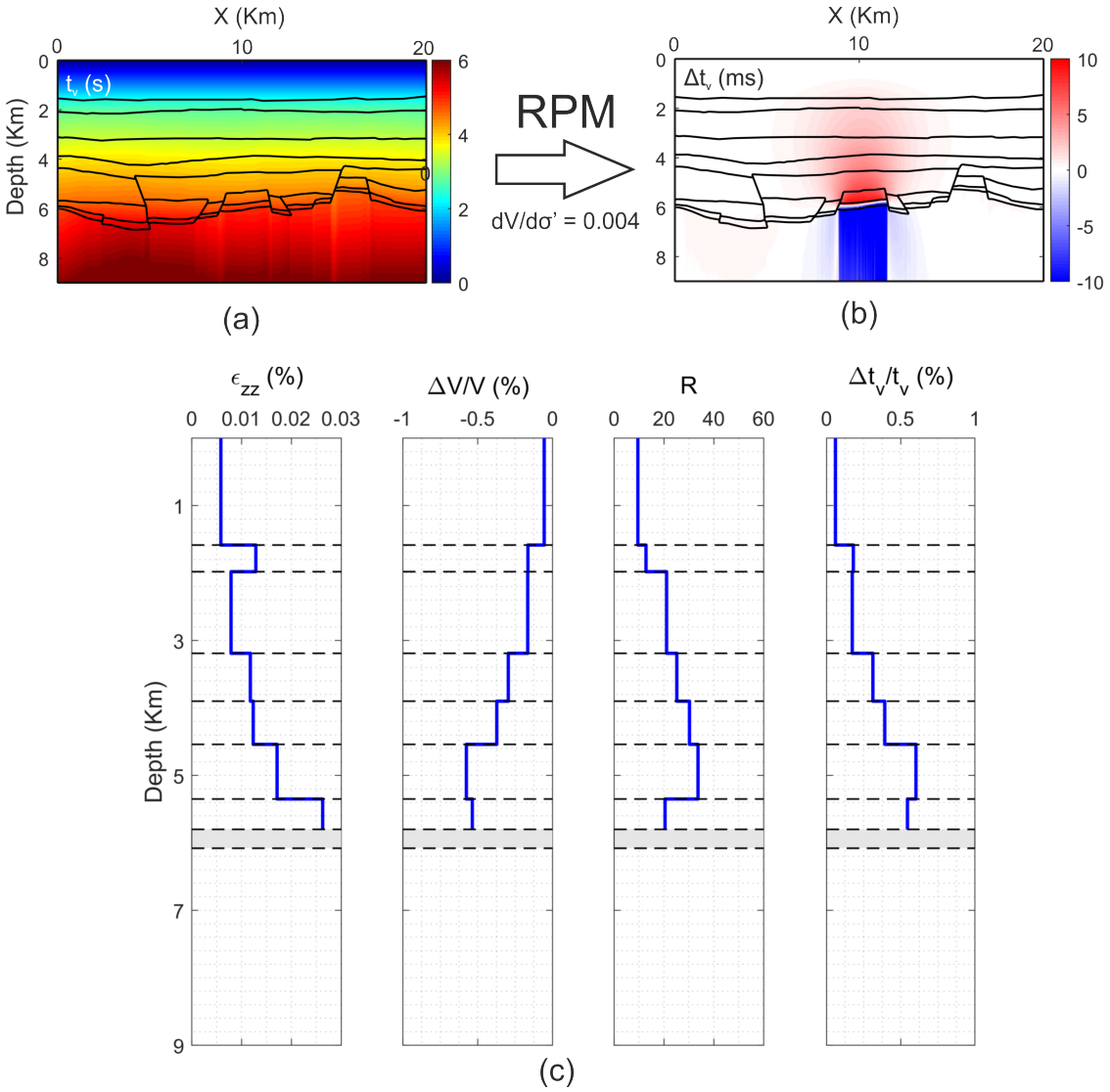

Figure 2.16: (a) Pre-production (i.e. 0 years) two-way vertical travel times t_v (in seconds) found by vertical integration of the velocity model in Figure 2.15. (b) Change in vertical travel times Δt_v (in milliseconds) after 20 years of production assuming a rock physics model of $dV/d\sigma' = 0.004 km.s^{-1}.MPa^{-1}$. Corresponding overburden logs are shown in (c), which show each layers time-strain $\Delta t_v/t_v$, average fractional change in velocity $\Delta V/V$ and thickness ε_{zz} and resultant R-factor. Layer boundaries are marked via dotted horizontal lines whilst the reservoir layer shaded. Logs are taken at the production well location shown in Figure 2.1

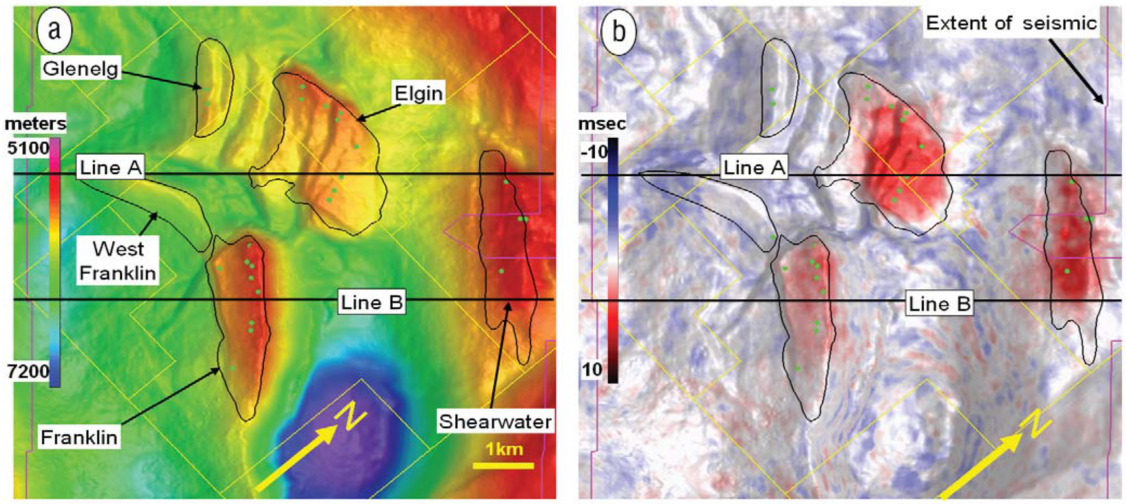

Figure 2.17: Hawkins *et al.* (2007). Top reservoir maps of (a) depth structure, (b) time-shifts between base and monitor survey for the Elgin and Franklin fields of the North Sea.

2.10.2 Time-shift vs Offset

As previously discussed in Chapter 1, production related stress change can result in anisotropic velocity change. The contrast between the change in vertical and horizontal velocity at varying locations within the subsurface means that time-lapse time-shifts are offset dependant. As offset increases the raypaths become more horizontal and the greater the influence of the horizontal velocity (i.e. stress) change. As such, the time-shift offset behaviour is seen to hold additional geomechanical information, particularly regarding the rate and extent of the anisotropic stress change.

Forward modelling non-normal time-shifts becomes slightly more complicated than modelling simple vertical shifts as velocity anisotropy and refraction needs to be considered. However, the potentially rich geomechanical information stored within the offset dependency of the time-shifts could make them vitally important for seismic history matching.

The analytical method of modelling non-normal incidence time-shifts using the R-factor, introduced in Chapter 1, has previously failed to predict the time-shifts observed in data (e.g. Kudarova *et al.*, 2016). Therefore, I choose to use an anisotropic raytracing methodology which uses a combination of Snells law and simple trigonometry. It is well understood that finite difference, full waveform techniques are the most superior for modelling wave propagation. However, the extremely large computational resources required to implement these techniques over a large model domain makes them unfeasible. For estimating travel times, raytracing is a more than adequate alternative.

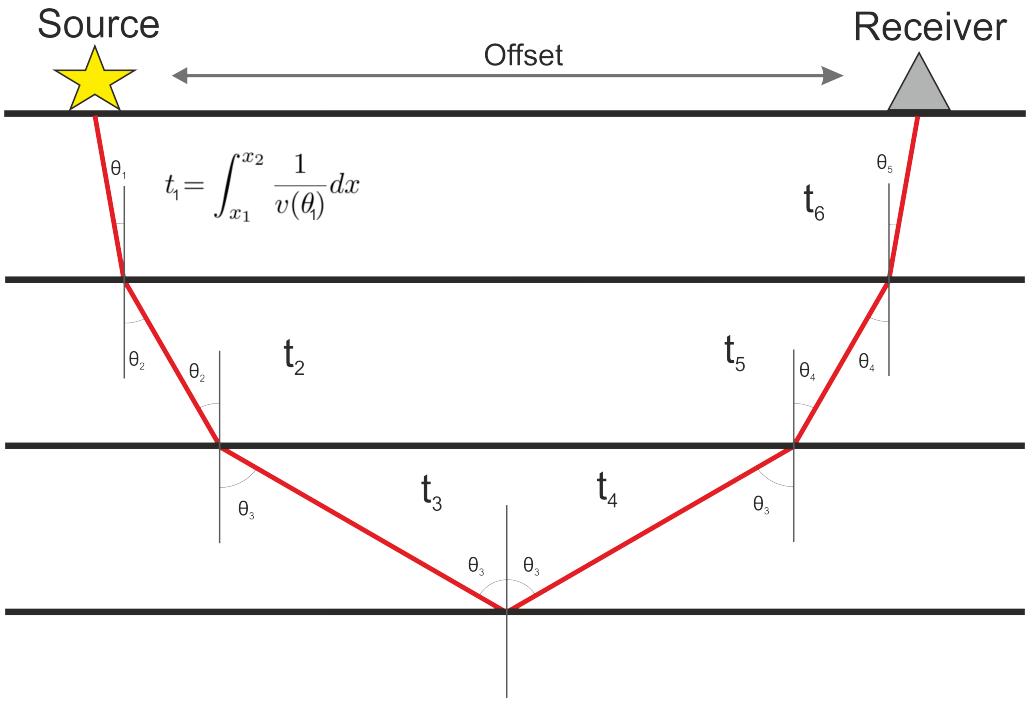

Figure 2.18: Schematic example of the seismic raytracing methodology through a multi-layered medium. At each horizon, the ray is refracted based on the velocity contrast across the interface described via Snell's law (equation 2.17). Assuming raypaths are straight within each layer, the angle of refraction will equal the angle of incidence. The total, two way travel time of the ray recorded at the receiver will be equal to the sum of travel times within each layer t_i. The travel time in each layer is related to the distance it travels x and the velocity V. Note that the velocity of each layer is given as a function of rayangle θ to account for velocity anisotropy.

Assuming raypaths are straight within a given layer, a ray can be traced from a provided source location across layer boundaries to the desired horizon and back again to the surface. A schematic example is shown in Figure 2.18. Refraction at the interface between two layers is described via Snells law

$$\frac{sin(\theta_1)}{V_1} = \frac{sin(\theta_2)}{V_2}, \tag{2.17}$$

where θ is the angle of incidence, measured from the normal to the interface and V the P-wave velocity of each media. Note that the subscripts corresponding to a ray travelling across a boundary from media 1 to media 2. If the velocity model is not homogeneous within each layer, ray travel times are calculated by integrating over the ray velocity V via:

$$t = \int_{x_1}^{x_2} \frac{1}{V(\theta)} dx \approx \frac{x_2 - x_1}{n} \sum_{k=1}^{n} \frac{1}{V_k(\theta)}, \tag{2.18}$$

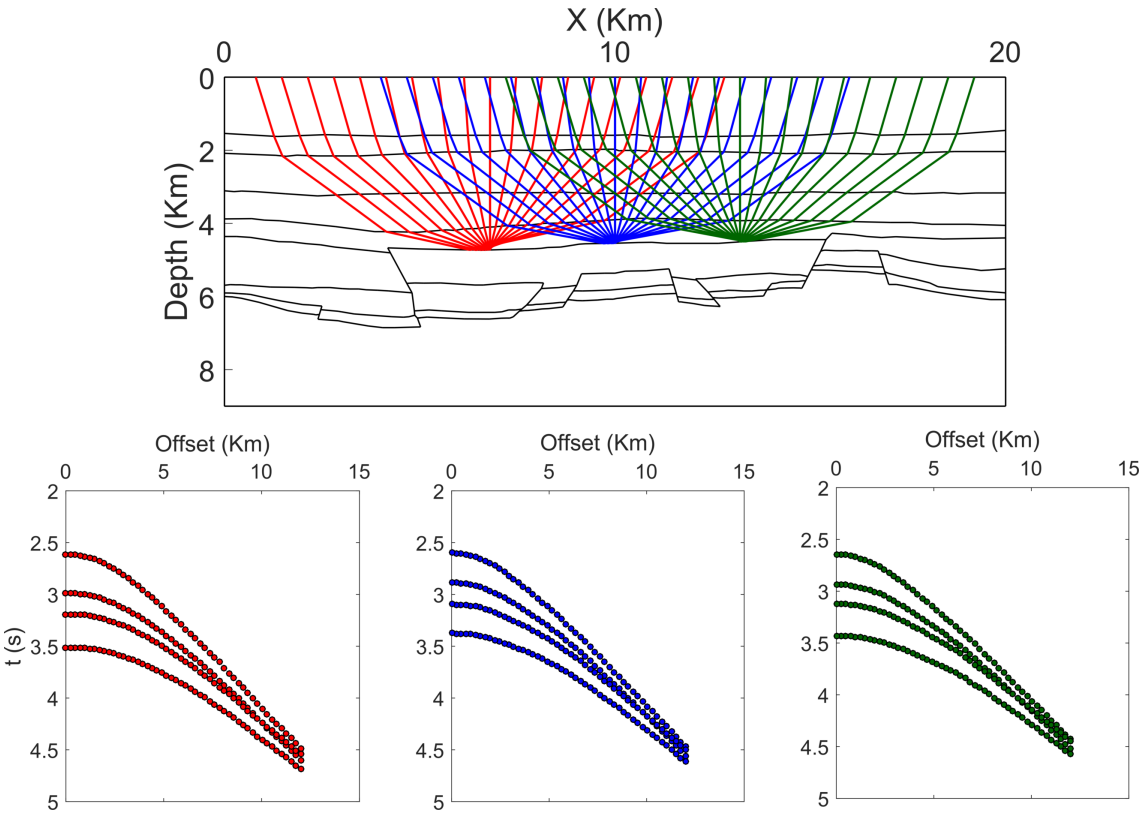

Figure 2.19: Three Common Midpoint (CMP) gathers (bottom) generated from raytracing the pre-production (i.e. base) P-wave velocity model (Figure 2.15) which is assumed to be isotropic. Each CMP is generated from 50 source receiver pairs, whose offsets range from zero to 12km. The two way travel time to the bottom of each overburden chalk layer is shown in the CMP gathers. For visual purposes, only 10 raypaths to a single horizon (bottom of chalk layer 5) are shown on the model geometry (top), however, the CMP gathers (bottom) show the travel times for the total 50 rays to each bottom chalk horizon.

where x corresponds to the distance travelled by the ray within each layer and n corresponding to the number of equally spaced points in which to discretized the definite integral. Velocities along the raypath $V_k(\theta)$ are determined by assigning it the velocity of closest nodal result found within the FE mesh.

It should be noted that the velocity $V(\theta)$ in equation 2.18 is written as a function of angle θ. This is because, assuming an anisotropic medium, the velocity of a seismic wave will differ depending upon the direction in which it is travelling. However, as the base (i.e. pre-production, 0 years) velocity model is assumed isotropic and homogenous, the velocity is constant for all values of θ.

Applying the raytracing methodology to the base velocity model of Figure 2.15 allows the generation of Common Midpoint (CMP) gathers. Figure 2.19 shows three CMP gathers created from 50 source receiver pairs, whose offsets range incrementally from zero to 12km. The reflection travels times to the base of each overburden chalk (i.e. overburden

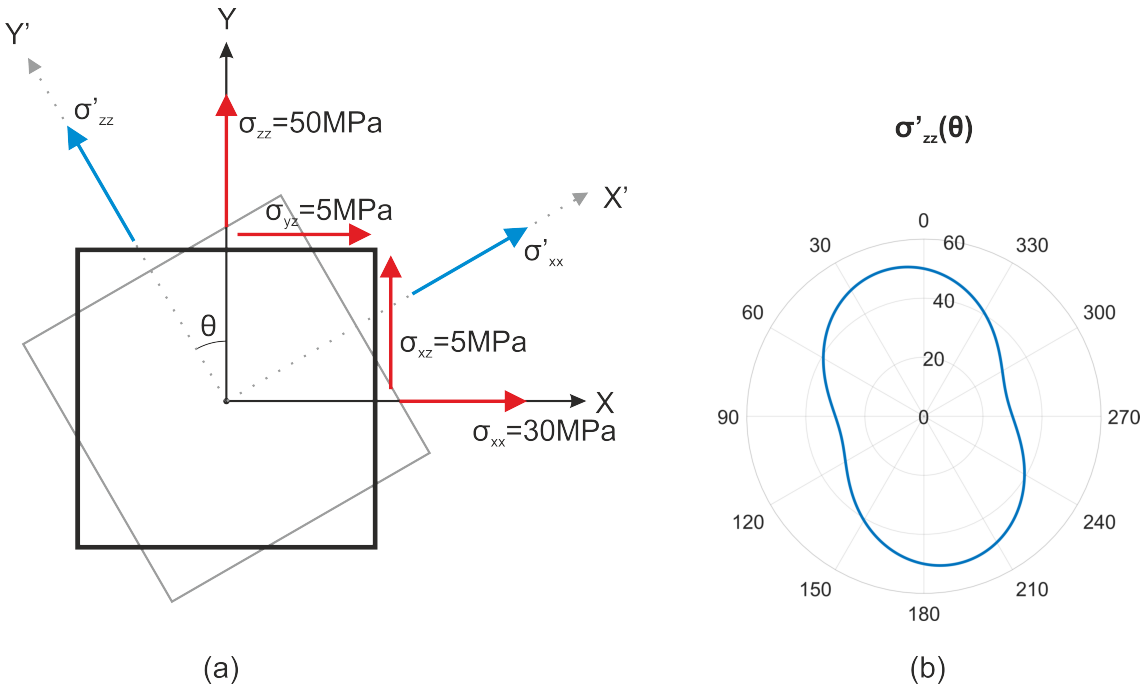

Figure 2.20: (a) Diagram demonstrating the stresses in an original coordinate system $X - Z$ transformed to another coordinate system $X' - Z'$ by the angle θ. (b) The rotated σ'_{zz} shown in MPa for all angles θ in the polar plot.

layers 3 to 6 in Table 2.1) are shown in each CMP gather. For visual purposes only 10 raypaths are drawn for each CMP in Figure 2.19, but the total 50 travel times used when plotting the CMP gathers.

The anisotropic change in effective stress as a result of production results in anisotropic velocity change. Thus, for monitor surveys, V becomes a function of θ as the velocity model becomes anisotropic. To determine the change in seismic velocity along a raypath, the effective stress change parallel to the raypath is determined and passed through the isotropic (constant for all values of θ) rock physics model (i.e. $dV/d\sigma' = 0.004 km.s^{-1}MPa^{-1}$). To determine the change in effective stress at an angle θ requires the rotation of the reference coordinate system. In 2-dimensions this stress rotation can be written in matrix form as:

$$\underbrace{\begin{bmatrix} \sigma''_{xx} & \tau'' \\ \tau'' & \sigma''_{zz} \end{bmatrix}}_{\boldsymbol{\sigma}''} = \underbrace{\begin{bmatrix} cos(\theta) & sin(\theta) \\ -sin(\theta) & cos(\theta) \end{bmatrix}}_{\mathbf{R}} \underbrace{\begin{bmatrix} \sigma'_{xx} & \tau \\ \tau & \sigma'_{zz} \end{bmatrix}}_{\boldsymbol{\sigma}'} \underbrace{\begin{bmatrix} cos(\theta) & -sin(\theta) \\ sin(\theta) & cos(\theta) \end{bmatrix}}_{\mathbf{R}^T} \tag{2.19}$$

where $\boldsymbol{\sigma}'$ are the effective stresses of your reference coordinate system (i.e. the results of the hydromechanical model) and $\boldsymbol{\sigma}''$ the stresses in your rotated coordinate system (i.e. along the raypath). Note that σ_{zz} corresponds to the vertical stress whilst σ_{xx} the horizontal. The stress rotation is demonstrated in Figure 2.20. It should be noted that by assuming an isotropic rock physics model, the production induced velocity anisotropy

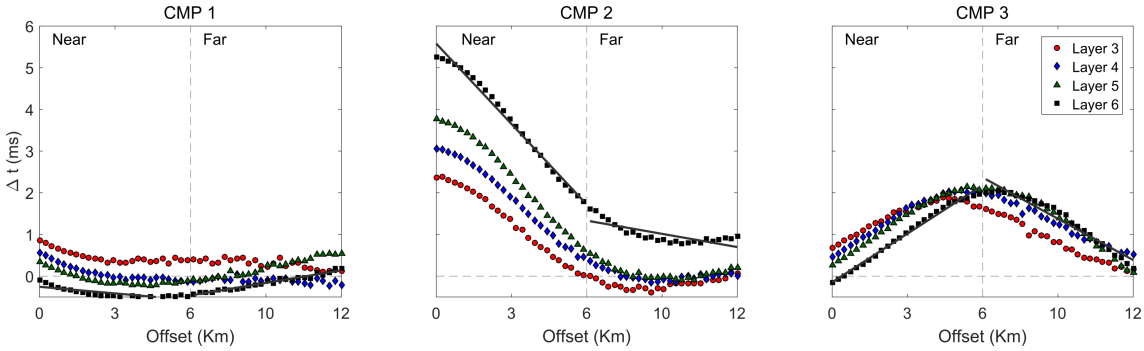

Figure 2.21: Time-shift as a function of offset for each of the three CMPs of Figure 2.19 after 20 years of production. The rate of change of time-shift with offset $d\Delta t/dX$ for near ($< 6km$) and far ($> 6km$) offsets calculated by linear regression. For visual purposes only the regression results are shown for Layer 6 (i.e. bottom of Chalk layer 6), the full set of results can be found in Table 2.2.

Horizon N°	$d\Delta t/dX$ (ms.Km^{-1})					
	CMP 1		CMP 2		CMP 3	
	Near	Far	Near	Far	Near	Far
Horizon 3	-0.0655	-0.0507	-0.4416	0.0305	0.1931	-0.2658
Horizon 4	-0.0999	-0.0168	-0.4908	-0.0307	0.2890	-0.2732
Horizon 5	-0.0721	0.1220	-0.5721	-0.0449	0.3410	-0.3794
Horizon 6	-0.0531	0.1003	-0.6433	-0.1057	0.3882	-0.3303

Table 2.2: The rate of change of time-shift with offset $d\Delta t/dX$ for each horizon in each CMP gather shown in Figure 2.21.

can be considered directly related to the anisotropic change in effective stress as opposed to any anisotropy in the rock physics model.

Repeating the raytracing procedure after the start of production by performing the relevant stress rotations enables the time-shifts to be analysed as a function of offset. However, the relatively large R factor values observed (e.g. Figure 2.16) indicate a significant proportion of the vertical time-shifts are a result of changes in velocity (i.e. effective stress). Therefore, the raytracing is simplified by assuming negligible horizon subsidence (i.e. no displacements) and all time-shifts a direct result of changes in effective stress.

The time-shift offset relationship for each CMP location after 20 years of production is shown in Figure 2.21. Directly above the reservoir region (i.e. CMP location 2) the time shifts clearly decrease with offset. The increased influence of the horizontal stress σ'_h, which is seen to increase directly above the reservoir, results in a much smaller time-shift at large offsets. At the CMPs located at the flanks of the reservoir (i.e. 1 & 3 in Figure 2.19), more complex time-shift offset relationships are recorded. The negative correlation between the change in σ'_v and σ'_h on the velocities making the time-shifts relatively constant

with offset.

To describe the time-shift offset relationship, the rate of change of time-shift with offset $d\Delta t/dX$ is calculated by linear regression. Due to the relatively complex relationship, $d\Delta t/dX$ is calculated separately for near ($< 6km$) and far ($> 6km$) offsets. The $d\Delta t/dX$ results for each chalk horizon in each CMP gather is provided in Table 2.2.

It should be noted that this raytracing methodology assumes straight ray paths (within each layer) and that interface refractions adhere to Snells law, which is derived only for isotropic media. However, for the purpose of this study I assume these simplifications to provide an adequate prediction of seismic travel times.

2.11 Summary

- I have developed a synthetic hydromechanical model of a HPHT production scenario in the North Sea which gives realistic results within a reasonable time-frame.
- I have created a suitable workflow for forward modelling seismic time-shifts from the modelled geomechanical results.
- I have discussed, in detail, the process of parameterising the hydromechanical model and outline how this is typically carried out in industry for real world scenarios. I also discuss the difficulties involved in this process and where varying forms of uncertainty can enter the workflow, indirectly highlighting why model benchmarking i.e. history matching, is of great importance.

3 . Multi-Method Sensitivity Analysis

A good means to discovery is to take away certain parts of a system and to find out how the rest behaves
George Christoph Lichtenberg

3.1 Introduction

Hydromechanical models are complex and highly nonlinear. Before a seismic history match can be successfully attempted, it is important to have an in depth working knowledge of your model's behaviour. For complex simulators with a high dimensional input space, it is common to find that a significant proportion of the variation to a certain output can be explained by a small subset of inputs. These inputs are often referred to as the *active* variables and have the greatest influence in explaining the variation to a specific model output. Determining these active variables and the extent of their influence over the output is important information for conducting a robust history match. Often it is found that identifying a suitable set of active parameters is sufficient to yield an acceptable match between model output and a set of historical observations. The investigation into a numerical model's behaviour is known as a Global Sensitivity Analysis (GSA). It provides a coherent mathematical methodology to determine active variables and their influence on the model output. The results provide important information to support model history matching and diagnostic evaluation.

In this chapter I conduct a multi-method GSA on over 4000 model perturbations of the hydromechanical model designed in Chapter 2. The results of the GSA are used to evaluate the potential geomechanical information content of time-lapse seismic data (i.e. in respect to model inputs) and get a first look at the complexity of the model space. Specifically, via the GSA, I examine the sensitivity of predicted overburden seismic time-shifts to the various properties of a single unknown overburden chalk layer. As part of the GSA I attempt to screen model parameters with negligible influence (i.e. *inactive* variables), rank those that are most influential (i.e. *active* variables) and develop an understanding of the model space (i.e. mapping). Initially, I focus the GSA on near-offset time-strains but then extend the analysis to include the time-shift offset relationship.

3.2 Global Sensitivity Analysis Methods

Many different sensitivity analysis methods exist; each technique being well documented in literature. An in depth examination into different sensitivity analysis methods is beyond the scope of this research. However, it is important to understand that choosing the most appropriate method is problem specific. The most suitable method depends on the question that needs to be addressed (i.e. screening, ranking or mapping), the number of model evaluations available and the characteristics of the problem at hand.

Typically, as the number of model inputs increase, the number of model runs required to perform a robust sensitivity analysis increases. However, the ratio between the number of parameters and model runs vary from one technique to the other. Also, the linearity between the input-output relationship and the characteristics of the output distribution (i.e. skew) will render some methods more suitable than others due to their statistical derivation. For a comprehensive insight into the mathematical concepts of the most widely used techniques and their key assumptions, advantages and limitations, the reader is directed to the study of Pianosi *et al.* (2016).

In this study I choose to employ a multi-method approach in which I use a total of four different GSA methods. Using a number of different methods creates a more robust analysis in which each approach defines and measures sensitivity differently, capturing different aspects of the models response. This results in different, yet complimentary, sensitivity measures for the same input factor. Also, by using a range of techniques, it permits the ability to address a number of different questions (i.e. screening, ranking and mapping).

In this study I use a total of four different GSA methods, the Elementary Effects Test (EET), Variance-Based Sensitivity Analysis (VBSA) and a two density based approaches, Regional Sensitivity Analysis (RSA) and PAWN. In this section I introduce these four techniques and discuss how the VBSA and PAWN methods are modified such that they can be applied to the same dataset as that of the RSA. This avoids additional model runs through tailored sampling strategies. Each of these four GSA methods, are described in greater detail in Petropoulos & Srivastava (2016).

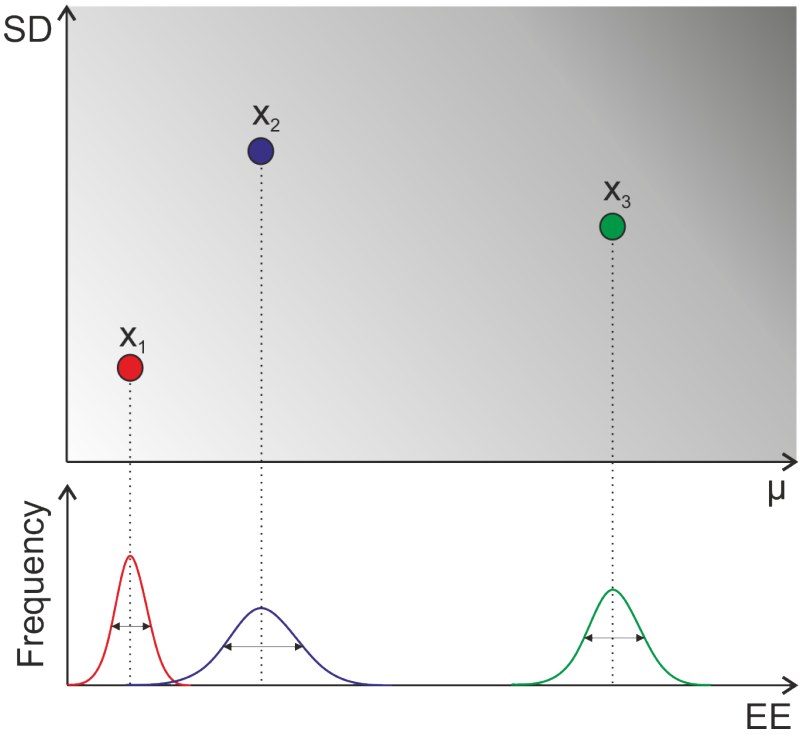

Figure 3.1: Elementary Effect (EE) distributions of three different parameters x_1, x_2 and x_3. A large (absolute) measure of the central tendency (i.e. mean value μ), indicates an input with an important direct influence on the model output, whilst, a large spread (i.e. standard deviation SD) indicates an input with a strong nonlinear effect. Therefore, parameters that fall within the top right hand section of an EE μ-SD plot are most influential to the model output.

3.2.1 Elementary Effects Test (EET)

The Elementary Effects Test (EET) (Morris, 1991), calculates an effect per input from a one-factor-at-a-time (OAT) sample matrix, $\mathbf{x}$:

$$x_{j,k} = \begin{pmatrix} x_{1,1} & x_{1,2} & \cdots & x_{1,k} \\ x_{2,1} & x_{2,2} & \cdots & x_{2,k} \\ \vdots & \vdots & \ddots & \vdots \\ x_{j,1} & x_{j,2} & \cdots & x_{j,k} \end{pmatrix}, \tag{3.1}$$

where, k is equal to the total number of parameters and $j = k + 1$ representing an independent sample or model run. The sample matrix $\mathbf{x}$ is ordered such that its first row (i.e. $j = 1$) is a randomly sampled set of model parameters whilst its j-th row differs in only the $(j-1)$st element. An Elementary Effect (EE) is calculated for each parameter k via:

$$EE_i = \frac{|Y_{i+1} - Y_1|}{(|x_{i+1,i} - x_{1,i}|)}(a_i - b_i) \qquad for \quad i = 1, ..., k, \tag{3.2}$$

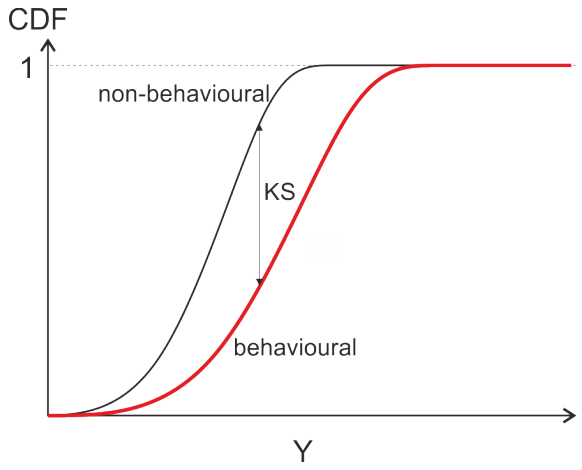

Figure 3.2: Cumulative Density Functions (CDFs) of behavioural and non-behavioural samples. Different criterion can be used to define behavioural regions of the parameter space. Typically behavioural samples are those which minimise a pre-defined objective function such as the difference between measured and observed data. The Kolmogorov-Smirnov (KS) statistic, describes the difference between the two CDFs, which in this study we take to be the maximum difference. The larger the KS statistic the larger the Regional Sensitivity Analysis (RSA) indice.

where $\mathbf{Y}$ is a $1\times j$ matrix of each independent model result and $\mathbf{a}$ and $\mathbf{b}$, $1\times k$ matrices that define the maximum and minimum sample ranges for each parameter k respectively.

Repeating this procedure, generating an ensemble n of $\mathbf{x}$ matrices, builds a finite distribution of n EE's per parameter k i.e. $EE_{n,i}$. To build a distribution of n elementary effects per input k would require n different $\mathbf{x}$ matrices and hence $n(k+1)$ model runs. A large (absolute) measure of central tendency in these EE distributions indicates an input with an important '*overall*' influence on the output whilst, a large spread indicates an input with an important nonlinear effect (i.e. it is heavily affected by the values of other inputs and their interactions). This is shown schematically in Figure 3.1. Note that the EET requires a tailored sampling strategy for the generation of the sample matrix $\mathbf{x}$.

3.2.2 Regional Sensitivity Analysis (RSA)

Regional Sensitivity Analysis (RSA) (Spear & Hornberger, 1980) requires the separation of the input space into '*behavioural*' and '*non-behavioural*' regions. Formally, the set X_b of behavioural inputs is defined as:

$$X_b = \{x | y_i = f_i(x) \leq \bar{y_i} \text{ for all } i\}, \tag{3.3}$$

where $\mathbf{x} = [x_1, ..., x_k]$ is the vector of all k input parameters, y_i either model output or an objective function (i.e. models fit to observed data) and $\bar{y_i}$ a predefined threshold value. Note that this particular criterion lends itself to assigning behavioural inputs as those that

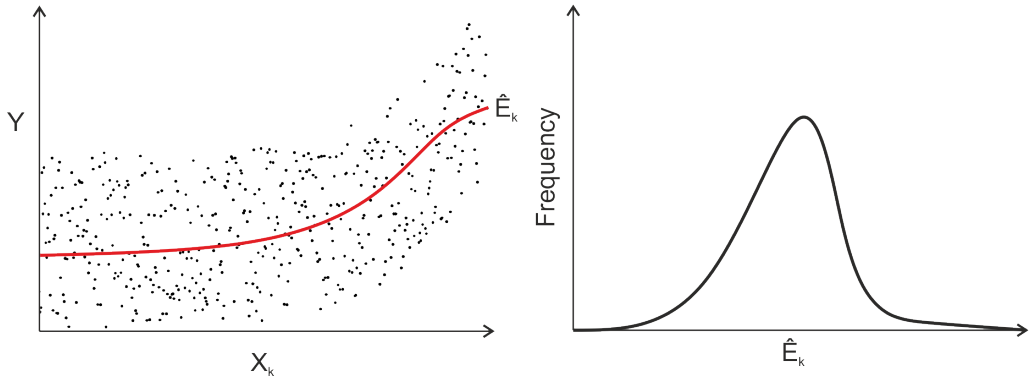

Figure 3.3: A linear combination of Radial Basis Functions (RBFs) $\hat{E}_k$ is used as a regression function for the input-output (i.e. $x_k - Y$) dataset (left). The optimized regression function is then evaluated at all values of x_k and the variance of $\hat{E}_k$ (right) used to approximate the term $V_{x_k}[E_{x_{\sim k}}(y|x_k)]$ in equation 3.6.

minimise a pre-defined objective function (i.e. distance between measured and observed data). However, different, less harsh criterions can be defined, such that behavioural inputs can be defined such that they meet only one of many pre-defined threshold values. For this study I define behavioural samples to be those which show absolute differences from the data of less than the average absolute difference seen across the whole ensemble.

Once the input sample is decomposed, sensitivity is measured by comparing the marginal Cumulative Density Functions (CDF's) of the two groups. Specifically, the sensitivity is defined by means of the Kolmogorov-Smirnov (KS) statistic. The sensitivity index for the k-th input factor x_k is expressed as:

$$S_k = \max_{x_k} |F_k^B(x_k) - F_k^{\bar{B}}(x_k)|, \tag{3.4}$$

where $F_k^B(x_k)$ and $F_k^{\bar{B}}(x_k)$ are the behavioural and non-behavioural CDF's respectively. A schematic demonstrating the KS statistic of two different CDF's is shown in Figure 3.2. The larger the distance between the two CDF's (i.e. the larger the KS statistic) the greater the sensitivity. Note that, unlike the EET, the RSA does not require a tailored sampling strategy but only a generic input-output dataset.

3.2.3 Variance Based Sensitivity Analysis (VBSA)

Variance-Based Sensitivity Analysis (VBSA) assigns a sensitivity indice to each input parameter based upon its contribution to the variance of the model output (Sobol, 1990). The direct contribution of the k-th input factor to the variance of the output is defined

as:

$$S_k = \frac{V_{x_k}[E_{x_{\sim k}}(y|x_k)]}{V(y)}, \tag{3.5}$$

where E is the expected value, V the variance and $\mathbf{x_{\sim k}}$ a vector of all inputs factors but the k-th. S_k can be described as the reduction of the total model output variance $V(y)$ that would be observed on average when the uncertainty about x_k would be removed by setting x_k to a fixed value (Tarantola, 2002). Since an analytic solution to equation 3.5 is typically impossible, numerical approximations are often used (e.g. Saltelli *et al.*, 2010) which require tailored sampling techniques. However, Petropoulos & Srivastava approximate equation 3.5 such that is can be used on a generic input-output dataset. They approximate $E_{x_{\sim k}}(y|x_k)$ as a linear combination of Radial Basis Functions (RBF),

$$\hat{E_k} = \sum_{j=1}^{n}[a_j exp(-(x_k - w_j)^2)], \tag{3.6}$$

where a_j and w_j are parameters that define the shape of the RBF. The variance $V_{x_k}[E_{x_{\sim k}}(y|x_k)]$ in equation 3.5 can now be approximated by the sample variance of $\hat{E_k}$ whilst $V(y)$ approximated from the variance of the sample output y. To obtain $V_{x_k}[E_{x_{\sim k}}(y|x_k)]$ operationally for each input factor the steps are (1) calibrate the regression function of equation 3.6 by calculating the best fit parameters a_j and w_j (in this case I use a linear combination of 5 RBF's, thus $j = 1, ..., 5$), (2) evaluate the optimized regression function for all values of x_k and finally, (3) calculate the sample variance of $\hat{E_k}$. A schematic example of this methodology is shown in Figure 3.3.

3.2.4 PAWN Sensitivity Analysis

PAWN (Pianosi *et al.*, 2015b) is a density-based method where sensitivity is measured by estimating the variation to the output y distribution when removing the uncertainty in one or more parameters x_k. This variation is calculated from the measure of distance between the unconditional (when all inputs vary simultaneously) and conditional (when all inputs vary but x_k, which is set to a nominal value) CDFs. The PAWN sensitivity index for the k-th input is defined as:

$$S_k = \max_{x_k} \max_{y} |F_y(y) - F_{y|x_k}(y|x_k)|, \tag{3.7}$$

where $F_y(y)$ and $F_{y|x_k}(y|x_k)$ are the unconditional and conditional CDFs of the output. The inner maximum of equation 3.7 defines the maximum absolute difference between the two CDFs approximated via the KS statistic using empirical distribution functions. As the KS statistic will depend on the nominal (i.e. fixed) value of x_k, the outer maximum of equation 3.7 extracts the maximum KS statistic over all values of x_k. If the dataset

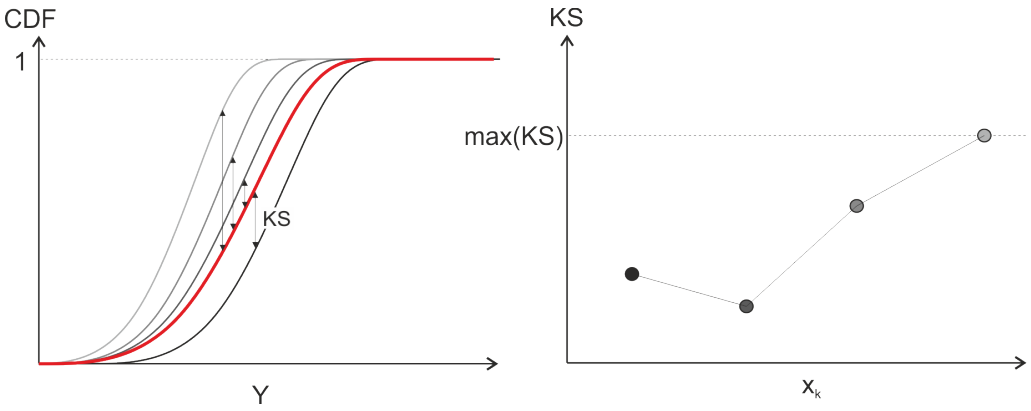

Figure 3.4: Red line (left image) indicates the unconditional (when all inputs vary simultaneously) CDF whilst shaded lines the conditional CDFs (all inputs vary but x_k) when x_k is fixed at incremental nominal values. The KS statistic (see caption for Figure 3.2) is computed for each unconditional-condition CDF pair and the PAWN sensitivity indice taken as the maximum KS value for the input x_k (right).

does not contain multiple samples with the same value of x_k, i.e. a generic input-output dataset, conditional distributions can be conditioned on 'similar' values of x_k. Therefore equation 3.7 can be approximated as:

$$S_k = \max_{j=1,\ldots,n} \max_{y} |F_y(y) - F_{y|x_k}(y|x_k \in \alpha_j)|, \tag{3.8}$$

where α_j are n (e.g. 10) equally spaced intervals over the range of variation of x_k. A schematic example of this method is shown in Figure 3.4.

3.3 Experimental Set-up

3.3.1 Defining the Model Space and Output

I consider a single unknown overburden chalk layer (layer 5 in Table 2.1 and highlighted in Figure 3.5) whose material properties are largely uncertain. As discussed in Chapter 1, it is assumed that there is little *a priori* knowledge of the overburden chalk properties. Therefore, large, uniform, independent uncertainty distributions are considered for all its physical parameters. The production profile (Figure 2.11) and mechanical properties of the reservoir and underburden are assumed known. In other words, known to greater degree of accuracy (i.e. much smaller uncertainty) than that of the overburden chalk. Thus, their properties are kept constant and not considered in the GSA.

In total, 21 different input factors are subjected to the GSA, each a material property of the overburden chalk. A summary of these parameters is presented in Table 3.1 along with their range of uncertainties. These uncertainty ranges are chosen based on typical

N^0	Parameter	Nomenclature	Equation N^o	Truth Value	Range	
					Min	Max
1	K_{xy}	Vertical-Horizontal stress coef		0.6	0.4	1.1
2	ΔP_p (Mpa)	Over/under-pressure		20	0	+40
3	ρ_f (g.cc^{-1})	Fluid density		1.02	1	1.2
4	ρ_g (g.cc^{-1})	Grain density		2.71	2.6	2.8
5	λ	Cam-clay constant	eqs. 2.6 & 2.7	0.06	0.02	0.1
6	κ	Cam-clay constant	eqs. 2.6 & 2.7	0.008	0.002	0.012
7	E_{ref} (Mpa)	Reference Young's Modulus	eq. 2.10	30500	1×10^4	3.3×10^4
8	n	Elastic constant	eq. 2.10	0.02	0.001	0.1
9	A/B	Elastic constant	eq. 2.10	-0.2758	0	-0.5
10	c	Elastic constant	eq. 2.10	-0.1	-0.5	-0.001
11	ν_{max}	Max Poisson's ratio	eq. 2.11	0.33	0.2	0.4
12	ν_{ratio}	Min Poisson's ratio	eq. 2.11	1	1	1.5
13	m	Elastic constant	eq. 2.11	1	0.01	1
14	α	Biot constant		1	0.5	1
15	K_0 (m^2)	Permeability constant	eq. 2.12	1×10^{-22}	1×10^{-23}	1×10^{-18}
16	x	Permeability constant	eq. 2.12	3	1	4
17	y	Permeability constant	eq. 2.12	2	1	6
18	K_s (Mpa)	Grain stiffness		2400	2400	5000
19	K_f (Mpa)	Fluid stiffness		13×10^4	8×10^4	15×10^4
20	Φ_{init}	Initial porosity	eq. 2.8	0.06	0.01	0.23
21	Φ_{ref}	Reference porosity	eq. 2.8	0.3	0.3	0.5

Table 3.1: Chalk layer physical properties and their parameter sensitivity ranges.

properties presented in the generic material database of Rockfield Software Limited and are made as wide as possible. Most of these parameters are described in greater detail in the definition of an elastoplastic material found in Chapter 2 Section 2.4. However, to ease GSA parameter space sampling, the poro-elastic parameters A and B (equation 2.10) are considered equal (for simplicity) and the minimum Poisson's ratio term υ_{min} (equation 2.11) replaced as a ratio υ_{ratio} of υ_{max}. Also, I assume that overburden rocks behave elastically during production, as production related stress changes in the overburden are generally small compared to the yield strength of the rock. Therefore, those parameters that define the shape of the state boundary surface are assumed to have no effect on the seismic travel times. However, the yield surface evolution parameters (e.g. λ and κ) are varied as they will affect the stress dependant porosity parameter in the elastic equation 2.10. It should also be noted that for the purpose of this study it is assumed that all unphysical, or algorithm specific (e.g. coupling rate, mesh type and size, etc.) parameters are optimized and are not considered in the GSA. The parameter ranges presented in Table 3.1 result in *in situ* Young's Modulus values roughly between 1×10^4MPa and 30×10^4MPa and Poisson's ratio values within the range 0.15 and 0.4.

The outputs analysed by the GSA are the individual overburden layer vertical time-strains $\Delta t_v/t_v$ (as seen in Figure 2.16) and the time-shift offset relationship $d\Delta t/dX$ (as

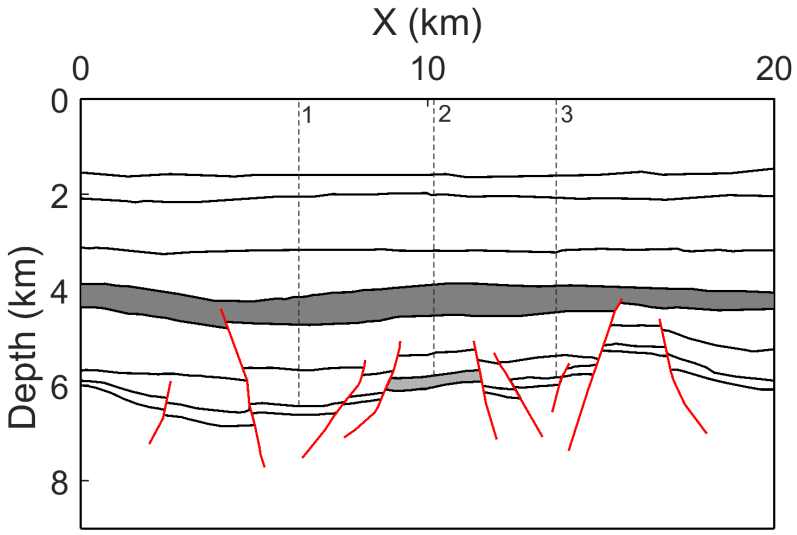

Figure 3.5: Model geometry with the chalk layer whose physical properties are deemed uncertain shaded in grey. Also shown are the three locations in which $\Delta t_v/t_v$ and $d\Delta t/dX$ measurements are calculated and used in the Global Sensitivity Analysis (GSA).

seen in Figure 2.21 and stated in Table 2.2). Specifically, $\Delta t_v/t_v$ and $d\Delta t/dX$ over each production year (i.e. 1 through to 20 years) at three separate locations within the main stress arching zone (highlighted in Figure 3.5). Only three locations are used as opposed to the entire model domain due to the computational expense of forward modelling $d\Delta t/dX$ through anisotropic raytracing. Although modelling $\Delta t_v/t_v$ is comparatively simple and quick, to maintain consistency and to be able to directly compare all results, the GSA only considers $\Delta t_v/t_v$ at the same three locations. These specific locations correspond to the same CMP positions in which the $d\Delta t/dX$ measurements were taken in Chapter 2 (i.e Figure 2.21).

Sensitivity indices are generated for each parameter by analysing each $\Delta t_v/t_v$ and $d\Delta t/dX$ output. Global sensitivity indices are presented by averaging the combined set of individual results. For example, the sensitivity of chalk layer 5 to a certain parameter will be the average of the three individual indices calculated at the three locations shown in Figure 3.5.

3.3.2 Sampling Methodology

A maximum Latin-Hypercube design is used to sample the model space of Table 3.1 (Forrester *et al.*, 2008). This approximately orthogonal design attempts to ensure model run locations are well spread out over the model space. Latin Hypercube sampling works by randomly combing a set of 1-dimensional samples, generated along each axes of the model space. Each parameter axis is divided into n equal partitions and a sample is

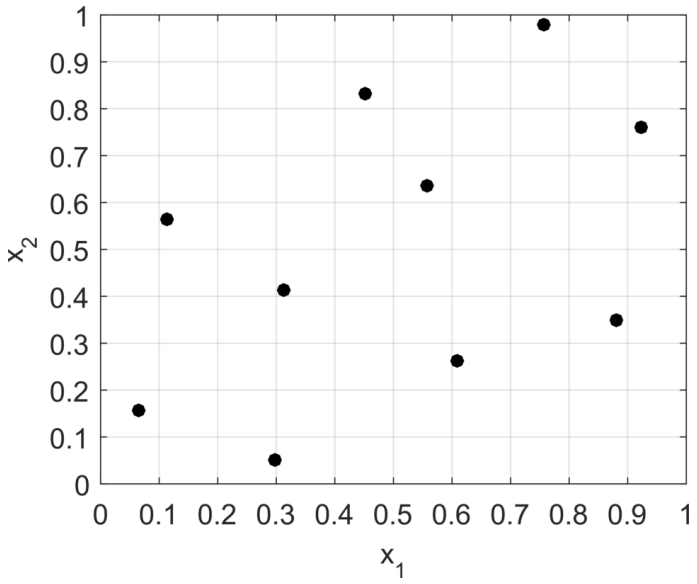

Figure 3.6: Latin hypercube sampling for a 2-dimensional parameter space. Each axis is divided into n equally spaced regions (n=10 in this case) in which a random sample is generated in each. The two sets of random samples are then combined randomly into two dimensional pairs.

generated randomly in each region. Each sub-region is sampled only once to ensure points are well distributed. An example is shown in Figure 3.6. A maximum Latin Hypercube design works by generating a large number of Latin Hypercube designs and choosing the one with the maximum minimum distance between all its sample points.

Latin-Hypercube sampling creates a generic input-output dataset. However, the EET method requires a tailored OAT sampling strategy. In this case, the radial design method of Campolongo *et al.* (2011) is used. An n point Latin Hypercube design is created such that a finite distribution of n EE's are created for each input factor. For each of the n points in the hyperspace a random walk is performed in each input dimension. Each walk is performed independently such that they originate from the same starting location. This ensures that each n Latin-Hypercube sample point will have k related samples (k being the number of dimensions of the input space) in which only differ by their location in a single dimension.

3.4 Results

Utilizing over 4000 model perturbations I conduct an in depth multi-method GSA using the SAFE Toolbox of Pianosi *et al.* (2015a). To begin with, I focus the GSA primarily on overburden $\Delta t_v/t_v$ measurements due to their relative ease to forward model. I initially use the EET on an ensemble of 1540 (i.e. n=70 EE's per input) model runs to screen those parameters (see Table 3.1) that have little affect over overburden $\Delta t_v/t_v$. I then create

an additional random ensemble of 3000 model runs with a reduced number of variable parameters. The RSA, PAWN and VBSA techniques are then applied to this dataset simultaneously to rank the most influential parameters in order of importance. Finally, the most influential (i.e. *active*) parameters are extracted and the condensed model space mapped to assess the potential constraint via seismic data. With these GSA results in mind I then utilise the same model perturbations to rank those parameters with the most influence over the shift-offset relationship $d\Delta t/dX$.

3.4.1 Near-offset Time-strains

Screening Model Parameters

Figure 3.7 shows the results of the EET analysis. Taking the three vertical locations shown in Figure 3.5 average EE measures are calculated for both the uncertain chalk layer and remaining overburden layers at 1 year intervals over the total 20 years of production.

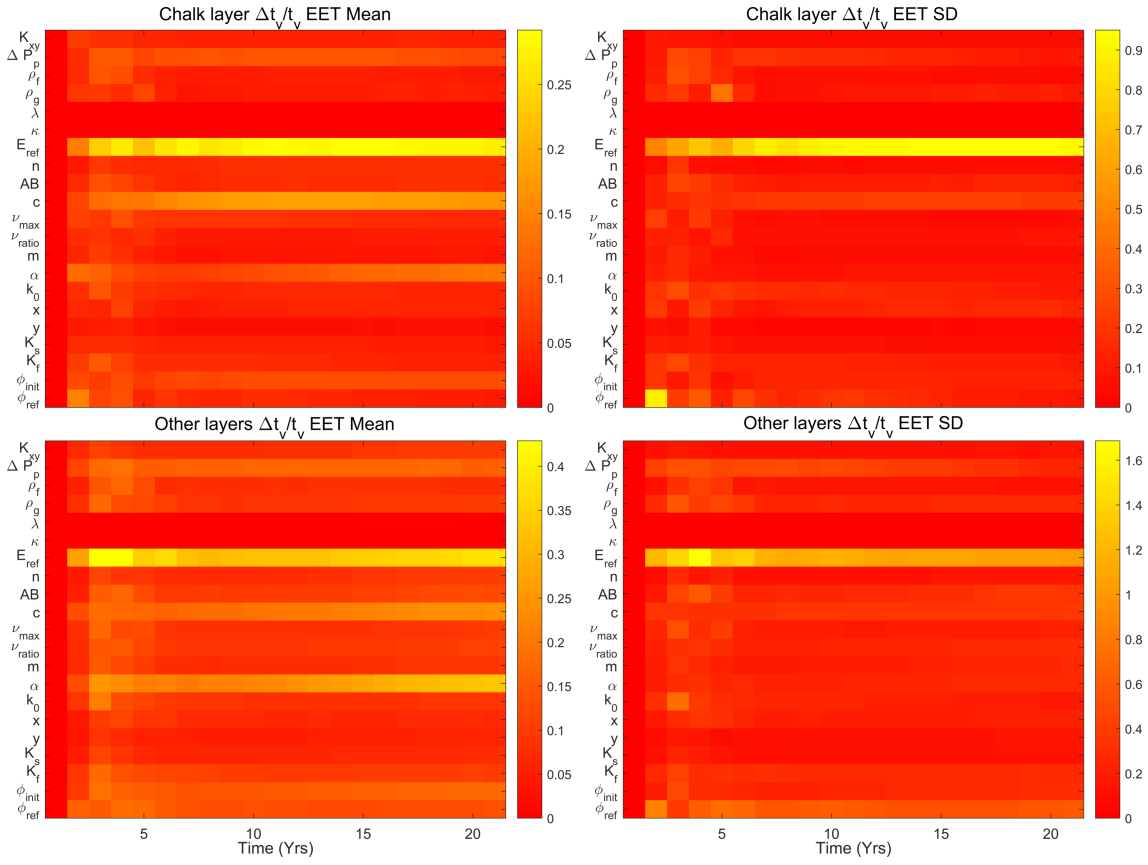

Figure 3.7: Time varying Elementary Effects (EEs) considering the resultant change in layer travel time $\Delta t_v/t_v$ at yearly intervals over the total 20 years of production. Results are computed considering the $\Delta t_v/t_v$ results of the uncertain chalk layer only and the $\Delta t_v/t_v$ result of the other (unchanged) overburden layers at the locations specified in Figure 3.5.

As discussed in Section 3.2.1, a large (absolute) measure of central tendency (i.e. mean), indicates an input with an important direct influence on the model output. A large spread (i.e. standard deviation), indicates an input with a strong nonlinear effect on the model output. Thus, parameters which show a significant shading (i.e. yellow in Figure 3.7) have a greater influence over the modelled $\Delta t_v/t_v$.

It is apparent from Figure 3.7 that altering the material properties of a single layer affects $\Delta t_v/t_v$ across the whole overburden. This demonstrates a complex nonlinear model behaviour. However, similar sensitivity patterns emerging across all overburden layers suggests the total modelled overburden $\Delta t_v/t_v$ could potentially be explained by a handful of model variables. Although Figure 3.7 suggest certain model parameters to be more influential than others it is difficult to conclusively screen a number of parameters as being non-influential. However, it is apparent from these results that the Cam-Clay parameters λ and κ do not affect the modelled $\Delta t_v/t_v$. Both parameters measure zero EE mean and standard deviation. This is not unexpected as they primarily affect the yield surface evolution (equations 2.6 and 2.7) and, as their influence is negligible, it confirms the assumption that the overburden remains elastic during production. However, their zero measure also suggests negligible influence over the stress dependant porosity parameter in equation 2.10. As a result, the Cam-Clay parameters λ and κ are screened and classed as non-influential but the remaining 19 parameters are all considered as potentially influential to $\Delta t_v/t_v$.

Ranking Model Parameters

To further investigate the influence of the remaining uncertain parameters on the modelled $\Delta t_v/t_v$ an additional 3000 different model input combinations are run. The same uncertainty ranges are used as those expressed in Table 3.1, but the Cam-Clay constants fixed to their true value.

I apply the RSA, PAWN and VBSA sensitivity techniques simultaneously to this input-output dataset to give complimentary parameter sensitivity indices. Figure 3.8 show the results of all three GSA methods focused on the final modelled $\Delta t_v/t_v$ (i.e. after 20 years of production). Note that here, a similar procedure is used as that of the EET by which sensitivity indices are summarized as average values for the uncertain chalk layer and remaining overburden layers over the locations shown in Figure 3.5.

A parameter with a greater sensitivity index indicates one which has a greater direct influence over $\Delta t_v/t_v$. It is apparent from Figure 3.8 that, although not giving exactly the same absolute measures of sensitivity, all three GSA techniques provide suitably similar global trends. Similar results are observed as to that of the EET analysis (Figure 3.7) where the parameters that control the non-linear elastic response (E_{ref}, c, ϕ_{init} of equation

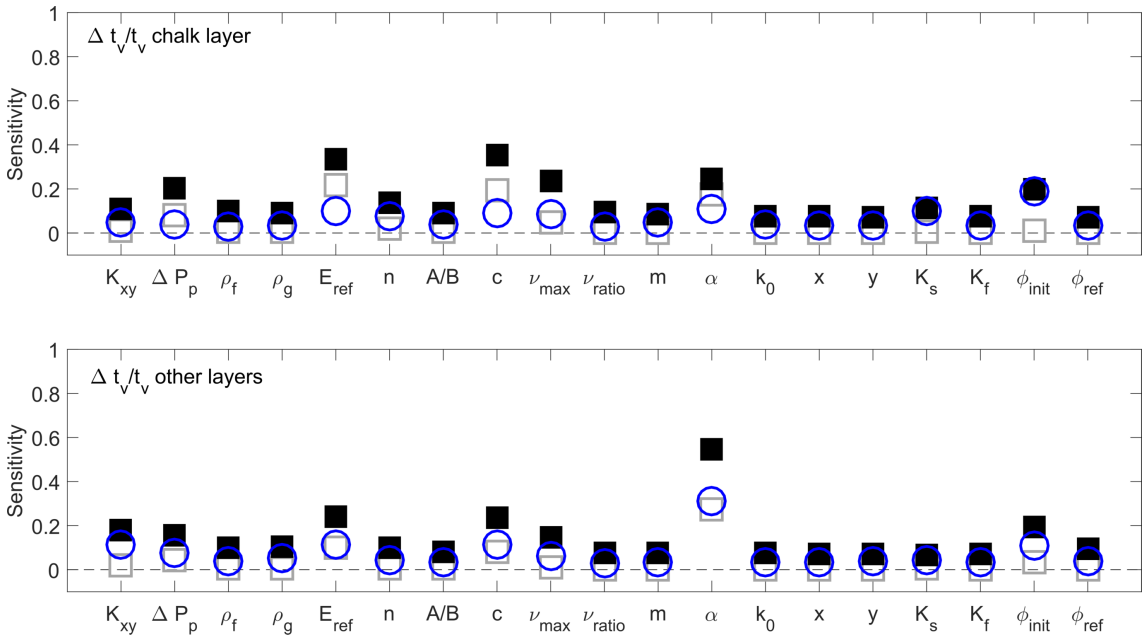

Figure 3.8: GSA sensitivity indices of the reduced set of model parameters. Blue circles represent the RSA results, black squares PAWN and grey hollow boxes the VBSA results. Sensitivity indices are computed considering the $\Delta t_v/t_v$ results of the uncertain chalk layer only and the results of the remaining (unchanged) overburden layers. These results focus on the final model $\Delta t_v/t_v$ i.e. after 20 years of production, at the locations highlighted in Figure 3.5.

2.10) and the Biot coefficient α are noticeably the most influential across all overburden layers. It is therefore fair to assume these to be the active parameters of this model.

Plotting the time-varying sensitivity indices of these parameters when considering $\Delta t_v/t_v$ of the chalk we can compare the influence of the elastic properties to α over production. The results are presented in Figure 3.9. Here, we see that the elastic parameters to be most influential during earlier production times but appear to be outweighed by α later in production. The initial erratic sensitivity indices recorded during early production years, i.e. years 1 and 2, are most likely due to the model not yet producing significant overburden $\Delta t_v/t_v$. This is demonstrated in Figures 2.12 and 2.13 in which little overburden stress and displacement is seen during the first two years of production. Therefore, it is assumed that these early measures of sensitivity are not truly reliable and should be treated with caution.

Mapping Data to Model Space

I take the 3000 model ensemble and compare these simulations to the result of the original (i.e. truth) hydromechanical model of Chapter 2. Assuming the overburden $\Delta t_v/t_v$ of the original model (Figure 2.16) to be observed data, I compare model residuals in the form of a $\Delta t_v/t_v$ Root Mean Square Error (RMSE). As time-lapse seismic data is time consuming

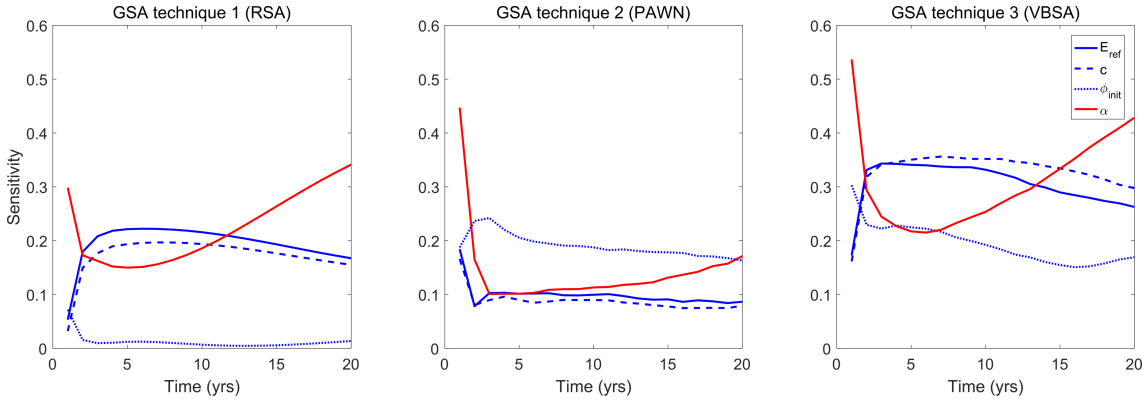

Figure 3.9: The time-varying GSA sensitivity indices of the four most influential parameters within the uncertain chalk layer. The elastic parameters are shown in blue whilst the Biot coefficient α in red.

and costly to acquire, shooting data at yearly intervals (or less) is generally unfeasible. Therefore, the RMSE is calculated considering the $\Delta t_v/t_v$ results at just three production time steps. The results of the GSA (Figures 3.7 and 3.9) suggest that the active variables do not start to significantly affect overburden $\Delta t_v/t_v$ till 3 years into production. With this in mind, they also show that the Biot coefficient α takes approximately 10 years to become as influential as the elastic coefficients (e.g. Figure 3.9). Taking this into consideration, the RMSE is calculated using the $\Delta t_v/t_v$ result at 3, 5 and 10 years. Note that the RMSE is calculated assuming the results from all 3 vertical locations shown in Figure 3.5.

Figure 3.10 show parallel coordinate plots of the best 5% (i.e. 15) of models whose $\Delta t_v/t_v$ measurements most closely resemble that of the data (i.e. original, truth model). These possess the lowest RMSE and are referred to as behavioural models. Also shown in Figure 3.10 are their corresponding $\Delta t_v/t_v$ logs (plotted just at location 2 of Figure 3.5) after 10, and 20 years of production. The results show that each behavioural models $\Delta t_v/t_v$ results closely resembles that of the data. Even their forward predicted $\Delta t_v/t_v$ values (i.e. after 20 years of production) are similar to those observed in the data. However, these models appear randomly scattered along the uncertain parameter range. Thus, models with significantly different active parameters each produce similar, possibly acceptable,

N^0	Parameter	Nomenclature	Equation N^o	Truth Value	Range	
					Min	Max
1	E_{ref} (Mpa)	Reference Young's Modulus	eq. 2.10	225	100	1000
2	c	Elastic constant	eq. 2.10	-1.28	-1.5	-0.001
3	α	Biot constant		1	0.5	1
4	Φ_{init}	Initial porosity	eq. 2.8	0.12	0.01	0.23

Table 3.2: Active parameters of the reservoir layer and their uncertain sensitivity ranges.

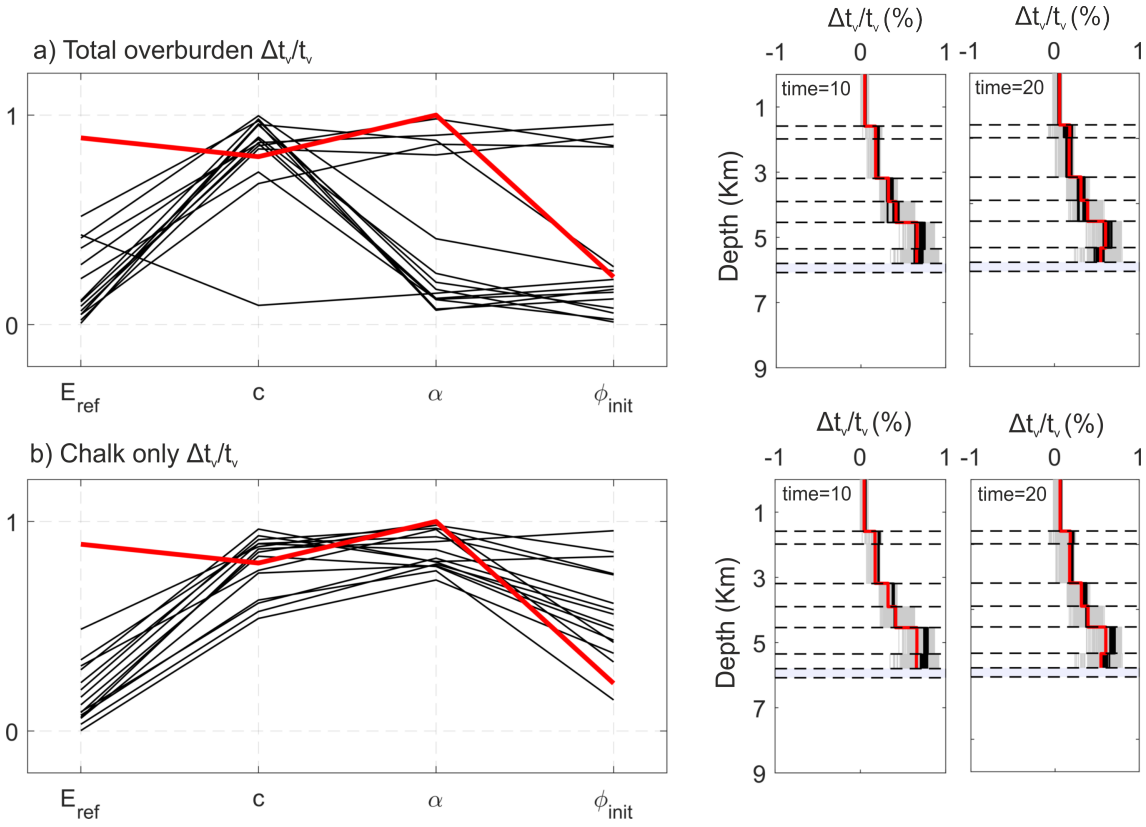

Figure 3.10: Parallel coordinate plots showing the active parameters of the best 5% (i.e. 15) of models whose $\Delta t_v/t_v$ results most closely resemble that of original, i.e. truth, model (e.g. Figure 2.16). Also shown are the corresponding models $\Delta t_v/t_v$ overburden logs after both 10 and 20 years of production. The original model results are highlighted in red, whilst the closest models in black. The overburden $\Delta t_v/t_v$ logs of the whole model ensemble shown in grey. The model residuals were computed by taking the Root Mean Square Error (RMSE) of the whole overburden $\Delta t_v/t_v$ results after 3, 5 and 10 years of production. Also shown are the results when only the uncertain chalk layers $\Delta t_v/t_v$ results are considered in the residual calculation.

solutions. This suggests a complex, possibly ill-posed, model space. If I simplify the objective function to the RMSE of just the uncertain chalk layers $\Delta t_v/t_v$ (i.e. ignoring the $\Delta t_v/t_v$ of other overburden layers), a slightly different result is observed (e.g. Figure 3.10). This optimization produces a different set of behavioural models which, as expected, do a better job of fitting the data of the uncertain chalk layer. These behavioural models also appear less scattered throughout the model space. Almost all of their active parameters, more closely resembling those of the original (i.e. true) model. However, these models contain a significantly lower value of the elastic coefficient E_{ref} (and as a result a lower pre-production Young's Modulus). Thus, significantly different model parameters still produce similar, possibly acceptable, solutions even with a simplified, condensed data space.

Figure 3.10 along with the sensitivity results of the GSA emphasise the complexity and non-linearity of the model behaviour. The uncertainty in a single overburden layers

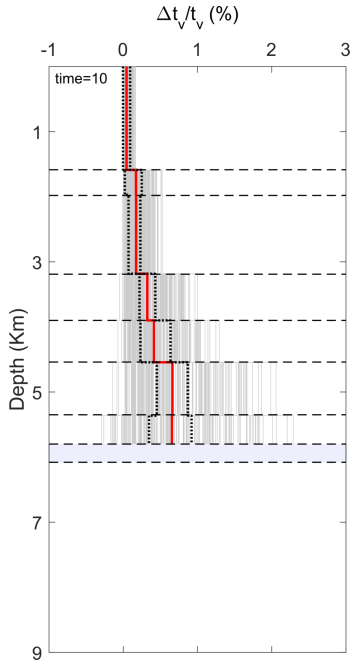

Figure 3.11: Overburden $\Delta t_v/t_v$ logs of the uncertain reservoir ensemble (Table 3.2) after 10 years of production shown via grey lines. The, truth model results are show in red (e.g. Figure 2.16) whilst the dotted lines represent the extreme values seen within the original GSA results (Figure 3.10).

material properties appears to affect the predicted $\Delta t_v/t_v$ across the whole overburden domain. Due to significant pore pressure changes, the reservoir undergoes far more extreme mechanical changes than the overburden during production. Thus, it is reasonable to presume that the uncertainty in the mechanical properties of the reservoir may, more heavily, influence overburden $\Delta t_v/t_v$ than similar uncertainty in overburden properties.

To test this hypothesis, I assume the mechanical properties of our reservoir to be uncertain, whilst holding the properties of the overburden constant (Table 2.1). Taking the four active parameters highlighted by the GSA, uniform, independent uncertainty distributions are assigned for their values in the reservoir. A summary of their uncertainty ranges are outlined in Table 3.2; their ranges similarly as large as that used for the overburden chalk layer in the GSA (Table 3.1). I run 200 different model input combinations and compute their overburden $\Delta t_v/t_v$ results. The $\Delta t_v/t_v$ values are again computed at the same locations as that used in the GSA (Figure 3.5).

Shown in Figure 3.11 are the corresponding overburden logs for each model run after 10 years of production. The results confirm the significant effect reservoir uncertainty has on overburden $\Delta t_v/t_v$. Its uncertainty appearing to influence overburden $\Delta t_v/t_v$ to a much greater extent than suitable similar uncertainty in overburden layers. It is important to note that the extreme mechanical changes seen in the reservoir could result in plastic

deformation. Thus, parameters which govern the rocks state boundary surface could potentially have significant influence. These parameters should be included if an in depth sensitivity study is to be undertaken for the reservoir region.

3.4.2 Time-shift versus Offset

The time-shift offset behaviour is believed to hold additional geomechanical information which is not contained within near-offset (i.e. vertical) shifts. At greater offsets, raypaths become increasingly more horizontal and the greater the influence of the horizontal velocity (i.e. stress) change. As such, the time-shift offset behaviour is seen to hold information regarding the rate and extent of the anisotropic stress change. This becomes of interest to seismic history matching as the shift versus offset relationship could hold additional information concerning other model parameters; those which are seen to not heavily influence near-offset shifts.

Re-applying the RSA, PAWN and VBSA sensitivity techniques on the modelled $d\Delta t/dX$ results of the 3000 model ensemble produce the results shown in Figure 3.12. Note that here, the GSA is focused on the $d\Delta t/dX$ output calculated from the difference in travel times to the bottom of chalk layer 5 (shown in Figure 2.19) after 10 years of production. This particular year is chosen, as opposed to the final model result (i.e. 20 years), due to

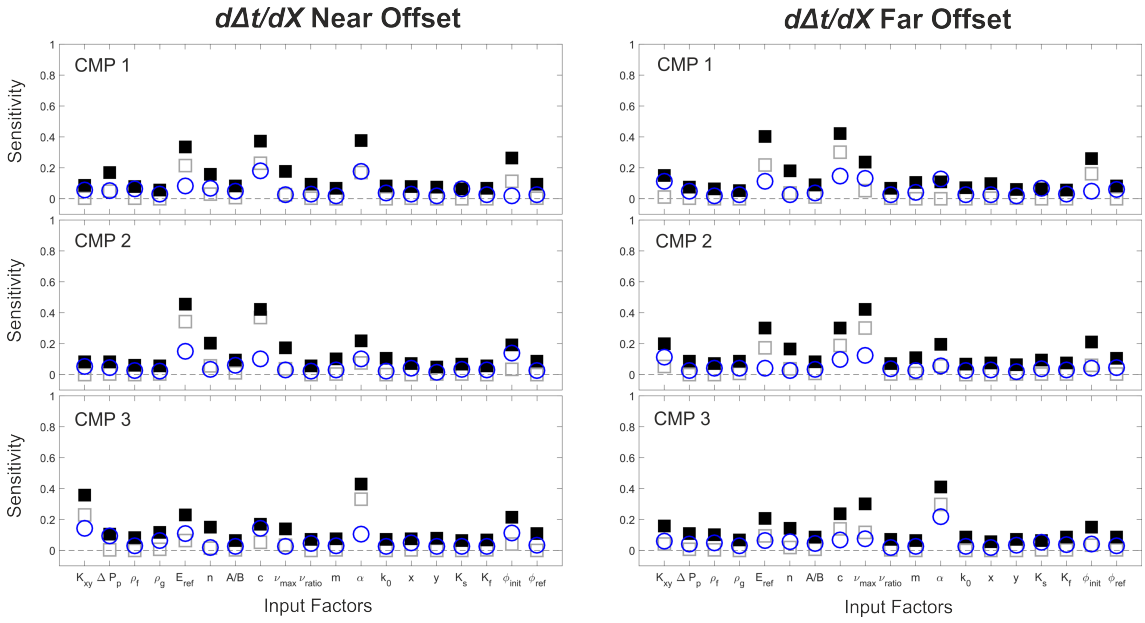

Figure 3.12: GSA sensitivity indices where blue circles represent the RSA results, black squares PAWN and grey hollow boxes the VBSA results. Sensitivity indices are computed considering the overburden chalk layer 5 $d\Delta t/dX$ results for the near ($< 6km$) and far ($> 6km$) offset response of each of the three CMP locations shown in Figure 3.5. These results focus on the $d\Delta t/dX$ response after 10 years of production.

the monitor surveys used in the history matching process likely being around this time in production. The CMP numbers labelled in Figure 3.12 correspond to the three locations shown in Figure 3.5. Sensitivity indices are computed considering the near (<6km) and far (>6km) offset response for each CMP gather.

It is apparent from Figure 3.12 that the parameters that control the non-linear elastic response (E_{ref}, c, ϕ_{init} of equation 2.10) and the Biot coefficient α appear to be the most influential to the $d\Delta t/dX$ response. This result is suitaby similar to the GSA results found when analysing the vertical time-strain $\Delta t_v/t_v$ (e.g. Figure 3.8). However, the parameter that controls the magnitude of the Poisson's Ratio ν_{max} also appears noticeably influential. Arguably, it becomes the most influential parameter for the far offset $d\Delta t/dX$ response.

3.5 Discussion

The results of the GSA highlight that out of an initial 21 model parameters, the modelled overburden seismic time-shifts are most heavily influenced by just 4 (e.g. Figures 3.7, 3.8 and 3.12), the Biot coefficient α and the parameters that govern a materials elastic behaviour E_{ref}, c and ϕ_{init}. The $\Delta t_v/t_v$ GSA also suggests that these variables take 3 years (from the start of production) to become significantly influential and that α takes approximately 10 years to become as influential as the elastic parameters (e.g. Figure 3.9). This time varying sensitivity demonstrates how acquiring multiple vintages of time-lapse seismic data could be advantageous. However, these results also suggest that significant overburden seismic time-shifts may take time to manifest. Thus, time-lapse seismic data taken shortly after the start of production may not be conclusive or reliable enough to aid the advanced numerical calibration of geomechanical models. However, acquiring early seismic data can be beneficial as an early warning system. It can highlight any large discrepancies between model and reality, and the potential case where there is likely no acceptable match suggesting the potential need to re-evaluate the simulator (e.g. the mechanical stratigraphy, mesh size etc.)

The elastic parameters being influential is not totally unexpected, as seismic travel times are affected by changes in stress and path length and thus governed by rock stiffness (i.e. Young's Modulus equation 2.10). However, slightly unexpected is the significant influence of the Biot coefficient α. Typically, the overburden is modelled as an undrained scenario (i.e. no fluid flow) in which you assume there is no production related pore pressure change. Therefore, you would expect α (i.e. $\sigma' = \sigma - \alpha P_p$) to have little influence over changes in effective stress and hence $\Delta t_v/t_v$ and $d\Delta t/dX$. However, ELFEN implicitly evaluates the pore pressure P_p of the whole model domain (i.e. whole domain coupling) as a function of α and the volumetric strain ϵ_v. Therefore, although there is no (or little) fluid flow outside of the reservoir, the pore pressure is affected by mechanical changes in

volumetric strain. The GSA demonstrates this and emphasises the importance of modelling fluid flow and pore pressure outside of the reservoir. Their slight instabilities can cause non-negligible effects to the model output.

The GSA results focused on $d\Delta t/dX$ show that the parameter that controls the magnitude of the Poisson's ratio ν_{max} becomes influential. Arguably, it becomes the most influential parameter for the far offset $d\Delta t/dX$ response. This is not overly unexpected as the Poisson's ratio governs the extent of the strain perpendicular the applied load and hence will indirectly influence the extent of the change in horizontal stress. This becomes interesting in terms of seismic history matching as the $d\Delta t/dX$ response can offer extra information regarding other model parameters which would have otherwise been overlooked. It also makes $d\Delta t/dX$ a potentially important observation in terms of providing information regarding the rate and extend of the anisotropic stress change.

The consequence of the material properties of a single layer affecting $\Delta t_v/t_v$ across the whole overburden demonstrates a complex nonlinear model behaviour. Thus, analysing model activity globally (i.e. across whole modelled domain), as opposed to locally, could be crucial for potential calibration. Although I highlight just 5 active parameters for the $\Delta t_v/t_v$ and $d\Delta t/dX$ results, it is also influenced, albeit to a lesser extent, by the remaining uncertainty in other parameters (e.g. Figure 3.8 and 3.12). Therefore it must be stressed that changes in overburden $\Delta t_v/t_v$ and $d\Delta t/dX$ are not entirely determined by changes in these 5 active variables. Thus, calibration procedures focussing on a condensed model space should also account for variations to model output caused by changes in less sensitive variables.

Models with significantly different input parameters produce similar $\Delta t_v/t_v$ results (e.g. Figure 3.10). This is the case when considering both global $\Delta t_v/t_v$ results (i.e. across the whole overburden) and when focused to local model output (i.e. results of uncertain chalk layer only). This highlights the complexity of the model space where a single global solution will most likely not exist. Instead, numerous models, of different input combinations will produce equally acceptable solutions (e.g. Figure 3.10). In this study we assume only the uncertainty of a single overburden layer. The complexity of the model space will undoubtedly increase when we consider the uncertainty in the mechanical properties of other layers. The GSA results do suggest that time-lapse seismic data could potentially be able to distinguish between certain models within our ensemble. The difference in layer Δt_v between certain models being on the order of 2-3ms. However, the size and complexity of the model space suggests seismic history matching will not be straightforward. The observation that models with significantly different inputs can yield relatively similar solutions (e.g. Figure 3.10) may hinder potential attempts to constrain parameters. It could be suggested that the material properties in ELFEN are

over-parameterised. Complex nonlinear relationships (e.g. equations 2.10, 2.11 and 2.12) generate undesirable additional complexity to the model space. Simplifying the material properties to purely constants may be beneficial to reduce complexity whilst producing suitable similar results.

I find that the uncertainty in the mechanical properties of the reservoir heavily influence overburden $\Delta t_v/t_v$ (e.g. Figure 3.11). Its uncertainty appearing to influence $\Delta t_v/t_v$ to a much greater extent than suitable similar uncertainty in the overburden (e.g. Figure 3.10). This demonstrates the nonlinearity of the model behaviour and the importance of a suitably accurate reservoir model. Time-lapse seismic calibration of other properties of a geomechanical model will thus only be possible once the reservoir behaviour is known to a suitable degree of accuracy.

It is important to note that the sensitivity measurements of the GSA are heavily affected by the uncertainty in model parameters. For example, considering a much smaller uncertainty range in the elastic coefficients would result in their sensitivity being significantly less than seen in this study. Therefore it is always important to cross analyse the results of the GSA with the uncertainty range used. It is also important to mention that in this chapter I have not accounted for random modelling errors (e.g. variations to the implicit and explicit solutions caused by the parameterisation of their solvers), which can act as noise or bias to the resulting output distributions. However, since large distributions are seen in $\Delta t_v/t_v$ (e.g. Figures 3.10 and 3.11) it is safe to assume these random modelling errors to be insignificant. It is also important to note the stress dependant rock physics model is not included in the GSA and is assumed known (i.e. no uncertainty). The uncertainty introduced by the rock physics model is looked at in greater detail in Chapter 4.

3.6 Summary

- Out of an initially large set of material properties, the modelled overburden $\Delta t_v/t_v$ is mainly affected by just 4 *active* parameters. These are the Biot coefficient α and the parameters that govern the materials elastic behaviour (i.e. stiffness).
- The same set of parameters is seen to cause the majority of the variation in $d\Delta t/dX$. However, the parameter that controls the magnitude of the Poisson's ratio also becomes significant. It becomes arguably the most influential parameter for the far offset $d\Delta t/dX$ response and hence can also be considered an active parameter for $d\Delta t/dX$.
- The influence of the Biot coefficient highlights the importance of modelling fluid flow and pore pressure outside of the reservoir i.e. whole domain coupling.
- A hydromechanical model is complex and highly non-linear. Altering the material properties of a single layer affects the time-shift results across the whole overburden domain.
- Multiple combinations of model parameters can yield equally possible model realisations. However, significant differences in the time-shift estimates between certain models within the ensemble suggests seismic data could be used in history matching to distinguish between different input combinations.
- Reservoir behaviour must be known to a suitable degree of accuracy before the benchmarking of other parts of the model, such as the overburden, can be attempted.
- Potential over-parameterisation of the material properties. Complex nonlinear porous and elastic relationships add complexity to the model space and will potentially make history matching more difficult. Simplification of the rock properties will most likely not effect model performance whilst potentially making seismic history matching more achievable.

4 . Analysis of Stress-dependant Rock Physics Models

In its efforts to learn as much as possible about nature, modern physics has found that certain things can never be known with certainty. Much of our knowledge must always remain uncertain. The most we can know is in terms of probabilities.
Richard Feynman

4.1 Introduction

Rock physics models are vitally important in the seismic calibration of hydromechanical models. They provide a method of modelling the influence of production related changes in stress and strain to seismic velocity and anisotropy (e.g. Angus *et al.*, 2015; Guilbot & Smith, 2002; Herwanger & Koutsabeloulis, 2011). Effectively, these models are based on the recognition that an increase in effective stress will result in a non-linear increase in seismic velocity due to closure of cracks, grain boundaries and discontinuities (e.g. Baird *et al.*, 2013a; Crampin, 2005; Nur & Simmons, 1969). The non-linear (i.e. exponential) behaviour a consequence of a greater number of more compliant cracks at lower effective stresses.

Many rock physics models have been derived to account for this non-linear relationship such as empirically determined relationships (e.g. Zimmerman *et al.*, 1986), third order elasticity theory (e.g. Korneev & Glubokovskikh, 2013; Prioul *et al.*, 2004), Hertz-Mindlin contact forces (e.g. Makse *et al.*, 1999), micro-structural models (e.g. Guéguen & Sarout, 2011; Hall *et al.*, 2008; Ougier-Simonin *et al.*, 2009; Sarout & Guéguen, 2008; Sayers, 2002; Tod, 2002) and relationships derived from first principles that are consistent with empirically derived equations (e.g. Shapiro, 2003, 2005). Typically, these models are constrained using ultrasonic velocity-stress core data obtained from laboratory experiments. The sensitivity of the velocity to stress is heavily dependent on rock architecture and hence rock lithology.

Thus far in this study, the velocity-stress dependence has been modelled via a simplified linear approximation ($dV/d\sigma' = 0.004 km.s^{-1}.MPa^{-1}$). Although this is a reasonable approximation considering typical core measurements and previous time-lapse studies (e.g. Angus *et al.*, 2009, 2012, 2015), up to this point it has been assumed constant with zero uncertainty. In terms of history matching, its uncertainty can be seen as a form of model discrepancy error δ. Even if the true physical properties are inserted into the model, a

significant discrepancy between the simulator output and the data would be observed if an inaccurate rocks physics model is defined.

In this Chapter I explore rock physics model uncertainty in greater detail. I take a number of commonly used models and vigorously assess their behaviour and stability when applied to stress versus velocity measurements of a large (dry) core dataset of different lithologies. Specifically, using a collection of ultrasonic velocity versus stress measurements I invert for various model parameters. I then critically analyse the fit of different models to the observed data and compare their time-lapse velocity predictions when subject to the hydromechanical model of Chapter 2. The inversion constraint is also simultaneously assessed using Bayesian style statistics. I then use the inversion results to derive parameter-porosity-clay relationships to assess the potential calibration of models when laboratory measurements are unavailable (i.e. calibrate models using rock properties measurable from wellbore data). Finally I discuss the implications of core damage and how representative velocity-stress core data is to *in situ* rocks.

Unfortunately, the core database used in this study contains no chalk rock. Finding comprehensive stress-velocity chalk measurements in literature is extremely difficult. The documented data is either inadequate (e.g. Borre & Fabricius, 2001) or not quantitative (e.g. Gregory, 1976) and hence it was not included in the final core database. However, I do collate what little chalk data is available in literature and demonstrate that the main results of this Chapter are relevant and applicable to chalk rock and hence the overall history matching study.

Up to this point, most references to seismic velocity have referred to the P-wave velocity. However, in this Chapter I also discuss S-wave velocity and hence introduce relevant subscripts (i.e. P and S) to distinguish between the two. Also, it should be noted that all references to stress in this Chapter refer to effective stress.

4.2 Rock Physics Models

There are many different rock physics models available, each aiming to relate changes in stress and strain to seismic velocity. However, since there are many different mathematical formulations, it is not feasible to collate and analyse each published relationship. Instead, I focus on the most common theorems and formulae used for hydrocarbon monitoring scenarios. A total of 5 different models are analysed: an empirical (EMP) model (e.g. Zimmerman *et al.*, 1986), a first principle (FPR) model (e.g. Shapiro, 2003), a micro-structural (MST) model (e.g. Schoenberg & Sayers, 1995) and two third-order elasticity (TOE) models (e.g. Korneev & Glubokovskikh, 2013; Prioul *et al.*, 2004).

It should be noted that the development of new cracks or the permanent deformation of pre-existing cracks and pores are not considered in certain models (i.e. no hysteretic behaviour). Although the influence of plastic deformation could be modelled using porosity-velocity relationships (e.g. Avseth *et al.*, 2010), these transforms may neglect important geomechanical effects such as shear-banding.

4.2.1 EMP Model

Zimmerman *et al.* (1986) propose that for an isotropic rock under an isotropic load the seismic velocity V_ν (where ν refers to either the P- or S-wave) can be related to the effective stress σ' via

$$V_\nu(\sigma') = A_\nu + K_\nu\sigma' - B_\nu \exp(-\sigma' D_\nu), \tag{4.1}$$

where A_ν, K_ν, B_ν and D_ν are material dependent coefficients (or fitting parameters) which can differ for P- and S-waves. If the effective stress is on the order of MPa (which is often the case for production scenarios), the second term in equation 4.1 becomes orders of magnitude less than the other two terms and thus can be neglected (e.g. Eberhart-Phillips *et al.*, 1989; Khaksar *et al.*, 1999; Kirstetter & MacBeth, 2001; Zimmerman *et al.*, 1986),

$$V_\nu(\sigma') = A_\nu - B_\nu \exp(-\sigma' D_\nu). \tag{4.2}$$

Equation 4.2 generally provides a good approximation for both dry and saturated rocks (e.g. Jones, 1995). This is due to the fact that the model fits an exponential curve to data that typically displays an exponential trend. However, this model is limited in that its material dependent coefficients lack any physical meaning and are often empirically determined (e.g. Eberhart-Phillips *et al.*, 1989).

4.2.2 FPR Model

Shapiro (2003) expands on the formulation of Zimmerman *et al.* (1986) by deriving physical meanings for the model coefficients A_ν, K_ν, B_ν and D_ν. Shapiro (2003) assumes that the stress dependence of porosity controls the change in elastic moduli and that the total porosity ϕ is a function of both compliant ϕ_c and stiff ϕ_s porosity terms,

$$\phi = \phi_c + \phi_s. \tag{4.3}$$

The compliant porosity consists of thin cracks and open spaces within grain contact boundaries, whereas the stiff porosity consists of the approximately spherical pores. Although

compliant porosity makes up only a small percentage of the overall pore space, its relative change with stress is far greater than the relative change in stiff porosity.

Shapiro (2003) uses the theory of poro-elasticity to derive an exponential relationship between compliant porosity and applied effective stress,

$$\phi_c = \phi_c^0 \exp(-\theta_c \sigma'/K^*), \tag{4.4}$$

where ϕ_c^0 is the compliant porosity at zero effective stress and K^* the bulk modulus of a rock assuming zero compliant porosity (i.e. a perfectly linear elastic rock with no cracks). The term θ_c represents a so-called elastic piezo-sensitivity coefficient

$$\theta_c = \frac{K_g(3K_g + 4\mu_g)}{\pi a \mu_g (3K_g + \mu_g)}, \tag{4.5}$$

where K_g and μ_g are the bulk and shear moduli of the grain material respectively, and a the effective aspect ratio of the compliant pore space. Based on these equations Shapiro (2003) expresses the velocity as a function of compliant porosity,

$$V_P(\sigma') \approx V_P^* - \frac{1}{2} V_P^* H_c \theta_{c\mu} \phi_c \tag{4.6}$$

and

$$V_S(\sigma') \approx V_S^* - \frac{1}{2} V_S^* \theta_{c\mu} \phi_c, \tag{4.7}$$

where V_P^* and V_S^* are the P- and S-wave velocity of the zero compliant porosity rock. The parameters $\theta_{c\mu}$ and H_c are defined as

$$\theta_{c\mu} \approx \frac{1}{5}\left[1 + \frac{4(3K_g + 4\mu_g)(9K_g + 4\mu_g)}{3\pi a (3K_g + \mu_g)(3K_g + 2\mu_g)}\right] \tag{4.8}$$

and

$$H_c = \frac{K^*\theta_c/\theta_{c\mu} + 4\mu^*/3}{K^* + 4\mu^*/3}, \tag{4.9}$$

where μ^* is the shear modulus of the zero compliant porosity rock. Note that again the linear K_ν term is left out of equations 4.6 and 4.7. Shapiro (2003) expresses this term as a function of the stiff porosity ϕ_s and makes the same observation as Zimmerman *et al.* (1986) in that it can be neglected in comparison to the two other, much larger terms. Shapiro (2003) also states that the exponential term in equation 4.4 is constant for both the P- and S-wave velocities and that equations 4.6 and 4.7 are valid for both dry and saturated rocks.

4.2.3 MST Model

Schoenberg & Sayers (1995) introduced an excess compliance approach to model the influence of cracks. The elastic compliance of a rock S_{ijkl} (the inverse of elasticity C_{ijkl}) can be thought of as being the sum of the intrinsic compliance of the rock matrix (in the absence of discontinuities) S^0_{ijkl}, plus the additional extrinsic compliance ΔS_{ijkl} due to the presence of cracks and grain contacts

$$S_{ijkl} = S^0_{ijkl} + \Delta S_{ijkl}. \tag{4.10}$$

The excess compliance due to cracks ΔS_{ijkl} can be expressed in terms of a second- and a fourth-rank crack density tensor α_{ij} and β_{ijkl}

$$\Delta S_{ijkl} = \frac{1}{4}(\delta_{ik}\alpha_{jl} + \delta_{il}\alpha_{jk} + \delta_{jk}\alpha_{il} + \delta_{il}\alpha_{ik}) + \beta_{ijkl}, \tag{4.11}$$

where δ_{ij} is the Kronecker delta. The second- and fourth-rank crack density tensors are defined

$$\alpha_{ij} = \frac{1}{V}\sum_m B^m_T n^m_i n^m_j S^m \tag{4.12}$$

and

$$\beta_{ijkl} = \frac{1}{V}\sum_m (B^m_N - B^m_T) n^m_i n^m_j n^m_k n^m_l S^m, \tag{4.13}$$

where V is volume and B^m_N and B^m_T the normal and tangential crack compliance across the mth displacement discontinuity having unit normal n_i and surface area S^m. Note that summation convention is used for equations 4.10-4.13.

Sayers & Kachanov (1995) state that as the ratio of normal to tangential crack compliance $B_N/B_T \to 1$ (i.e. as $B_N \to B_T$), the fourth-rank crack density tensor β_{ijkl} becomes at least an order of magnitude smaller than the second-rank crack density tensor α_{ij}. When $B_N/B_T = 1$, the so-called scalar crack assumption, $\beta_{ijkl} = 0$ and any crack set can be described by the three orthogonal components of the second-rank crack tensor α_{ij}. It has been shown that the scalar crack assumption is not universally valid for most real rocks (e.g. Angus *et al.*, 2009, 2012; Choi *et al.*, 2014). However, Hall *et al.* (2008) and Verdon *et al.* (2008) observe that the scalar crack assumption is still a valid approximation to predict the general characteristics of stress dependent velocity and anisotropy. They provide a set of equations that express the nine independent elastic constants of the orthorhombic

stiffness tensor C_{ij} in terms of the second-rank crack tensor α_{ij} and the compliance tensor of the background medium S^0_{ij} (i.e. rock mineral components),

$$\begin{aligned}
C_{11} &= [(S^0_{23})^2 - (S^0_{22} + \alpha_{22})(S^0_{33} + \alpha_{33})]/D \\
C_{22} &= [(S^0_{13})^2 - (S^0_{11} + \alpha_{11})(S^0_{33} + \alpha_{33})]/D \\
C_{33} &= [(S^0_{12})^2 - (S^0_{11} + \alpha_{11})(S^0_{22} + \alpha_{22})]/D \\
C_{12} &= [S^0_{12}(S^0_{33} + \alpha_{33}) - S^0_{13}S^0_{23}]/D \\
C_{13} &= [S^0_{13}(S^0_{22} + \alpha_{22}) - S^0_{12}S^0_{23}]/D \\
C_{23} &= [S^0_{23}(S^0_{11} + \alpha_{11}) - S^0_{12}S^0_{13}]/D \\
C_{44} &= [S^0_{44} + \alpha_{22} + \alpha_{33}]^{-1} \\
C_{55} &= [S^0_{55} + \alpha_{11} + \alpha_{33}]^{-1} \\
C_{66} &= [S^0_{66} + \alpha_{11} + \alpha_{22}]^{-1},
\end{aligned} \tag{4.14}$$

where

$$\begin{aligned}
D =&(S^0_{11} + \alpha_{11})(S^0_{23})^2 + (S^0_{22} + \alpha_{22})(S^0_{13})^2 + \\
&(S^0_{33} + \alpha_{33})(S^0_{12})^2 - 2S^0_{12}S^0_{13}S^0_{23} - \\
&(S^0_{11} + \alpha_{11})(S^0_{22} + \alpha_{22})(S^0_{33} + \alpha_{33}).
\end{aligned} \tag{4.15}$$

The P-wave speeds along the principle axes can be related to the diagonal elements of C_{ij} via

$$V_{11} = \sqrt{\frac{C_{11}}{\rho}}, \quad V_{22} = \sqrt{\frac{C_{22}}{\rho}}, \quad V_{33} = \sqrt{\frac{C_{33}}{\rho}}, \tag{4.16}$$

and S-waves propagating in the ith direction polarized in the jth by

$$V_{32} = V_{23} = \sqrt{\frac{C_{44}}{\rho}}, \quad V_{31} = V_{13} = \sqrt{\frac{C_{55}}{\rho}}, \quad V_{12} = V_{21} = \sqrt{\frac{C_{66}}{\rho}}. \tag{4.17}$$

The micro-structural formulation of Sayers (2002) and Hall *et al.* (2008) provides only a single second- and fourth-rank crack density value per stress measurement (i.e. no velocity-stress dependence). However, invoking the scalar crack assumption, Tod (2002) derives an analytical expression for the second-rank crack density, α_{ij} as a function of effective crack normal stress

$$\alpha_{ij} = \begin{cases} \frac{\epsilon_i(\sigma'(n_i))}{h_i}, & \text{if } i = j \\ 0, & \text{if} i \neq j \end{cases} \tag{4.18}$$

where

$$\epsilon_i\left(\sigma'(n_i)\right) = \epsilon^0 \exp\left[-\frac{2(1-\nu_b)}{\pi\mu_b a^0}\sigma'(n_i)\right]. \tag{4.19}$$

The terms a^0 and ϵ^0 are the initial aspect ratio and initial crack density at zero applied stress. The parameters ν_b and μ_b are the Poisson's ratio and shear modulus of the matrix assuming a zero compliant porosity rock. The normalisation term (Schubnel & Gueguen, 2003) h_i is given by

$$h_i = \frac{3E_i(2-\nu_i)}{32(1-\nu_i^2)}. \tag{4.20}$$

If we assume the rock is isotropic, the second-rank crack density tensor α_{ij} (equation 4.18) and the normalisation constant h_i (equation 4.20) can be simplified

$$\alpha_{11} = \alpha_{22} = \alpha_{33} \tag{4.21}$$

and

$$h_1 = h_2 = h_3. \tag{4.22}$$

It should be noted that there is often criticism of rock physics models such as the FPR and MST models based on their model idealisations of the rock architecture. It is important to stress that ultrasonic seismic signals are band-limited (i.e. finite frequency bandwidth) and so carry limited information such as travel-time, amplitude and phase. For wave propagation scenarios, such as ultrasonic measurements, the seismic wavefield experiences the averaging effects of sub-wavelength scale features in the rock. Thus, the information that the seismic wavefield provides is not at all comparable to actual rock architecture. However, rock physics models such as the FPR and MST models allow us to construct intuitive model idealisations that have some correlation to measurable parameters.

4.2.4 TOE Model

Third order elasticity rock physics models present a non-linear elastic stiffness tensor as a function of stress and strain by invoking elasticity theory (e.g. Thurston & Brugger, 1964). They include cubic (or third-rank) terms that account for a non-linear change in stiffness with stress. Third order elastic constants can have different relationships with rock parameters (e.g. Fuck & Tsvankin., 2009; Shapiro, 2005; Sinha & Plona, 2001). However, this study focuses primarily on the commonly used TOE models of Prioul *et al.* (2004) and Korneev & Glubokovskikh (2013).

TOE-1 Prioul

Prioul *et al.* (2004) derived nine independent components of an orthorhombic stiffness tensor C_{ij} as

$$\begin{aligned}
C_{11} &= C_{11}^{\text{ref}} + c_{111}\Delta\varepsilon_{11} + c_{112}(\Delta\varepsilon_{22} + \Delta\varepsilon_{33}) \\
C_{22} &= C_{11}^{\text{ref}} + c_{111}\Delta\varepsilon_{22} + c_{112}(\Delta\varepsilon_{11} + \Delta\varepsilon_{33}) \\
C_{33} &= C_{33}^{\text{ref}} + c_{111}\Delta\varepsilon_{33} + c_{112}(\Delta\varepsilon_{11} + \Delta\varepsilon_{33}) \\
C_{12} &= C_{12}^{\text{ref}} + c_{112}(\Delta\varepsilon_{11} + \Delta\varepsilon_{22}) + C_{123}\Delta\varepsilon_{33} \\
C_{13} &= C_{13}^{\text{ref}} + c_{112}(\Delta\varepsilon_{11} + \Delta\varepsilon_{33}) + C_{123}\Delta\varepsilon_{22} \\
C_{23} &= C_{13}^{\text{ref}} + c_{112}(\Delta\varepsilon_{22} + \Delta\varepsilon_{33}) + C_{123}\Delta\varepsilon_{11} \\
C_{44} &= C_{44}^{\text{ref}} + c_{144}\Delta\varepsilon_{11} + c_{155}(\Delta\varepsilon_{22} + \Delta\varepsilon_{33}) \\
C_{55} &= C_{44}^{\text{ref}} + c_{144}\Delta\varepsilon_{22} + c_{155}(\Delta\varepsilon_{11} + \Delta\varepsilon_{33}) \\
C_{66} &= C_{66}^{\text{ref}} + c_{144}\Delta\varepsilon_{33} + c_{155}(\Delta\varepsilon_{11} + \Delta\varepsilon_{22}),
\end{aligned} \tag{4.23}$$

where rock stiffness is expressed as a function of the second-rank elastic constants of the rock in a fixed reference state C_{ij}^{ref}. $\Delta\varepsilon_{ij}$ is the change in strain as a result of deviations from the reference state and c_{ijk} are third-rank (non-linear) elastic coefficients that define the linear relationship (or gradient) between stiffness and strain. Assuming the third-rank tensor is isotropic, only three independent non-linear coefficients are needed: c_{111}, c_{112} and c_{123}. The remaining two coefficients are given by

$$c_{144} = \frac{(c_{112} - c_{123})}{2}, \quad \text{and} \quad c_{155} = \frac{(c_{111} - c_{112})}{4}. \tag{4.24}$$

Equation 4.23 can be simplified further if we assume hydrostatic strain

$$\Delta\varepsilon_{11} = \Delta\varepsilon_{22} = \Delta\varepsilon_{33}. \tag{4.25}$$

Application of these equations requires strain data, which is often not measured during ultrasonic velocity-stress experiments (e.g. none of the datasets compiled in Angus *et al.*, 2009, 2012, provide strain data). However, Lei *et al.* (2012) provides an approximation of strain by assuming a hydrostatic stress state and a linear relationship between incremental changes in stress $\Delta\sigma'$ and strain $\Delta\varepsilon$,

$$\Delta\varepsilon = \frac{2C_{44}^{\text{ref}}\Delta\sigma'}{2C_{44}^{\text{ref}}(3C_{11}^{ref} - 4C_{44}^{\text{ref}})}. \tag{4.26}$$

Similar to the micro-structural formulation of Sayers (2002) and Hall *et al.* (2008) (equation 4.14), this third-order elasticity model has limited predictive capabilities. Specifically, this particular model is a local linear approximation of a non-linear relationship. However, Prioul *et al.* (2004) separated the data into several linear stress regimes to provide an approximate yet predictive algorithm.

TOE-2 Korneev & Glubokovskikh

Korneev & Glubokovskikh (2013) used nonlinear elasticity theory to derive a set of equations that describe the P- and S-wave velocities of a transversely isotropic medium,

$$V_{11}^2 = V_{22}^2 = V_{0_{11}}^2 + \frac{2q(B+C)}{\rho}, \tag{4.27}$$

$$V_{33}^2 = V_{0_{33}}^2 + \frac{2q(A+3B+C)}{\rho}, \tag{4.28}$$

$$V_{13}^2 = V_{31}^2 = V_{23}^2 = V_{32}^2 = V_{0_{13}}^2 + \frac{q(B+\frac{A}{2})}{\rho}, \tag{4.29}$$

$$V_{12}^2 = V_{21}^2 = V_{0_{12}}^2 + \frac{qB}{\rho}. \tag{4.30}$$

where A, B and C are TOE constants, ρ is density and $V_{0_{ij}}$ the seismic velocity of the unstressed rock. The parameter q defines a nonlinear static-strain component,

$$q = -\frac{\lambda+2\mu}{4(A+3B+C)}\left[1-\sqrt{1-\frac{8(A+3B+C)\sigma'}{(\lambda+2\mu)^2}}\right], \tag{4.31}$$

where λ and μ are the Lamé parameters of the unstressed rock and σ' the effective stress. Korneev & Glubokovskikh (2013) evaluated their analytical formulae using sonic log data and stacking velocities. The results of which showed relatively good fit to the observed data. However, they did not apply their formulae to laboratory measured ultrasonic velocity versus stress measurements.

Lithology	Reference
Sandstone	Han *et al.* (1986). Jizba (1991). He (2006). King (1966, 2002). Rojas (2005). Hemsing (2007). Grochau & Gurevich (2008).
Tight sandstone	Al-Harasi *et al.* (2013).
Limestone	Nur & Simmons (1969). Brown (2002). Simmons & Brace (1965).
Dolostone	Nur & Simmons (1969). Brown (2002).
Conglomerate	He (2006).
Anhydrite	Hemsing (2007).
Shale	Hemsing (2007). Hornby (1998). Johnston & Christensen (1995). Lorinczi *et al.* (2014).
Granite	Nur & Simmons (1969).
Carbonate	Hemsing (2007).

Table 4.1: Published ultrasonic velocity-stress core data.

Model	Unkown model parameters
Empirical (EMP): P- and S-wave	A_ν, B_ν, D_ν
First Principle Model (FPR)	V_P^{gr}, V_S^{gr}, ϕ_c^0, a
Micro-structural Model (MST)	V_P^{gr}, V_S^{gr}, a^0, ϵ^0
Third Order Elasticity - 1 (TOE-1)	c_{111}, c_{112}, c_{123}
Third Order Elasticity - 2 (TOE-2)	A, B, C, V_{P0}, V_{S0}

Table 4.2: Unknown rock physics model parameters found via inversion of the ultrasonic velocity-stress core data.

4.3 Core Data

The ultrasonic velocity versus stress measurements used in this study were compiled by Angus *et al.* (2009). However, I augment this dataset to include sandstone core data complimentary from the Wolfson multiphase flow laboratory of the University of Leeds along with other tight sandstone (Al-Harasi *et al.*, 2013) and shale (Lorinczi *et al.*, 2014) samples. The complete dataset is summarised in Table 4.1 and contains a total of over 400 samples. As the majority of published datasets only include a single P- and S-wave velocity measurement along a single direction (i.e. vertical axis of the cylindrical core sample), I use only the vertical velocity measurements of the few multi-directional datasets. If multi-directional data are available, anisotropic rock behaviour and hence anisotropic non-linear model parameters could be considered (e.g. Verdon *et al.*, 2008). However, due to a lack of anisotropic data within this particular dataset, I focus on the isotropic scenario.

4.4 Inversion Methodology

Some of the rock physics models defined in the previous section require some form of information regarding the mineral composition of the sample rock (e.g. K_g and μ_g for the FPR model), or so-called zero compliant porosity elasticity (e.g. V^* for the FPR model, and S^0_{ijkl}, ν_b and μ_b for the MST model). Typically, these are determined using either quantitative X-ray diffraction methods (e.g. Kendall *et al.*, 2007) or estimated from the behaviour of the rock sample at high confining stress (e.g. Sayers, 2002). However, obtaining mineral composition data is not trivial. The utility of using mineral data itself to estimate non-compliant elasticity neglects the importance of cementation and grain packing. This leads to potentially inconsistent or inaccurate velocity estimates. Also, laboratory ultrasonic velocity experiments typically try to minimise plastic deformation and so avoid high effective stresses. This means that the sample likely never reaches the state where all discontinuities are fully closed i.e. zero compliant porosity. As such, in this study I express each of these parameters in terms of the P- and S-wave velocity of a hypothetical rock with zero compliant porosity and include them in the inversion process.

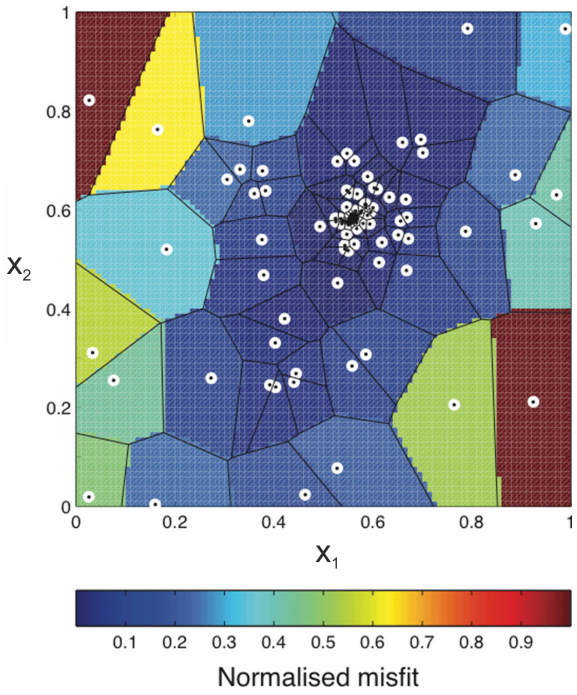

Figure 4.1: An example of exploring a two-parameter space using the Neighbourhood Algorithm (NA) of Sambridge (1999a). White circles show where the objective function has been sampled. The value of the function at each location is assumed to approximate the value of its neighbourhood (i.e. Voronoi cell in which it is located) shown by the colour scale. Promising neighbourhoods are re-sampled and the algorithm converges to the global minima. This image has been taken and modified from Wookey (2012).

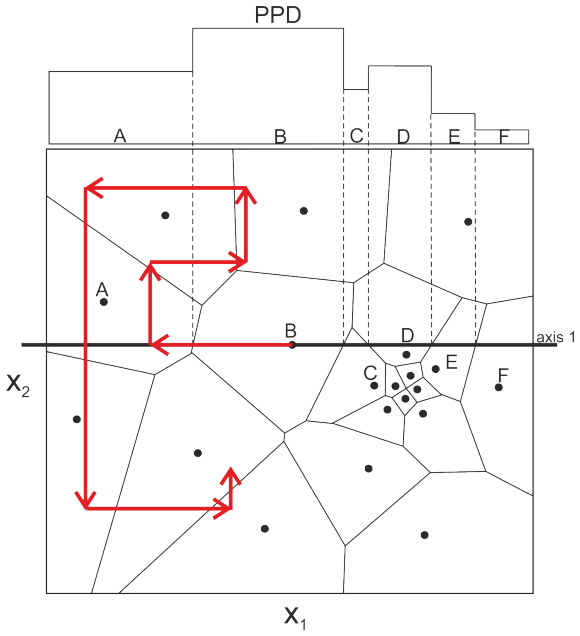

Figure 4.2: Four iterations of a random walk for the NA Bayesian algorithm starting from point B. Each walk takes a series of steps along each parameter axis in turn. It is possible for the random walk to move into any of the voronoi cells along a given axis, with the probability determined by the product of the PPD value and the width of the voronoi cell intersection with that axis. This image was taken and re-drawn from Sambridge (1999b).

The velocity of a rock with zero compliant porosity is assumed to be suitable similar to that of the grain material V_P^{gr}, V_S^{gr}. Theoretically, the two velocities are different in that the velocity of a zero compliant rock is also affected by the incompliant porosity and grain packing. However, for the purpose of this study, the difference is assumed negligible and I refer to both velocities as V_P^{gr}, V_S^{gr}. A valid assumption, supported by equation 9 of Shapiro (2003), which is based on the observation that for very high stresses the stiff porosity will obey an exponentially decreasing behaviour. To constrain the inversion, it is assumed that these grain velocities (i.e. where $\partial V/\partial\sigma' = 0$) are within ± 300 m/s of the highest recorded stress velocity.

For the TOE-1 model, I follow the approach of Prioul *et al.* (2004) and separate the data into low ($\sigma' \leq 20$ MPa), middle ($20 > \sigma' \leq 60$ MPa) and high ($\sigma' > 60$ MPa) stress regimes and invert for the third-rank coefficients of each regime separately. Since a reference rock state is needed (C_{ij}^{ref} in equation 4.23), *a priori* knowledge of the second-rank elastic constants of the rock at each stress interval is required. For this case, I assume this to be the data point whose stress value is closest to the lower bound of each interval (i.e. 0MPa, 20MPa and 60MPa). As no strain data is available, the approximation of Lei *et al.* (2012) is used (equation 4.26). Furthermore, only vertically propagating P- and S-waves are considered, hence only equations 4.28 and 4.29 from the TOE-2 model of

Korneev & Glubokovskikh (2013) are used. I also jointly invert for the P- and S-wave velocities at zero confining stress ($V_{0_{33}}$ and $V_{0_{13}}$) due to the lack of zero stress velocity measurements. Table 4.2 provides an overview of all unknown parameters for each of the five models.

For the inversion scheme, relatively large (but theoretically acceptable) parameter ranges are set for the initial inversion. This is because (1) the literature contains sparse information regarding definitive model parameter ranges and (2) this study focuses on model robustness and the constraint of the model inversion. Since some of the parameter ranges span large orders of magnitude, I use the neighbourhood algorithm (NA) of Sambridge (1999a) as the inversion procedure. The NA discretises the parameter space using Voronoi cells and iteratively explores the cells (or '*neighbourhoods*') that appear the most promising (see Figure 4.1). This results in a model ensemble that has sparse coverage over a broad range of the parameter space, whilst much finer i.e. localized, coverage near minima in the misfit function. This makes it an ideal algorithm to use for potentially very sharp global minima in a misfit function that may span many orders of magnitude. The objective function is defined as the model misfit between either both the P- and S-wave data or separately for each wave. The parameters for the NA global search are kept constant for all samples and models such that the inversion results can be compared directly.

For each sample, once an appropriate model solution has been found, the search ensemble is evaluated using the method of Sambridge (1999b). This algorithm was developed as a compliment to the NA sample and implements a Bayesian integration of the NA ensemble. It calculates 1-D and 2-D probability density functions (PDFs), to explore the confidence in any given coefficient or trade-off between different parameters. The NA Bayesian integration works by iteratively generating a number of random walks within the tessellated model space, whose distribution asymptotically tends towards a given Posterior Probability Distribution (PPD). Each walk takes a series of steps along each parameter axis in turn. It is possible for the random walk to move into any of the Voronoi cells along a given axis, with the probability determined by the product of the PPD value and the width of the Voronoi cell intersection with that axis. A random walk is demonstrated in Figure 4.2. Note that this method uses a neighbourhood approximation of the PPD where the probability is spread uniformly across each Voronoi cell as opposed to concentrated at a single point.

4.5 Results

Here I present the inversion results of each rock physics model and analyse their fit to the observed data. I also compare each model's time-lapse velocity predictions when subject to

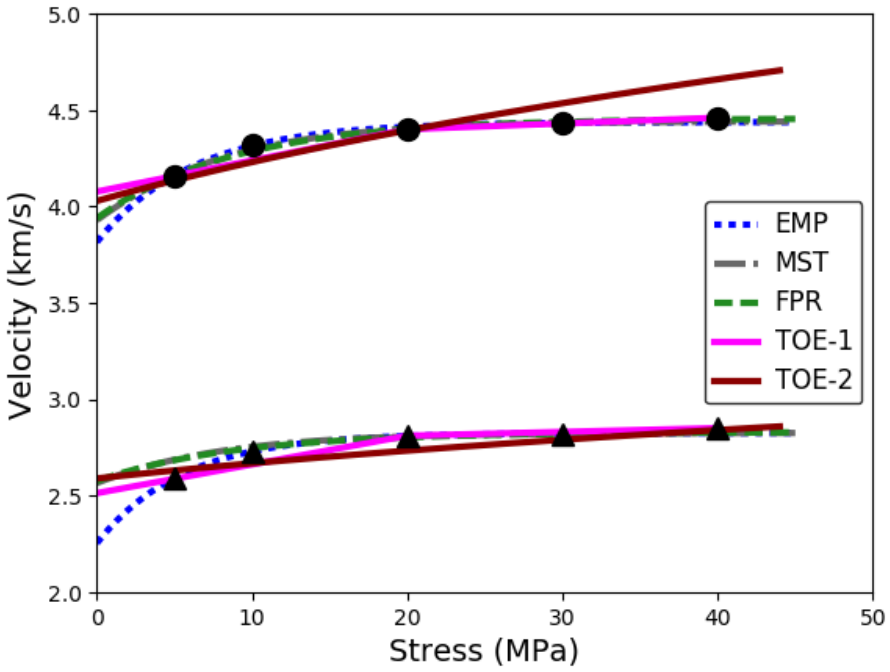

Figure 4.3: Rock physics model velocity-stress predictions for a representative sandstone core sample. Ultrasonic P-wave data shown by black circles and S-wave data by black triangles.

the production scenario of Chapter 2. The constraint of each model inversion is analysed and a collection of 1-D and 2-D PDF's of different model parameters presented. I also derive simple relationships between model parameters and key rock properties. These results are then used to discuss the potential calibration of certain models to predict suitably accurate time-lapse changes in seismic velocity when laboratory measurements are unavailable. Finally, I conclude by discussing the implications of core damage to the sensitivity of the stress-velocity relationship.

4.5.1 Initial Inversion Results

Figure 4.3 shows the inversion results for a single sandstone core sample and is a good representation of the whole dataset. Specifically, the results across each model show successful optimisation and a suitably good fit to the observed data. The inversion results for all samples are shown in the histograms of Figure 4.4. Care must be taken when interpreting these results as the dataset contains an unequal distribution of core samples of differing rock lithology. Therefore it should primarily be used to assess the range of values found for each parameter across our dataset. It should be noted that due to the limited number of high stress measurements, there are fewer values for the TOE-1 model high stress regime (i.e. mainly the hard rock samples have measurements above 60MPa).

If you examine each models fit to the observed data in more detail it is apparent that the TOE-2 model provides a relatively poor fit to observed P-wave velocity data at high effective stresses. Also, there is a slight degradation in most of the MST and FPR S-wave velocity predictions at low effective stress. By looking at the histograms of the EMP model (e.g. Figure 4.4), the distributions for the parameters A_ν, B_ν and D_ν differ when used to fit either P- of S-wave data. For the parameter A_ν, a shift in the distribution from P to S is to be expected as the S-wave speed at high stress (i.e. $\sigma \to \infty$) will be lower than the corresponding P-wave speed. However, differing distributions of B_ν and D_ν suggests that many samples have a different P- and S-wave velocity stress dependence (i.e. differing curvatures of the velocity-stress relationship). As such, this indicates that the V_P/V_S ratio, and hence Poisson's ratio, is stress dependent. By comparing the V_P/V_S ratio of the data compared to that predicted by the models it can be seen that the FPR, MST and TOE-2 models struggle to fit the observed stress dependent V_P/V_S ratio (e.g. Figure 4.5). These models appear to be formulated to predict an increase in V_P/V_S ratio

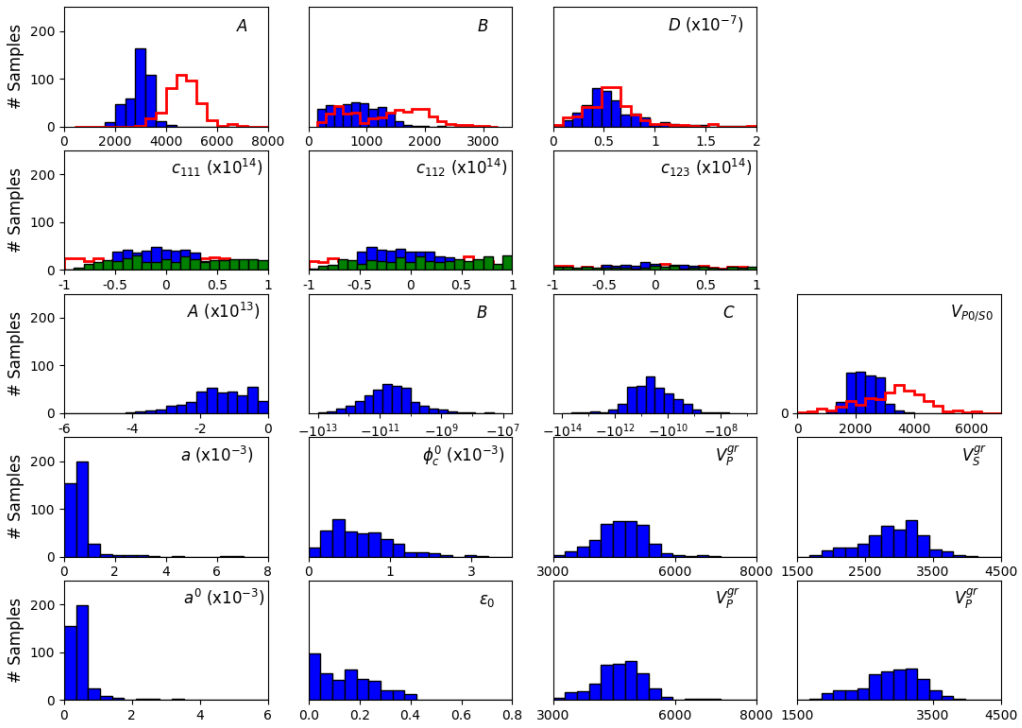

Figure 4.4: Histograms showing the range of inverted model parameters for all rock physics models: [top row] EMP model parameters, P-wave (red line) and S-wave (blue bar); [second row] TOE-1 model, low stress regime (red line), middle stress regime (green bar) and high stress regime (blue bar); [third row] TOE-2, with V_{S0} displayed as a bar plot whilst V_{P0} a red line; [fourth row] FPR model and [bottom row] MST model. Note that all velocities are given in ms^{-1} and third order coefficient in Pascals.

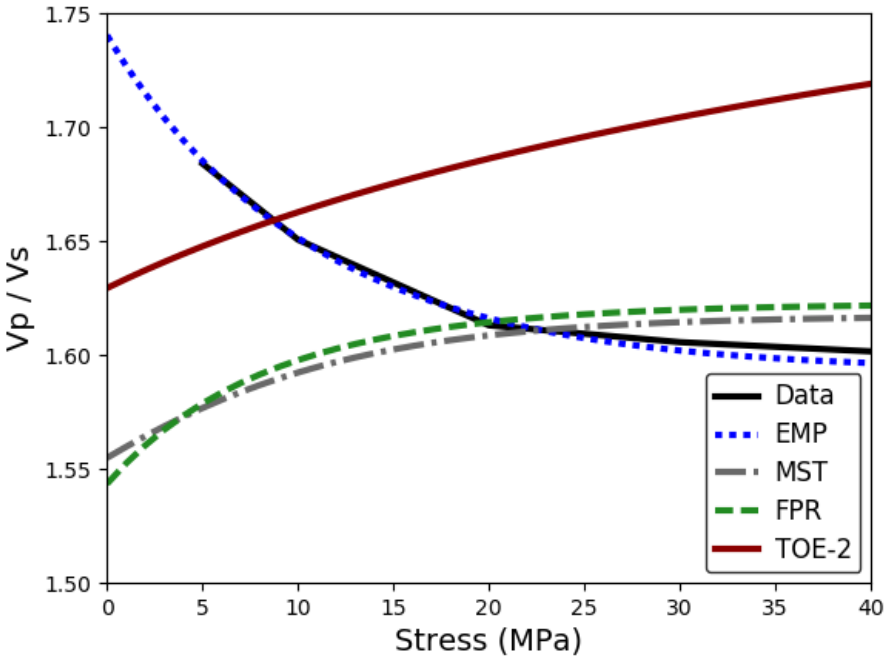

Figure 4.5: V_P/V_s ratio of the velocity-stress data for the representative sandstone sample of Figure 4.3 along with the corresponding ratios derived from the velocity-stress predictions of each rock physics model.

with increasing stress (i.e. increase in Poisson's ratio). However, the V_P/V_S ratio of the majority of the samples in the dataset is observed to decrease with increasing stress. By defining model parameters separately for each wave type, the EMP model is more successful in modelling the stress dependent V_P/V_S ratio. If this approach is applied to the FPR, MST and TOE-2 models in which the inversion for model parameters uses only a single set of velocity measurements (in this case we choose the P-wave measurements and assume V_S^{gr} is known *a priori*), a clear improvement is observed in the data fit for a majority of samples (e.g. Figure 4.6).

Although the results of Figure 4.6 show that it is possible to improve the fit of the TOE-2 model by using only a single set of velocity measurements, the absolute value of the Root Mean Square Error (RMSE) for the majority of samples is still much larger than those seen for other models. This is due to the fact that the TOE-2 expressions 4.28 and 4.29 attempt to model data that display a sharp exponential trend using functions that lack an exponential term. A similar issue is apparent in the TOE-1 model results where the local linear approximation struggles to accurately model the non-linear data. This is especially the case at low effective stresses where the non-linear relationship is at its strongest. Therefore, these models show a relatively poorer fit to the observed data and thus a greater RMSE.

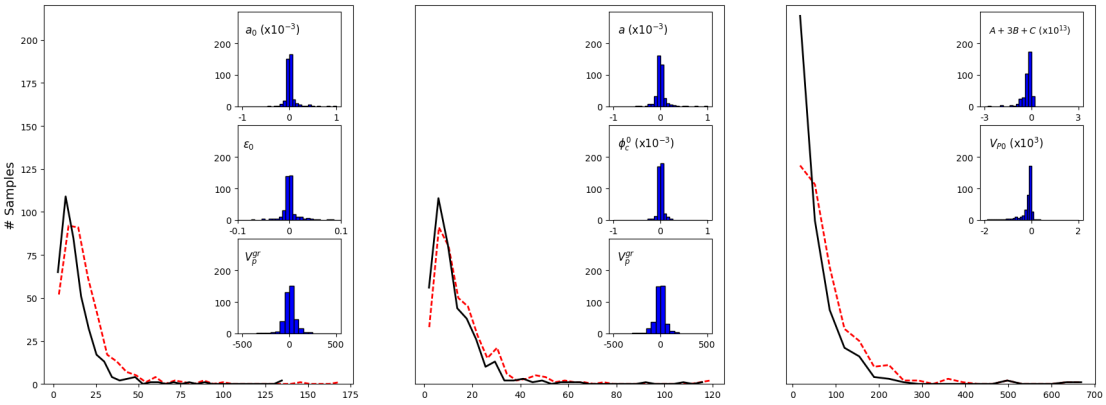

Figure 4.6: Histograms showing the range of Root Mean Square Errors (RMSE's) between the P-wave data and the rock physics model for all core samples. Dashed red line represents those models derived from inverting both P- and S-waved data, whilst the solid black line those derived from the P-wave data alone. Left is the MST, middle the FPR and right the TOE-2 model. The inset histograms show the absolute differences in the unknown parameters between each inversion. Note all velocities are given in ms^{-1} and the third order coefficients in Pascals.

4.5.2 Model Parameter Constraints

To assess how well constrained each model inversion is, the ensemble generated by the NA sampler is evaluated using the method of Sambridge (1999b) (see Figure 4.2). It should be noted that for all models presented in this work I assume no *a priori* constraint on the unknown parameters and thus uniform prior probability density.

Figure 4.7 show the 1-D and 2-D PDFs of the P-wave EMP and TOE-1 model of the representative sandstone sample shown in Figure 4.3. Narrow parameter PDFs for the EMP model highlight a relatively well constrained inversion where only a small subset of the model space can explain the velocity-stress dependence. Whereas, wide TOE-1 parameter PDFs that span the entire model space highlight a relatively poorly constrained inversion. This is a result of an under-determined inverse problem with no unique solution. A lack of multi-directional velocity data and strain measurements leads to a number of equally well fitted solutions. This is also indicated in the histograms of Figure 4.4 where the results of the TOE-1 inversion do not display any global trends. Instead they are uniformly spread across the entire model space.

The MST and FPR model show similar results to that of the EMP model, where a well defined global minimum exists in the model space making for a well constrained inversion. Similarly a well constrained inversion is seen for the TOE-2 model if we consider only the P-wave velocity data and the three third order coefficients as a combined unknown function $A+3B+C$ (Figure 4.8). However, determining a unique value for each individual third order coefficient i.e. A, B and C, is not possible when considering only a single set

of P- and S-wave velocity data. This is shown in the 2-D marginals of Figure 4.8 where a suitably well constrained value of the coefficient A is found but numerous solutions exist for the remaining coefficients B and C which span large orders of magnitude (also seen in the histograms of Figure 4.4). Therefore, similar to the TOE-1 model, a lack of multi-directional velocity data leads to an under-determined problem with a number of equally well fitted solutions. Although the results presented in Figures 4.7 and 4.8 are for a single core sample they are a good representation of the entire dataset. In general, relatively well constrained EMP, FPR and MST model inversions are observed whilst poorly constrained TOE-1 and TOE-2 inversions.

4.5.3 Comparison of 4-D Velocity Predictive Capabilities

For a typical hydrocarbon monitoring scenario, rock physics models are used as a method of modelling the influence of production related stress changes on seismic (i.e. P-wave) velocities. Consider the behaviour of the overburden chalks in the hydromechanical model

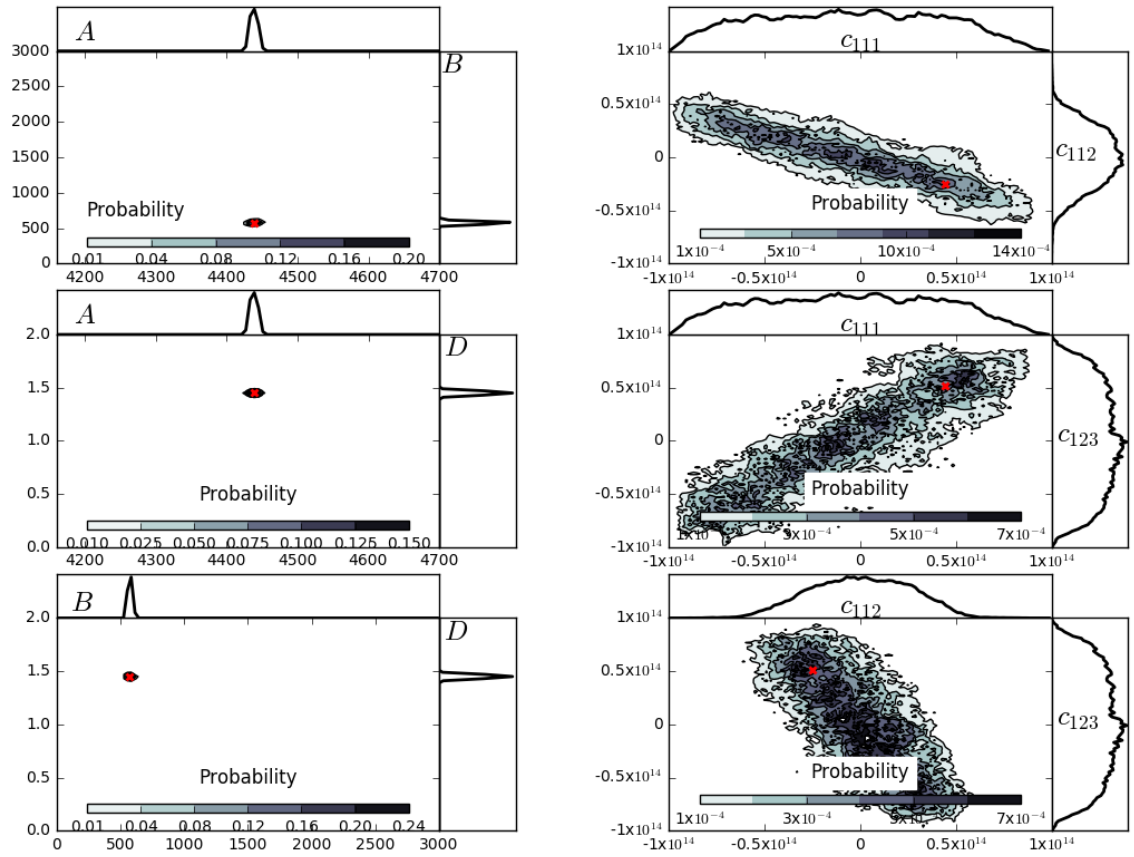

Figure 4.7: 1-D and 2-D Probability Density Functions (PDFs) for parameters A_P, B_P and D_P of the P-wave EMP model (left) and parameters c_{111}, c_{112} and c_{123} of the TOE-1 model (right) for the representative sandstone sample of Figure 4.3. The red cross indicates the final inversion result used to plot the models displayed in Figure 4.3.

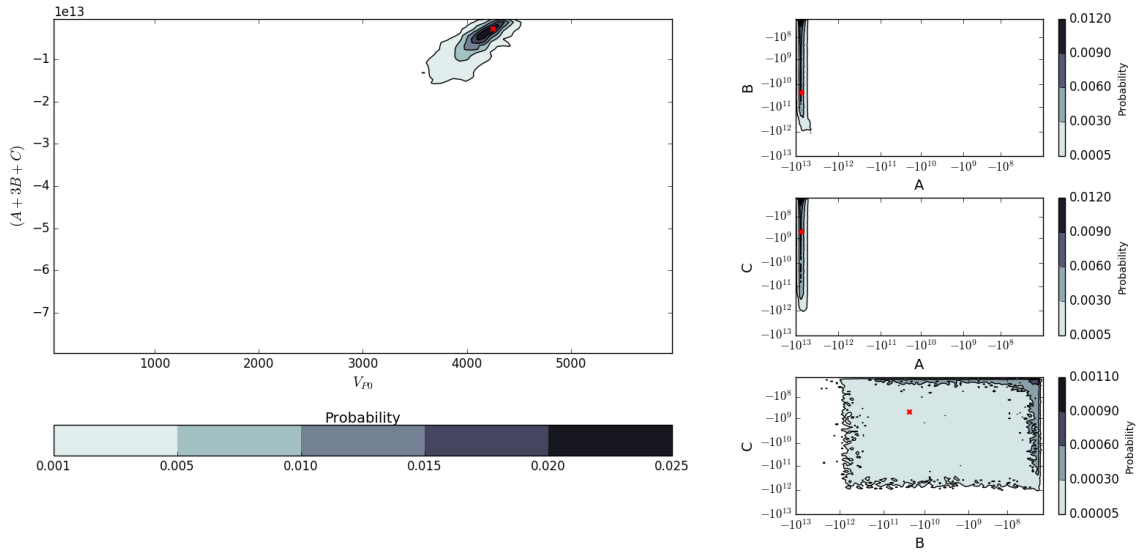

Figure 4.8: Left, the 2-D PDF of the two unknown parameters, V_{P0} and $A + 3B + C$, of the P-wave only TOE-2 inversion. Right, the 2-D PDF's when attempting to invert for each third order coefficient, A, B and C independently using both P- and S-wave data. Note that again these PDF's were created based on the results of the representative sandstone of Figure 4.3 with the red cross indicating the final inversion result.

of Chapter 2. In particular, layer 5 (see Table 2.1), the same chalk layer analysed in the GSA of Chapter 3. Directly above the reservoir (i.e. at the production well location in Figure 2.1), this layer experiences roughly a 5MPa (i.e. from 35 to 30MPa) reduction in vertical effective stress (e.g. Figures 2.10 and 2.13) after 20 years of production. Assuming that each core sample in our dataset is a potential representation of the velocity-stress dependence of this layer, it is possible to compare the velocity change predicted by each rock physics model. As it is the relative difference between models that is of interest, as opposed to absolute time-lapse predictions, the discrepancy between the layers lithology and that of the core sample become less important. Figure 4.9 show crossplots of the predicted P-wave velocity results of each model from all samples in our dataset against those predicted by the EMP model. The results of the EMP model are used as a reference here due to it having the lowest RMSE for most core samples. Also it should be noted that due to degradation in certain model solutions when considering S-wave data (e.g. Figure 4.6), I take the inversion results for the P-wave only FPR, MST and TOE-2 models.

The results show that, in addition to all models having a suitably good fit to the observed data, the FPR, MST and EMP model predict similar changes in seismic velocity with stress. However, it is important to note that slight discrepancies between models do exist. Marked on Figure 4.9 is a +/- 0.2% region. It is clear that for certain samples these different models do predict up to 0.2% difference in velocity change. As we are concerned with relatively small percentage changes (e.g. Figure 2.16) these slight discrepancies be-

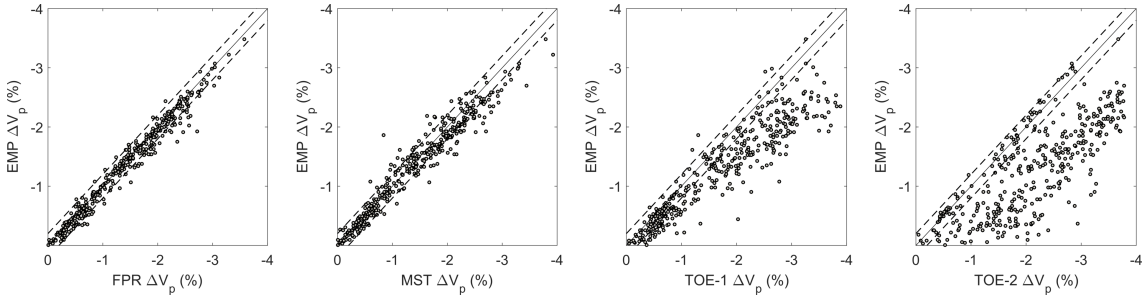

Figure 4.9: Crossplots of the percentage velocity change associated with 5MPa reduction in effective stress (i.e. 35 to 30MPa) predicted by each of the rock physics models for each core sample. A reduction in effective stress seen in the overburden chalk layer (Layer 5 in Table 2.1) at the production well location (e.g. Figure 2.1). The results of the EMP model are used as a reference due to it having the lowest RMSE for most core samples. Due to degradation of the FPR, MST and TOE-2 model solutions when the S-wave data is considered, these results are based on the P-wave only inversion results. The dotted lines represent a +/- 0.2% velocity change region.

tween models become significant. The TOE-1 and TOE-2 models however, appear to overestimate the velocity change for almost all samples. This is due to their poorer fit to the observed data seen across all samples (Figures 4.3 and 4.6). Overestimates are caused by these models attempting to fit data that display an exponential trend using functions that lack an exponential term. The poorer fit is emphasised when comparing relatively sensitive measures of velocity change.

4.5.4 Estimating Model Parameters using Proxy Rock Properties

Velocity-stress core data is not always readily available. This is often the case for non-reservoir rocks in hydrocarbon scenarios where core samples are not typically taken. Therefore, using core data to invert for a best fitting rock physics model is not always possible. This becomes an issue with models such as the EMP and TOE-1/2 as their coefficients lack physical meaning and thus theoretically cannot be derived without inverting velocity-stress data. On the other hand, the FPR and MST models are parameterised in terms of rock physical properties and thus theoretically can be derived from analysing rock architecture. However, determining properties, such as aspect ratio and crack density, is not trivial and often requires core samples to carry out complex laboratory techniques such as X-ray diffraction.

Eberhart-Phillips *et al.* (1989) set out to rectify this issue by relating the parameters of the EMP model (equation 4.1) to more abundant and easily measurable rock properties. Using a dataset of 64 sandstone core samples, Eberhart-Phillips *et al.* (1989) evaluated the best fitting numerical values for the parameters K, B and D whilst deriving the coefficient A as a function of porosity ϕ and clay content C,

$$V_p = 5.77 - 6.94\phi - 1.73\sqrt{C} + 0.446(\sigma' - exp(-16.7\sigma')), \tag{4.32}$$

and

$$V_s = 3.70 - 4.94\phi - 1.57\sqrt{C} + 0.361(\sigma' - exp(-16.7\sigma')). \tag{4.33}$$

Note that in equations 4.32 and 4.33 the P- and S-wave velocities are given in km/s and the effective stress σ' in $kbars$. Eberhart-Phillips *et al.* (1989) found that these simple approximations give relatively good velocity predictions for their dataset and deduced they may be useful for estimating the velocity of sandstone rocks for which laboratory measurements are unavailable. However, by replacing the parameters B, D and K with best fitting constants, a constant shape/curvature of the nonlinear relationship must be assumed. Therefore these simple functions may be useful for predicting the absolute magnitude of the rock velocity but may be limited when it comes to describing its nonlinear relationship with stress.

This is demonstrated in Figure 4.10, where, for each sandstone sample in the dataset, the absolute P-wave velocity and it's percentage change associated with the same production scenario as used for Figure 4.9, predicted by equation 4.32 are crossplotted against

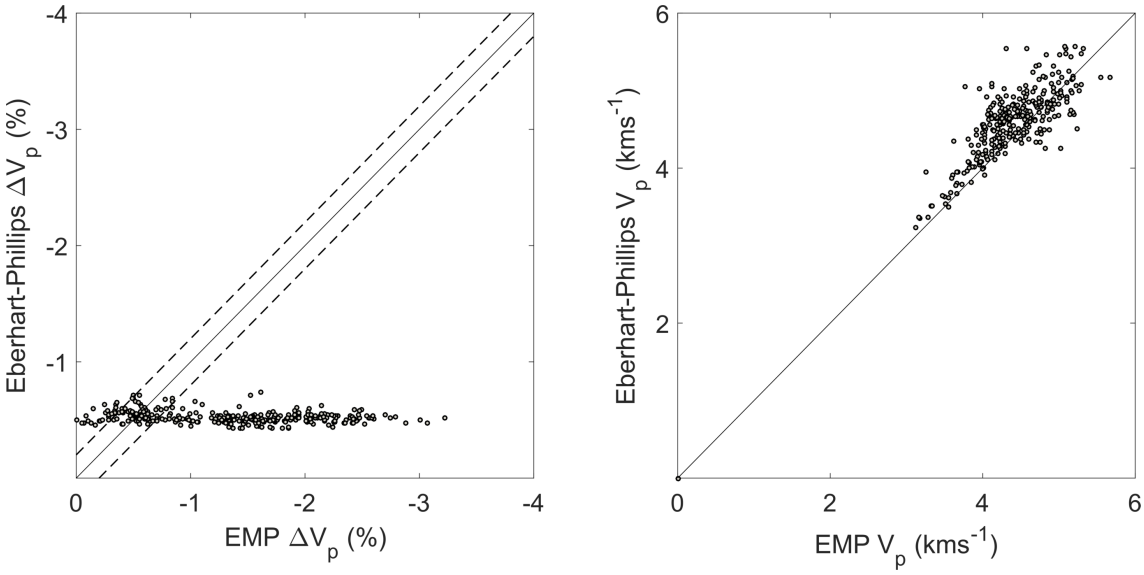

Figure 4.10: Crossplots showing the absolute P-wave velocity associated with 35MPa of effective stress for each sandstone core sample predicted by equation 4.32 against those of the EMP model (right). Also crossplotted is the percentage velocity change associated with a 5MPa reduction in effective stress (i.e. 35 to 30MPa) for each sandstone sample predicted by the two models (left). This represents the same overburden scenario as that of Figure 4.9. The dotted lines represent a +/- 0.2% velocity change region.

$f(\phi, C) = X_0 + X_1\phi + X_2 C$					
Model	Parameter	Coefficient			R^2
		X_0	X_1	X_2	
EMP	$A_{p/s}$	5594 / 3725	-7650 / -5842	-1143 / -1196	0.749 / 0.721
	$B_{p/s}$	1923 / 1114	-2393 / -410.2	-2070 / -1382	0.152 / 0.173
	$D_{p/s}$	5.370 / 3.581x10^{-8}	1.082 / 2.154 x10^{-7}	-3.853 / -9.537 x10^{-8}	0.056 /0.281
FPR	V_P^{gr}	5612	-7681	-1057	0.760
	V_S^{gr}	3670	-6038	-1085	0.716
	ϕ_c^0	6.212x10^{-4}	1.787x10^{-4}	9.426x10^{-6}	9. 193x10^{-4}
	a	2.560x10^{-4}	1.175x10^{-4}	1.478x10^{-4}	0.278
MST	V_P^{gr}	5570	-7594	-1044	0.751
	V_S^{gr}	3670	-6038	-1085	0.716
	a^0	1.731x10^{-4}	9.688x10^{-4}	1.258x10^{-3}	0.318
	ϵ^0	2.138x10^{-1}	-1.331x10^{-1}	-2.583x10^{-1}	0.069
TOE-2	V_{P0}	3499	-5131	1078	0.126
	$(A + 3B + C)$	-2.259x10^{13}	3.371x10^{13}	2.451x10^{13}	0.130

Table 4.3: Table showing the coefficients of the linear regression surface for each rock physics model parameter as a function of porosity ϕ and clay content C. The corresponding R^2 value for each surface is also included to indicate the goodness of fit. Note that all velocities, i.e. V_P^{gr} etc., are given in ms^{-1} and third order coefficients i.e. $(A + 3B + C)$, in Pascals.

those predicted by the original EMP model (equation 4.2). The relatively consistent estimated velocity change across all samples predicted by equation 4.32 ($\approx 0.5\%$) is an issue for time-lapse seismic monitoring. Estimating accurate time-lapse changes is arguably more important than a good approximation of absolute rock velocity in these scenarios. It should be noted that not all sandstone core samples within this dataset contained information regarding clay content. Therefore this analysis is limited to those sandstone samples in which clay content is available ($\approx$300).

I mimic the procedure taken by Eberhart-Phillips *et al.* (1989) and aim to relate rock physics model parameters to more abundant rock properties. These properties again being porosity and clay content. However, instead of approximating certain parameters with best fitting numerical constants, I aim to relate all unknown parameters to porosity and clay content in an attempt to improve predicted velocity changes. The analysis is focused purely on sandstone samples as they form the majority of the dataset for which clay content and porosity values are available. It is well understood that seismic velocity is a complex function of many rock properties and that it cannot be completely described by porosity and clay content alone (as expressed by Eberhart-Phillips *et al.* (1989)). However, the aim is to create simple relationships that could provide useful time-lapse approximations to within a workable accuracy. Linear least squares regression surfaces are calculated for each parameter-porosity-clay relationship. The coefficients of each linear model surface, along with its corresponding goodness of fit as an R-squared value, is provided in Table

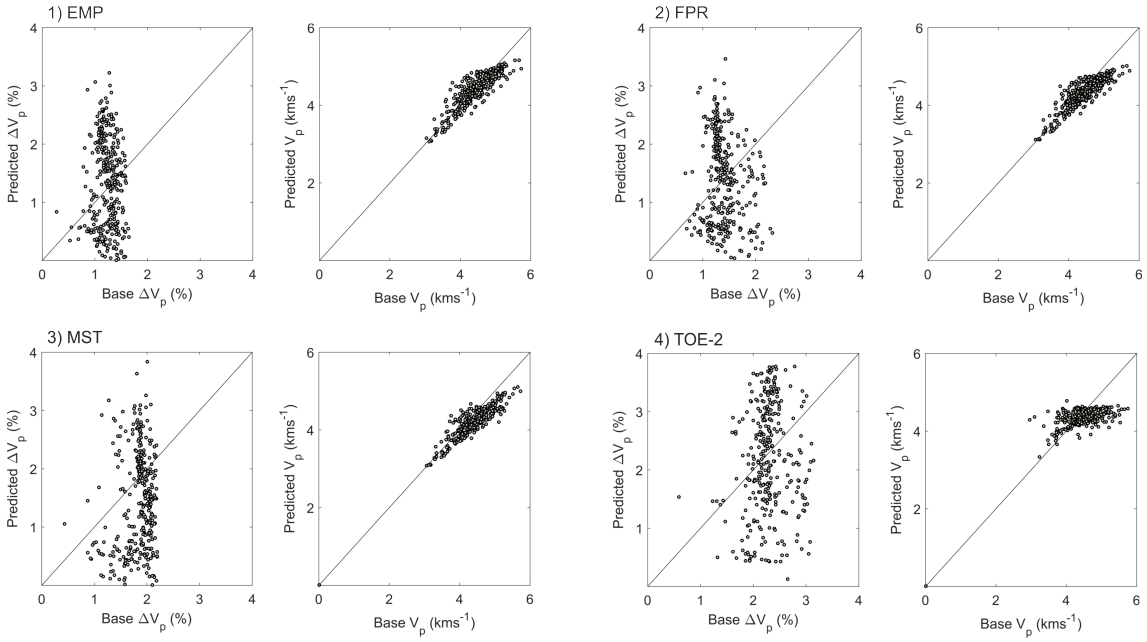

Figure 4.11: Crossplots showing the absolute velocity and percentage change associated with the overburden scenario of Figure 4.9, predicted by the linear regression surfaces of Table 4.3 against those predicted by the original inverted model (i.e. base case).

4.3. Note that the TOE-2 parameters are derived from a P-wave only inversion. This is because it is not possible to define accurate parameter relationships using the results of an unconstrained inversion (e.g. Figure 4.8). Due to this, the third order coefficients of the TOE-1 model are also excluded (e.g. Figure 4.7). Figure 4.11 show crossplots comparing the result of the rock physics model derived from parameter-porosity-clay regression surfaces (predicted) to that derived by the original inversion (base). Presented is the absolute P-wave velocity and its percentage change associated with the same overburden chalk as that used for Figures 4.9 and 4.10.

From Table 4.3 you can see that some parameters show strong parameter-porosity-clay correlations (e.g. V_P^{gr} with R^2 value ≈ 0.8) whilst many show weak or no correlation at all (e.g. ϵ_0 with R^2 value ≈ 0.07). As a result, the models derived from the regression surfaces predict the absolute magnitude of the rock velocity relatively well but are poor when it comes to predicting percentage changes related to stress (e.g. Figure 4.11). Although not shown, little improvement is seen if greater order polynomial surfaces are fit to these poorly correlated parameters. Therefore, it is clear that shape/curvature of the stress-velocity relationship cannot be described by porosity and clay content alone. Little improvement to the predicted velocity change is made by substituting constant terms for porosity-clay relationships.

4.5.5 Coring and Damage

It is becoming increasingly clear that stress-velocity core data may not be a good representation of the velocity-stress dependence of the subsurface. Comparison studies between core samples and well log measurements indicate that *in situ* rocks have a lower stress sensitivity (e.g. Furre *et al.*, 2007). The most widely accepted explanation for this difference is that large differential stresses that occur during coring damage the sample. This is demonstrated by MacBeth & Schuett (2007) where they take stress-velocity core measurements before and after inducing damage through heating. In addition to coring damage, Plona & Cook (1995) observe hysteresis in their velocity-stress data when taking measurements through loading and unloading cycles. They find that the velocity-stress hysteresis is reduced as more loading unloading cycles are carried out. They hypothesise that this trend is due to the rock being additionally damaged during the first loading cycle. New cracks are induced orientated with their normal aligned with the least principle stress.

In a piece of separate collaborative work, I assisted in the study of analysing trends in micro-crack properties of sedimentary rocks during cycles of core loading and unloading. In this study, we use loading and unloading velocity-stress core data to invert for the unknown parameters of the MST model. The inversion results are then used to explore trends to micro-crack properties. The full study can be found in Saleh *et al.* (2017). The work utilizes loading/unloading stress-velocity core data provided by the Wolfson Multiphase Flow Laboratory. The majority of these samples also form part of the dataset

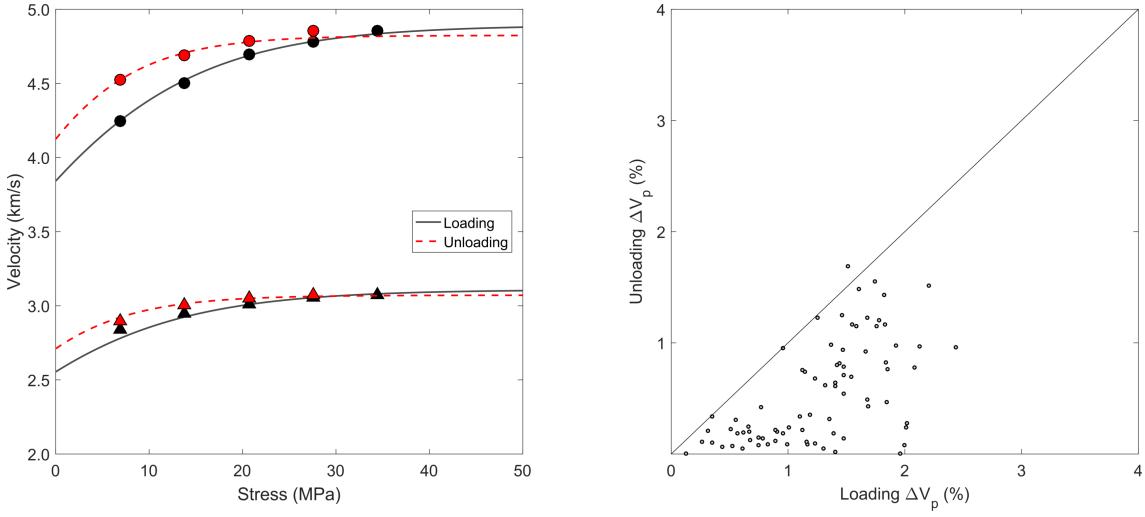

Figure 4.12: On the left is shown the MST rock physics models derived from inverting P- (circles) and S-wave (Triangles) data taken by loading (black) and unloading (red) a representative sandstone core sample. On the right is shown a crossplot of the percentage velocity change associated with the overburden chalk (i.e. 35-30MPa) predicted from the MST models derived from the loading and unloading stress-velocity core data of Saleh *et al.* (2017).

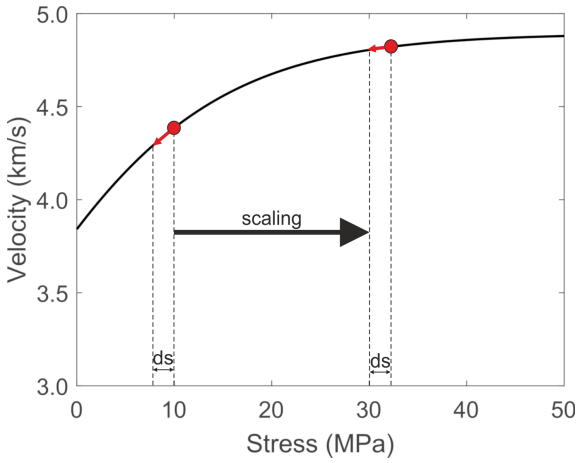

Figure 4.13: An example of scaling rock physics model approximations at low effective stresses such that the stress sensitivity of shallower (i.e. near surface) rock is not over predicted. The large stress sensitivity seen at lower stresses is thought to be a result of the damage induced to the core sample and hence an unrealistic representation of the true subsurface behaviour. Accurately determining the extent of the discrepancy between the core sample and the subsurface (i.e. the magnitude of the scaling) is extremely difficult to estimate.

used in this study (e.g. Table 4.1). The results of this work show clear discrepancies between the inverted MST models for loading and unloading data. Taking the inversion results presented in Saleh *et al.* (2017), I crossplot the overburden chalk time-lapse velocity prediction (i.e. 35-30MPa), between the models derived from loading and unloading data. The results can be seen in Figure 4.12 and show significant differences between the two sets of data. This highlights the extent in which a potentially damaged core sample can have on predicted time-lapse velocity changes.

The increased stress sensitivity observed in core data can cause unrealistic time-lapse velocity predictions for rocks with lower *in situ* stress (i.e. near-surface). Overly large time-lapse velocity changes can be predicted in these rocks for relatively small changes in stress compared to those predicted closer to the reservoir. This bias often obscures travel-time predictions and contradicts data. Often, to get around such issues, the stress-velocity relationship of rocks at low *in situ* stresses are scaled to the relationship seen at higher stresses (see Figure 4.13). However, it is difficult to justify the extent of the scaling. Such modelling issues lend evidence to *in situ* rocks having a much smaller stress sensitivity than that observed from core samples. However, estimating the damage and thus magnitude of this discrepancy is difficult to accurately quantify.

4.6 Chalk Data

Unfortunately, the database used to generate the results in Section 4.5 contains no velocity-stress core data from chalk rock. This is due to the difficulty in finding comprehensive velocity-stress chalk measurements documented in literature. Typically, chalk data is either insufficient or presented qualitatively (i.e. in the form of figures). For example, the velocity-stress chalk data presented in Borre & Fabricius (2001) contain velocity measurements only up to 10MPa whilst in Gregory (1976), the data is presented graphically without the corresponding numerical measurements. Consequently, this type of data was omitted from the main core database of Table 4.1.

However, as this particular Thesis focuses on the behaviour of chalk rock, it is important to demonstrate that the results of Section 4.5 are still relevant and applicable to chalk. To demonstrate this, I collate all the available velocity-stress core data from Borre & Fabricius (2001) and Gregory (1976) (numerical values extracted from figures via digitisation) and re-perform the model inversions of Section 4.5. I then analyse each models fit to the new chalk data and compare their time-lapse velocity predictions when subject to the production scenario of Chapter 2 (i.e. the same scenario considered in

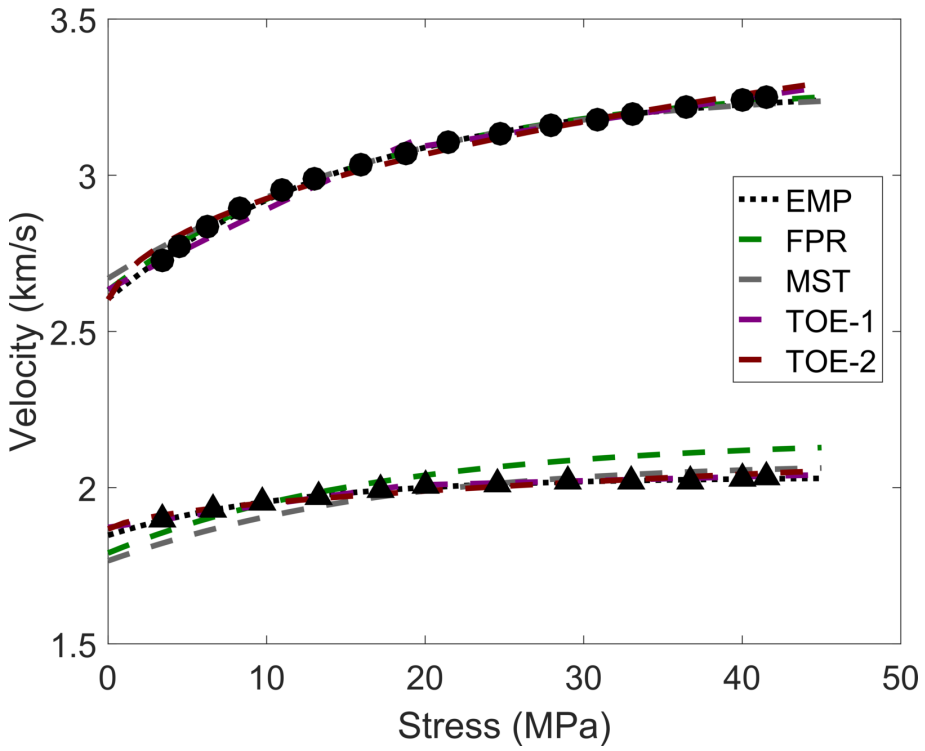

Figure 4.14: Rock physics model velocity-stress predictions for a single chalk sample. Ultrasonic P-wave (black circles) and S-wave (black triangles) data was extracted from Gregory (1976) via digitisation of their Figure 10.

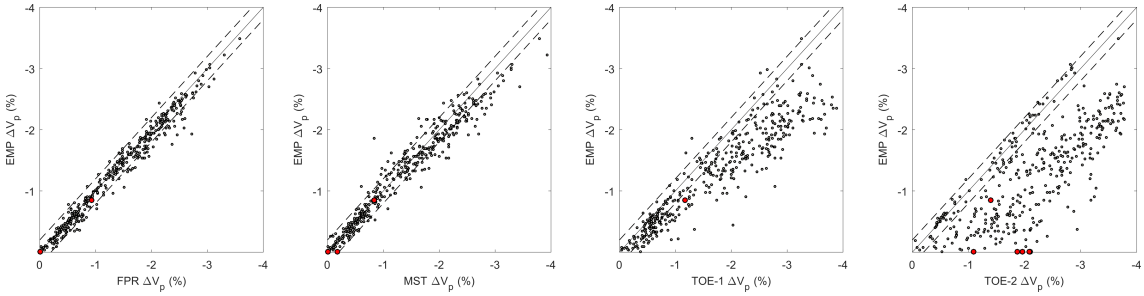

Figure 4.15: Crossplots showing the percentage velocity change associated with the overburden production scenario of Figure 4.9 predicted by each of the rock physics models for each core sample. The red points indicate the chalk samples whereas the grey points the results from the main core database re-plotted from Figure 4.9. The dotted lines represent a +/- 0.2% velocity change region. Note that only a single chalk sample is plotted on the TOE-1 crossplot due to only one chalk sample containing measurements >10MPa in which to invert for middle stress regime ($20 > \sigma' \leq 60$ MPa) coefficients.

Section 4.5, Figures 4.9, 4.10 and 4.11). In total, 6 chalk samples are extracted from the two publications.

Figure 4.14 show the inversion results for a single chalk sample taken from Gregory (1976) and is a good representation of the entire chalk dataset. The inversion results across each model show successful optimisation and a suitable good fit to the observed data. The final set of inverted parameters for each model also fall within the range observed for the main core dataset (e.g. Figure 4.4). Also, as seen in Figure 4.14, the MST and FPR models struggle to simultaneously fit both the P- and S-wave chalk data; a consequence of modelling both P- and S-wave behaviour with the same set of model parameters.

Comparison of the time-lapse velocity predictions of each model for each chalk sample when subject to the production scenario of Chapter 2 are shown in the crossplots of Figure 4.15. The production scenario used is the same as that used to generate the comparison crossplots of Chapter 2 (e.g. Figures 4.9, 4.10 and 4.11). The chalk results show a similar pattern in which the FPR, MST and EMP models predict similar changes in velocity whereas the TOE models appear to overestimate velocity changes.

The results of this section demonstrate that each rock physics model is suitably appropriate to model the velocity-stress relationship of chalk. Also, the limitations of each model in their ability to acutely fit both P- and S-wave data still hold true for chalk rock whilst similar discrepancies in time-lapse velocity predictions are seen. Limited data meant exploring the relationship between model parameters and chalk properties was not possible. However, the complex rock architecture of chalk makes it safe to presume similar difficulties in parametrising chalk rock physics models without the availability of velocity-stress core data.

4.7 Discussion

A rock physics model is an important component in relating observed time-lapse changes in seismic velocity to changes in stress and strain. In this Chapter I take some of the most commonly used rock physics models and show that by using velocity-stress core data, each model can be calibrated using similar global search techniques (i.e. the same NA search parameters) to give a relatively good fit to the observed data (e.g. Figure 4.3). Also, each model appears to predict relatively similar seismic velocity changes when subject to the overburden chalk scenario in the hydromechanical model of Chapter 2 (e.g. Figure 4.9). By combining the results of each inversion into the histograms of Figure 4.4 I present a range of plausible values (across different lithologies) for each model parameter. As literature contains little information regarding definitive parameter ranges, these results may be useful as a prior constraints for future model inversions.

Out of all models studied it appears that the two TOE models possess the worst fit to the overserved data (e.g. Figure 4.3). As a result, they also appear to consistently overestimate time-lapse velocity changes (e.g. Figure 4.9). This is due to the TOE-1 model making a linear approximation of a non-linear relationship. Whilst the TOE-2 attempts to model data that typically displays a sharp exponential trend using relationships that lack an exponential term. As the TOE-1 model is a local linear approximation, for practical purposes it requires the velocity-stress relationships to be subdivided into m linear segments. Splitting the data into linear regimes increases model error. This is further compounded since the definitive segment divisions may not be appropriate for all samples given different shape/curvature of the velocity-stress relationship. Furthermore, by subdividing the data into m regimes, the number of model coefficients n is increased to $n \times m$. Regardless, the TOE model is still widely used due to its flexibility of allowing general anisotropy (e.g. Herwanger & Koutsabeloulis, 2011) and has been adapted to *in situ* well log measurements (e.g. Donald & Prioul, 2015). The TOE-2 model on the other hand, shows a relatively good fit to velocity depth trends and stacking velocities (e.g. Korneev & Glubokovskikh, 2013). However, it appears to struggle to fit velocity-stress core data that exhibits a strong exponential trend (e.g. Figure 4.3). This, along with the loading/unloading results of Figure 4.12, raises a common question on the validity of velocity-stress core data on its representation of the velocity-stress dependence of the subsurface. Is the increase in stress sensitivity (i.e. nonlinearity) of core data large enough to render completely inadequate time-lapse velocity predictions? This question becomes even more significant if we consider that velocities are frequency and saturation dependant. Laboratory velocity data are taken from predominantly dry samples at ultrasonic frequencies, which is known to differ from seismic frequencies in saturated subsurface rocks. Accurately quantifying this discrepancy is difficult but is a science in which should

be further studied; Its potential implications for seismic history matching is extremely significant.

I show that the solution to some models (e.g. FPR, MST and TOE-2) is degraded when trying to simultaneously fit both P- and S-wave data (e.g. Figure 4.6). This is primarily due to these models using the same parameters to model both P- and S-wave behaviour. In doing so, they assume an increase in the V_P/V_S ratio i.e. Poisson's ratio, with effective stress. However, this is not observed globally across the dataset. Many core samples show an opposing decrease in V_P/V_S ratio with effective stress (e.g. Figure 4.5). This potentially could be an implication of using an effective medium based approach. However, it is most likely due to the models inability to accurately define the physics on the different interactions that P- and S-waves have with discontinuities. In most monitoring scenarios involving time-lapse seismic data, rock physics models are used predominantly to relate changes in stress and strain to seismic i.e. P-wave, velocity. Thus, in these circumstances the use of S-wave data in the inversion process might have a detrimental effect on the model solution (e.g. Figure 4.6). However, recent application of stress-dependent rock physics models are being used to predict shear-wave anisotropy (e.g. shear-wave splitting) to estimate fracture properties from microseismic data (e.g. Baird *et al.*, 2013b; Verdon & Wüstefeld, 2013). Thus, improvements to these models are necessary if quantitatively accurate predictions of S-wave behaviour are needed (e.g. Yousef & Angus, 2016). Furthermore, multi-directional measurements are needed to calibrate the anisotropic model parameters in order to improve predictions of lower-order anisotropic symmetries (e.g. Arts *et al.*, 1992; Nasseri *et al.*, 2013; Sarout *et al.*, 2014, 2015; Verdon *et al.*, 2008).

Many of the models under test in this study appear numerically stable. A relatively well constrained inversion demonstrates that only a small subset of the model space can explain the velocity-stress dependence of each sample (e.g. Figure 4.7). However, a simplification of the TOE-1 equations (equation 4.23) for an isotropic rock make the inversion for the three independent third order coefficients, c_{111}, c_{112} and c_{123} ill-posed (e.g. Figure 4.7). Specifically, the gradient of the linear P-wave velocity-stress relationship is described by the inverse relationship between parameters c_{111} and c_{112}. A similar limitation is seen in the TOE-2 equations where, a lack of multi-directional data, causes an ill-posed inversion for the individual third order coefficients A, B and C (e.g. Figure 4.8). Therefore, it appears for TOE models to be better constrained, multi-directional data is required (e.g. Donald & Prioul, 2015).

Finally, I argue that all models under test are difficult to parameterise without the availability of core data. This becomes an issue for most hydrocarbon scenarios where core samples are not typically taken (especially for non-reservoir rocks). Therefore, deriving a rock physics model in terms of more easily measurable rock properties is deemed

an important research topic. I present the equations of Eberhart-Phillips *et al.* (1989) (equations 4.32 and 4.33) which aim to address this issue by deriving the EMP model in terms of porosity and clay content. However, I show that these relationships are useful for predicting the absolute magnitude of rock velocities but limited in their prediction of time-lapse changes in seismic velocity due to changes in stress (e.g. Figure 4.10). This is because only certain parameters are related to porosity and clay content whilst others are replaced with best fitting constants. I attempt to mimic the work of Eberhart-Phillips *et al.* (1989), but derive all parameters as a simple function of porosity and clay content in an attempt to improve the time-lapse predictive capabilities. However, due to seismic velocity being a complex function of many rock properties, I find that the shape-curvature of the nonlinear relationships cannot be suitably described by porosity and clay content alone. As a result, substituting best fit constants with simple relationships does not improve time-lapse velocity predictions across all models (e.g. Figure 4.11). This poses a big question over the ability to derive accurate velocity-stress relationships without the availability of core data in which to perform a robust seismic history match.

4.8 Summary

- I demonstrate that, from a dataset of over 400 ultrasonic velocity-stress core measurements, all rock physics models can be calibrated using similar global search techniques to give a relatively good fit to observed data.
- I observe that some models fail to accurately fit both P- and S-wave stress dependence simultaneously. This is due to their assumption that the V_P/V_S ratio (hence Poisson's ratio) increases with stress.
- TOE models are limited in their approximation of an exponential relationship due to their equations lacking an exponential term. As a direct result, they appear to overestimate time-lapse changes in velocity with stress compared to other models when applied to the hydromechanical model of Chapter 2.
- Most model parameters are well constrained. However, the TOE inversions are ill-posed due to the simplification of the equations to an isotropic rock. These results are likely improved by including more multi-directional data.
- I argue that all the models are difficult to parameterise without the availability of velocity-stress core data. Parametrising models with simple porosity-clay relationships show limited capabilities in predicting time-lapse change in velocity.
- Velocity-Stress core data may not be a good representation of the velocity-stress dependence of the subsurface. It is most widely accepted that coring and removal of rocks from their *in situ* stress state causes inelastic deformation (i.e. induces more cracks). This results in an increase in the stress sensitivity. Accurately quantifying this discrepancy is difficult but is a science in which should be further studied.

5 . History Matching

when you have eliminated the impossible, whatever remains, however improbable, must be the truth?
Sir Arthur Conan Doyle

5.1 Introduction

History matching is defined as the process of identifying a set of model inputs such that its output gives an acceptable match to a set of historical observations given the uncertainty. It has often been overlooked as a method for constraining the properties of hydromechanical models due to the complexity and large runtime of Finite Element (FE) simulations. Running a suitably large number of models required for a robust history matching procedure is often unfeasible. In this Thesis, I attempt to overcome this by implementing an iterative emulator approach, known as linear Bayesian history matching. This technique has been used to great success on reservoir simulators (e.g. Craig *et al.*, 1997) and other, non-geophysical, complex computer models such as galaxy formation (e.g. Rodrigues *et al.*, 2017; Vernon & Goldstein., 2009) and genetic simulators (e.g. Vernon *et al.*, 2016). It works by constructing a Bayesian emulator of the simulator which is used as a faster surrogate (or proxy) to the original simulator. The emulator is then used to predict the simulator output at unevaluated points in the model space without running the computationally expensive simulator. It is used to identify regions of the model space that give rise to satisfactory matches between the model and the observed data. A location is deemed satisfactory based upon its measure of implausibility, a statistic that considers all forms of uncertainty in a consistent and unified manner.

In this chapter I employ the Bayesian emulator methodology to history match the mechanical properties of the overburden chalks using time-lapse seismic time-shifts. I make use of the same 2-D hydromechanical model design as that of Chapter 2 but, considering the results of the Global Sensitivity Analysis (GSA) of Chapter 3, simplify the material properties to create an analogous truth case scenario. Seismic time-shifts are forward modelled from this truth model and used as observational seismic data in the history matching process. The stress-dependant rock physics model is considered the main source of error in the process and is quantified utilising the results of Chapter 4. History matching is initially performed using near-offset time-shifts in which the emulator methodology is first validated on a simple, single layer scenario before being extended to a more complex multi-layer case. Time-shift versus offset information is then introduced into the multi-layer matching study in an attempt to improve the solution. Finally, I use the history

Layer N°	Lithology	Elastic Properties		Permeability Properties	Consolidation Properties							Dynamic Properties
		E (MPa)	v	K (m^2)	ρ ($g.cc^{-1}$)	ϕ	K_f (MPa)	K_s (MPa)	α	K_{xy}	ΔP_p (MPa)	V (Kms^{-1})
1	Shale	2800	0.31	$4.2x10^{-20}$	2.06	0.38	2400	36000	1	0.6	0	1.78
2	Sandstone	5800	0.31	$1x10^{-22}$	2.11	0.33	2400	26000	1	0.6	0	2.34
3	Chalk	25000	0.31	$1x10^{-22}$	2.30	0.23	2400	130000	0.7	0.6	0	5.04
4	Chalk	27000	0.31	$1x10^{-22}$	2.51	0.12	2400	130000	0.7	0.6	5	5.00
5	Chalk	40000	0.33	$1x10^{-22}$	2.61	0.06	2400	130000	0.8	0.6	20	6.20
6	Chalk	37000	0.31	$1x10^{-22}$	2.53	0.105	2400	130000	1	0.6	0	5.88
7	Shale	10000	0.33	$1x10^{-22}$	2.57	0.03	2400	36000	1	0.6	0	4.06
8	Sandstone	5000	0.13	$6.6x10^{-15}$	2.43	0.12	2400	36000	1	0.6	set to 110	1.90
8	Sandstone (Pay)	5000	0.13	$6.6x10^{-15}$	2.43	0.12	2100	36000	1	0.6	set to 110	1.90
9	Dolostone	60000	0.25	$1x10^{-22}$	2.79	0.01	2400	200000	1	0.6	0	6.60

Table 5.1: Poroelastic material properties for each layer in the hydromechanical model along with their pre-production (i.e. 0 years) P-wave velocity. The P-wave velocity is calculated from the static elastic properties of each layer along with a constant dynamic to static conversion of 1.3; this conversion relating to the P-wave velocities being 1.3 times larger than those derived from the static elastic moduli. Layer numbers represent increasing depth from surface.

matching results to make a final model calibration and analyse its predictive capabilities at the production well location. To ensure that the matching process takes into consideration larger, more computationally expensive 3-D scenarios, I limit the number of model runs used in the study to a relatively feasible number.

5.2 Hydromechanical model

The results of the GSA in Chapter 3 highlight that, even after the screening process, the material properties of the model are potentially over-parameterised. For example, the characterisation of the elastic and flow properties as nonlinear functions (equations 2.10, 2.11 and 2.12) introduces unnecessary complexity to the model space. Considering geological uncertainties, typical seismic resolution, and the relatively small production related stress change in the overburden, it is possibly more beneficial to define these relationships in terms of single constants.

In this history matching study, I make use of the same hydromechanical model design as that built in Chapter 2 but with a simplified set of material properties. It is assumed that the overburden remains elastic during production such that only elastic properties are defined. Also, complex nonlinear relationships are substituted for simple constants. A summary of the simplified set of material properties is shown in Table 5.1. By making these simplifications, the dimensions of the parameter space are greatly reduced. The new, simplified set of material properties are made as similar as possible to those of the *in situ* properties of the model in Chapter 2 and fall well within the ranges used in the GSA of Chapter 3. As a result, this simplified model generates suitably similar geomechanical results as those observed in Chapter 2 (e.g. Figures 2.12 and 2.13), as seen in Figure 5.1.

The seismic P-wave velocities are calculated from the Young's Modulus E, Poisson's ratio ν and bulk density ρ (see equation 2.16). However, unrealistic dynamic velocities can be derived from this methodology due to the relationship between dynamic and static elastic moduli (see Chapter 2). This is the case for the properties used in Table 5.1 where they give rise to unrealistic dynamic velocities (i.e. rock speeds below that of water, 1.5km.s^{-1}). Therefore, a dynamic to static conversion is required. For simplicity, this conversion consists of a constant ratio of 1.3, in which the dynamic P-wave velocities are 1.3 times larger than those derived from the static elastic moduli. The velocities of each layer after this conversion are shown in Table 5.1. To model the influence of production related stress change on the seismic velocity, the same rock physics model is used in which each lithological layer has the same, simple, isotropic, linear stress-velocity relationship of $dV/d\sigma' = 0.004km.s^{-1}.MPa^{-1}$. The resultant overburden time-strains $\Delta t_v/t_v$ for the model of Table 5.1 after 20 years of production are shown in Figure 5.2 whilst the time-shift offset behaviour $d\Delta t/dX$ shown graphically in Figure 5.3 and numerically in Table 5.2. Note that the CMP locations used to calculate $d\Delta t/dX$ correspond to the same ones used in Chapters 2 and 3.

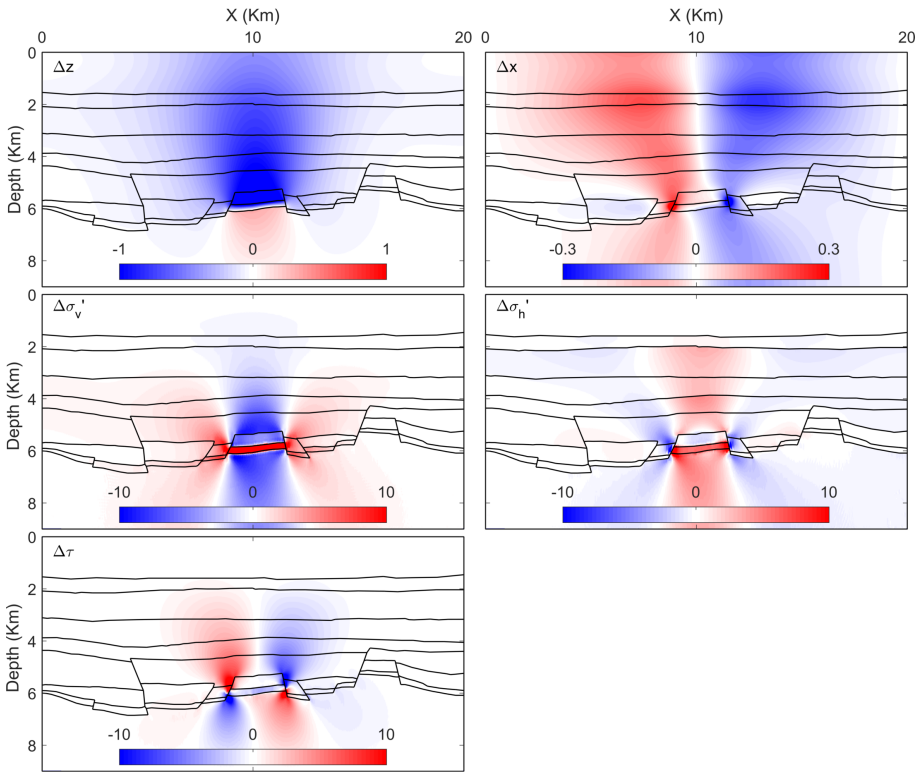

Figure 5.1: Predicted change in vertical displacement Δz, horizontal displacement Δx, vertical effective $\Delta\sigma'_v$ (c), horizontal effective stress $\Delta\sigma'_h$ (a) and shear stress $\Delta\tau$ (b) in meters and MPa from the initial pre-production state (i.e. 0 years) after 20 years of production. Note the difference in the colourbar used for Δz and Δx.

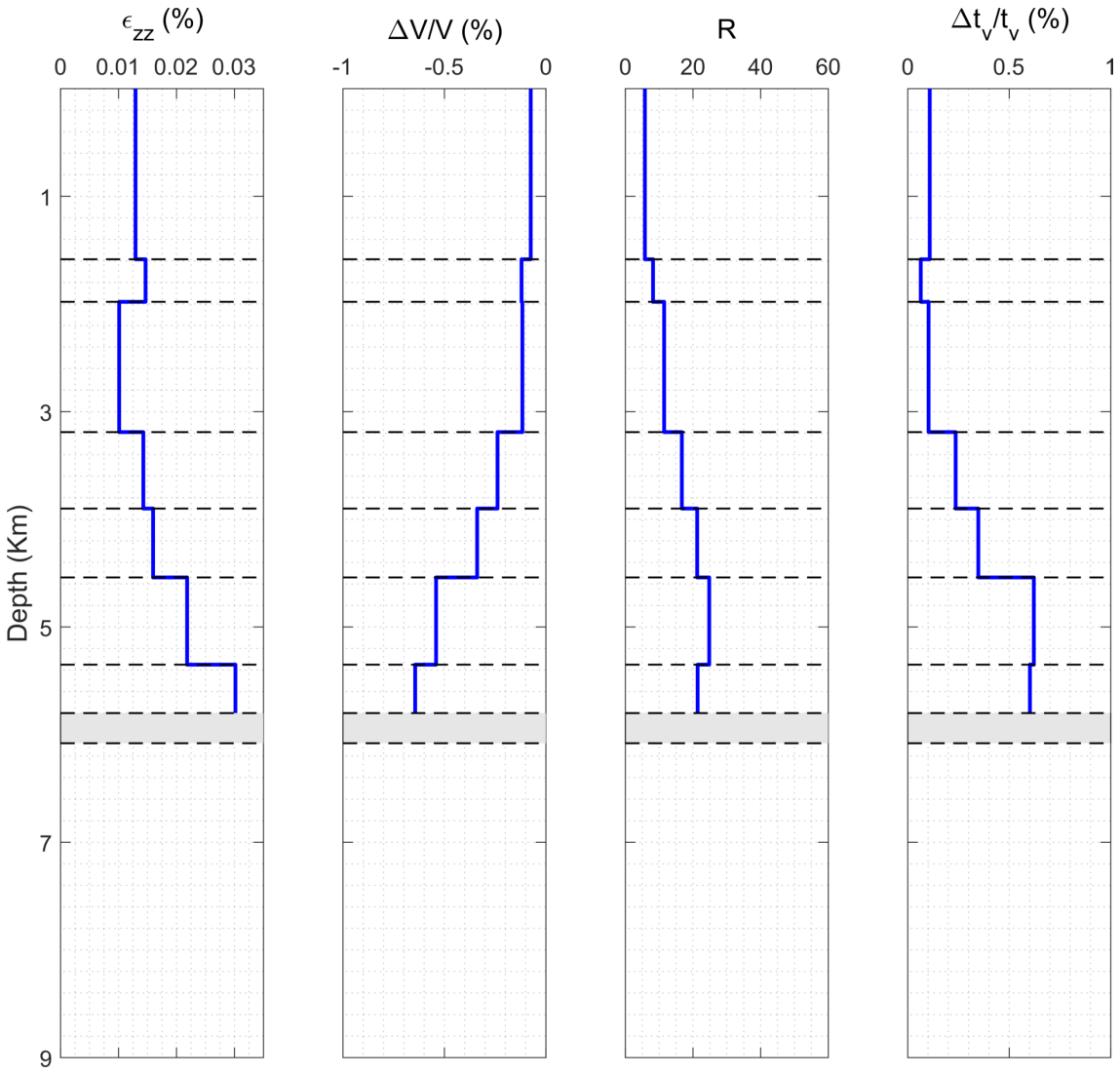

Figure 5.2: Logs which show each overburden layers time-strain $\Delta t_v/t_v$, average change in velocity $\Delta V/V$, change in thickness ε_{zz} and R-factor after 20 years of production. Layer boundaries are marked via dotted horizontal lines whilst the reservoir layer shaded. These logs are taken at the production well, located at X=10km.

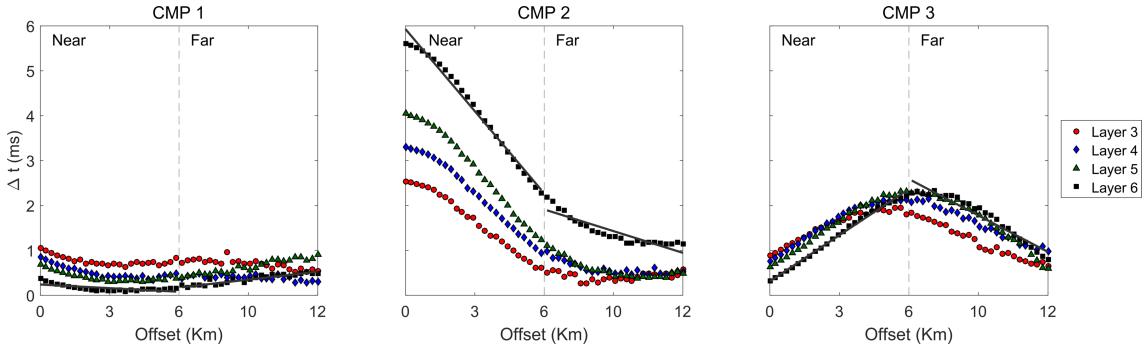

Figure 5.3: Time-shift as a function of offset for each of the three CMPs shown in Figure 2.19 after 10 years of production. The rate of change of time-shift with offset $d\Delta t/dX$ for near ($< 6km$) and far($> 6km$) offsets calculated by linear regression. For visual purposes only the regression results are shown for Layer 6 (i.e. bottom of Chalk layer 6), the full set of results can be found in Table 5.2.

Horizon N^o	$d\Delta t/dX$ (ms.Km^{-1})					
	CMP 1		CMP 2		CMP 3	
	Near	Far	Near	Far	Near	Far
Horizon 3	-0.0384	-0.0457	-0.3631	0.0055	0.1805	-0.2123
Horizon 4	-0.0633	-0.0211	-0.4307	-0.0592	0.2513	-0.2179
Horizon 5	-0.0437	-0.0840	-0.5194	-0.0987	0.3081	-0.3115
Horizon 6	-0.0269	-0.0588	-0.6098	-0.1611	0.3426	-0.2707

Table 5.2: The rate of change of time-shift with offset $d\Delta t/dX$ for each horizon in each CMP gather shown in Figure 5.3.

5.3 Bayes Linear History Matching

In this section I describe the process of linear Bayesian history matching in great detail. I describe the mathematics behind the construction of a Bayesian emulator and how it is used to iteratively history match via implausibility. I provide a simple 1-D example of Bayesian emulation taken from Rodrigues *et al.* (2017), which provides a good introduction to the emulation process.

5.3.1 Emulation

An emulator is a stochastic function that mimics a complex model but is many orders of magnitude faster to evaluate and has specified prediction uncertainty that varies across the input space (Rodrigues *et al.*, 2017). This makes it ideal for complex simulators with high dimensional input spaces and substantial run times. It allows us to explore the input space in greater detail, while taking into account the uncertainty introduced by substituting the simulator for the emulator.

Consider $f(x)$ to be a function that represents a simulator with $x = (x_1, x_2, \ldots, x_k)$ a vector of all simulator input parameters and f a vector of all simulator outputs. The emulator for output i of the function f has the form:

$$f_i(x) = \sum_j \beta_{ij} g_{ij}(x_{A_i}) + u_i(x_{A_i}) + v_i(x), \tag{5.1}$$

where x_{A_i} represents the *active* variables of x which are a subset of the initial input parameters that most influence the variation in f_i. This is typical of complex simulators with a high dimensional input space in which only a few parameters typically govern the majority of the variation in $f_i(x)$. g_{ij} are known deterministic functions of x_{A_i} (typically low order polynomial terms) while β_{ij} scalar regression coefficients. $v_i(x)$ is an uncorrelated *'nugget term'* with zero mean and constant variance $Var\big(v_i(x)\big) = \sigma^2_{v_i}$. It expresses the variation in f_i caused by the remaining inactive parameters or any model stochasticity. Finally, $u_i(x_{A_i})$ is a weakly stationary stochastic process (i.e. Gaussian process) with zero mean and a possible covariance function

$$Cov\big(u_i(x_{A_i}), u_i(x'_{A_i})\big) = \sigma^2_{u_i} exp\Big\{ - |x_{A_i} - x'_{A_i}|^2 / \theta_i^2 \Big\}, \tag{5.2}$$

where $\sigma^2_{u_i}$ is the point variance at any given x_{A_i} and θ_i the correlation length parameter that controls the strength of the correlation between two separated points in the input space (Vernon *et al.*, 2010). This specific covariance function is of the commonly used Gaussian form, however, there is no restriction to using other models such as linear, matern, squared etc. The regression terms in equation 5.1 express the global trend of the function f_i whereas the Gaussian process expresses localized deviations from the regression surface near to x.

Once generated, the emulator can be used to estimate simulator results at much greater efficiency than running the simulator itself. This opens up the possibility of conducting a full Bayesian analysis in which we can update our beliefs about $f_i(x)$ using Markov Chain Monte Carlo (MCMC) approaches. However, a full Bayes analysis requires the specification of joint prior probability distributions for all uncertain quantities in equation 5.1. This is particularly challenging as the uncertainties in the problem are complex and difficult to accurately define which can result in non-robust posterior judgements. Also, with such complex simulators, the likelihood surface is typically extremely complex which can result in non-robust Bayesian calculations (Vernon & Goldstein., 2009; Vernon *et al.*, 2010). Consequently, in this study I prefer to adopt the more tractable linear Bayesian approach. This method can be seen as an approximation to the full Bayesian analysis which requires a much simpler prior belief specification. It is based solely on the mean $E\big(f_i(x)\big)$, variance $Var\big(f_i(x)\big)$ and covariance $Cov\big(f_i(x), f_i(x')\big)$ of $f_i(x)$. Therefore, to

obtain these necessary Bayesian linear priors requires only the specification of $E(\beta_{ij})$, $Var(\beta_{ij})$, $\sigma^2_{u_i}$, $\sigma^2_{v_i}$ and θ^2_i. A Bayesian linear approximation is more straight forward than a full Bayesian analysis and is often sufficient for history matching complex computer simulators. The technical challenges involved in a full Bayesian analysis are typically not rewarded by significant improvements to the results (Vernon *et al.*, 2010).

An initial set of n model runs are performed with inputs $x^{[1]}, x^{[2]}, \ldots, x^{[3]}$ which give the corresponding outputs $D_i = \big[f_i(x^{[1]}), f_i(x^{[2]}), \ldots, f_i(x^{[n]})\big]$. Here i refers to a particular model output. To predict the simulator response at an unevaluated input, the Bayes linear adjusted expectation $E_{D_i}\big(f_i(x)\big)$ and variance $Var_{D_i}\big(f_i(x)\big)$ are calculated via:

$$E_{D_i}\big(f_i(x)\big) = E\big(f_i(x)\big) + Cov\big(f_i(x), D_i\big)Var(D_i)^{-1}\big(D_i - E(D_i)\big), \tag{5.3}$$

$$Var_{D_i}\big(f_i(x)\big) = Var\big(f_i(x)\big) - Cov\big(f_i(x), D_i\big)Var(D_i)^{-1}Cov\big(D_i, f_i(x)\big). \tag{5.4}$$

The terms $E_{D_i}\big(f_i(x)\big)$ and $Var_{D_i}\big(f_i(x)\big)$ are described as the Bayes linear adjusted mean and variance of $f_i(x)$ given D_i. $Cov\big(f_i(x), D_i\big)$ is a column vector of covariances between the new unevaluated point and known points, while $Var(D_i)^{-1}$ is an $n \times n$ matrix of covariances between known points. The emulator provides a prediction $E_{D_i}\big(f_i(x)\big)$ of what the simulator would give at an unevaluated point in the model space along with a corresponding uncertainty $Var_{D_i}\big(f_i(x)\big)$ which is x (i.e. location) dependant.

Simple 1-D Example

A helpful example of constructing a Bayesian emulator can be found in Vernon *et al.* (2016) and Rodriguez-Herrera *et al.* (2015). They describe, in detail, the process of constructing a Bayesian emulator for a simple 1-D function. I found this simple example to greatly aid my understanding of the emulation process and so have decided to include the same example for the purpose of the reader's understanding. Consider the following 1-D function

$$f(x) = 3xsin\left(\frac{5\pi(x - 0.1)}{0.4}\right), \tag{5.5}$$

for which we calculate $f(x)$ at a set of $n = 10$ equally spaced inputs between 0.1 and 0.5 (i.e $x^{[1]} = 0.1, \ldots, x^{[10]} = 0.5$)

$$D_i = \big[f(x^{[1]}), f(x^{[2]}), \ldots, f(x^{[10]})\big]. \tag{5.6}$$

Note, that we have dropped the subscript i as our function (i.e. simulator) only contains a single output.

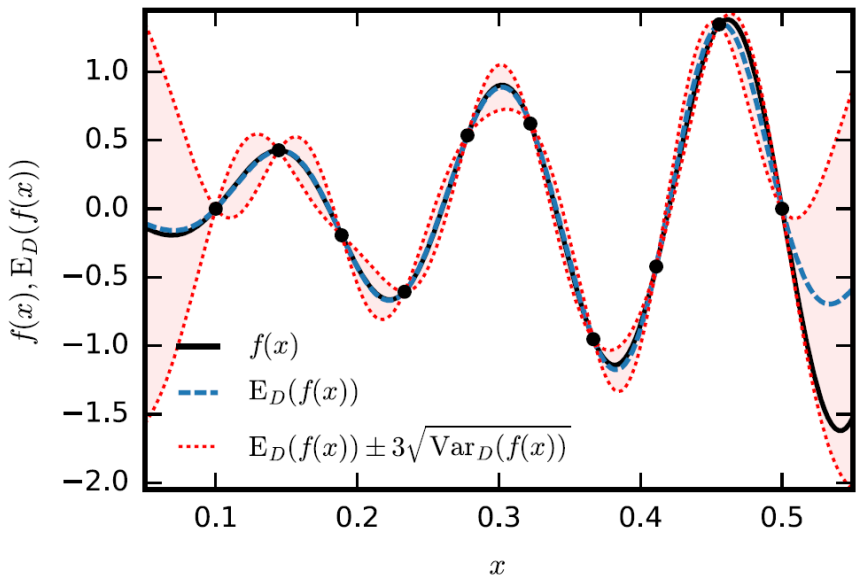

Figure 5.4: Rodriguez-Herrera *et al.* (2015). The 1-D emulator constructed in Section 5.3.1. The dashed blue line shows the emulator prediction $E_D(f(x))$ whilst the red shaded region reflecting the uncertainty in the prediction which, in this scenario, is assumed to be $E_D(f(x)) \pm 3\sqrt{Var_D(f(x))}$. The true function (equation 5.5) is shown by the solid black line and the 10 model runs used to create the matrix D shown by the black points.

The emulator regression terms $\beta_{ij} g_{ij}$ in equation 5.1 are reduced to a constant β_0. However, more complex polynomial regression terms are typical, especially when extending emulators to a higher dimensions. Also, as there are no inactive inputs, $\sigma^2_{v_i} = 0$ and equation 5.1 reduces to

$$f(x) = \beta_0 + u(x). \tag{5.7}$$

A possible prior specification is to treat the constant or mean term β_0 as known, with $E(\beta_0) = 0.1$ and hence $Var(\beta_0) = 0$. σ_u and θ of the covariance function in equation 5.2 are set to 0.6 and 0.06 respectively to render curves of moderate smoothness. We now have all the information required to calculate the terms on the right hand side of equations 5.3 and 5.4

$$E\big(f(x)\big) = \beta_0, \tag{5.8}$$

$$Var\big(f(x)\big) = \sigma_u^2, \tag{5.9}$$

$$E(D) = [\beta_0, \ldots, \beta_0]^T, \tag{5.10}$$

while $Cov\big(f(x), D\big)$ is a row vector of length n with jth component

$$\begin{aligned} Cov\big(f(x), D\big)_j &= Cov\big(u(x), u(x^{[j]})\big) \\ &= \sigma_u^2 exp\big[- |x - x^{[j]}|^2/\theta^2\big] \end{aligned} \tag{5.11}$$

and $Var(D)$ an $n \times n$ matrix with (j, k) element

$$\begin{aligned} Var(D)_{jk} &= Cov\big(u(x^{[j]}), u(x^{[k]})\big) \\ &= \sigma_u^2 exp\big[- |x^{[j]} - x^{[k]}|^2/\theta^2\big]. \end{aligned} \tag{5.12}$$

Figure 5.4 shows the result of the 1-D emulator along with the model runs D and the true simulator response $f(x)$. It can be seen that the emulator does a relatively good job at mimicking the true simulator response using a relatively small number of model runs. It precisely estimates the known run locations with zero uncertainty which is desirable since $f(x)$ is a deterministic function. The uncertainty in the emulator prediction gets larger as you move away from known locations which fittingly reflects our lack of knowledge regarding model behaviour within these regions. The true model response, falls well within the emulator uncertainty region, which in this example taken to be $\pm 3\sqrt{Var_D\big(f(x)\big)}$, for all x values. It only falls close to the boundaries of this region as we move to the edge of our model runs (i.e. $x > 0.5$ or $x < 0.1$).

5.3.2 Emulator Diagnostics

To assess the validity and adequacy of an emulator requires a diagnostic test. Bastos & O'Hagan. (2009) present a suit of such tests that are based on the comparisons between simulator outputs and emulator outputs for some test data, known as validation data. This data is defined by a sample of simulator runs, with inputs x^* not used to build the emulator.

Consider an output $f_i(x^*)$, a popular diagnostic test is one which analyses the standardized prediction error,

$$D_i^I\big(f(x^*)\big) = \frac{f_i(x^*) - E_{D_i}\big(f_i(x^*)\big)}{\sqrt{Var_{D_i}\big(f_i(x^*)\big)}}. \tag{5.13}$$

This diagnostic test analyses the standardized differences between the emulator prediction $E_{D_i}\big(f_i(x^*)\big)$ and the simulator output $f_i(x^*)$ for each of the validation runs. Large prediction errors indicate a conflict between emulator and simulator and hence the emulator should be re-assessed. Typically, values greater than 2 highlight a poor prediction (Bastos & O'Hagan., 2009). For more information regarding other diagnostic tests the reader is referred to the paper of Bastos & O'Hagan. (2009).

5.3.3 Iterative History Matching via Implausibility

Once the Bayesian emulator has been created and validated it can be used as a fast surrogate of the original simulator to identify regions of the parameter space that give rise to satisfactory matches between model $f(x)$ and observed data ξ. An input x is deemed satisfactory based upon its measure of *implausibility*. This statistic takes the difference between the emulator prediction $E_D\big(f(x)\big)$ and the observed data ξ and standardizes it with regards to all defined measures of uncertainty. For example, consider an output $f_i(x)$, its implausibility is defined as

$$I_i^2(x,\xi_i) = \frac{\Big(E_{D_i}\big(f_i(x)\big) - \xi_i\Big)^2}{Var_{D_i}\big(f_i(x)\big) + \sigma_{\delta_i}^2 + \sigma_{\epsilon_i}^2}, \tag{5.14}$$

where $Var_{D_i}\big(f_i(x)\big)$ is the emulator variance, $\sigma_{\epsilon_i}^2$ the variance of the observational data error and $\sigma_{\delta_i}^2$ the variance of the model discrepancy error. These two errors were introduced in Chapter 1, and reflect what is typically concerned as the two main causes of error in history matching. The model discrepancy term describes the deficiencies of the simulator in replicating the true physical system whilst the observational error describes the accuracy of the physical measurement.

A large implausibility measure I_i implies that the point x in the model space is statistically unlikely to yield an acceptable match to the observed data ξ_i. To categorise certain regions of the parameter space as being *'implausible'* requires a pre-defined tolerance. This is usually adapted from Pukelsheims 3σ rule (Pukelsheim, 1994) where the location x is deemed plausible if $I_i < 3$. This assumes that if $E_{D_i}\big(f_i(x)\big) - \xi_i$ is a continuous unimodal distribution, then 95% of the probability must lie within $\pm 3\sigma$ of the mean regardless of its symmetry or skew (Pukelsheim, 1994).

The implausibility measure for different outputs i can be combined by taking the maximum value

$$I_M(x,\xi) = \max_i I_i(x,\xi_i). \tag{5.15}$$

For stability purposes, when combining implausibility measures the second or the third largest value is often taken instead of the true maximum. To incorporate correlations, multivariate implausibility measures can be determined. However, these require a more detailed prior specification such as covariances between δ and ϵ (e.g. Vernon *et al.*, 2010).

History matching via implausibility is an iterative process. Regions of the parameter space are discarded as implausible in a series of waves or iterations. Within each iteration, non-implausible regions of the parameter space are determined and re-sampled. These re-sampled points are run through the simulator and the results used to update

N°.	Parameter	Nomenclature	Truth value				Range	
			Layer 3	Layer 4	Layer 5	Layer 6	min	max
1	E (MPa)	Young's Modulus	25×10^3	27×10^3	40×10^3	37×10^3	10×10^3	100×10^3
2	υ	Poisson's ratio	0.31	0.31	0.33	0.31	0.2	0.4
3	K (m^2)	Permeability	1×10^{-22}	1×10^{-22}	1×10^{-22}	1×10^{-22}	1×10^{-23}	1×10^{-18}
4	ρ ($g.cc^{-1}$)	Bulk density	2.30	2.51	2.61	2.53	2.3	2.8
5	ϕ	Porosity	0.23	0.12	0.06	0.105	0.01	0.23
6	K_f (MPa)	Fluid stiffness	2400	2400	2400	2400	2400	5000
7	K_s (MPa)	Grain stiffness	130×10^3	130×10^3	130×10^3	130×10^3	80×10^3	150×10^3
8	α	Biot coefficient	0.7	0.7	0.8	1	0.5	1
9	K_{xy}	Vertical-Horizontal stress coef	0.6	0.6	0.6	0.6	0.4	1.1
10	ΔP_p (MPa)	Over/underpressure	0	5	20	0	0	10/20/40/40

Table 5.3: Chalk layer physical properties and their parameter sensitivity ranges. Layer numbers correspond to those assigned in Table 5.1. Note the uncertainty in ΔP_p increases with depth such that it does not exceed the fracture pressure within each layer.

and improve the Bayesian emulator. The number of waves and simulator runs is typically determined via time and computational resources available. With each wave of model runs, the Bayesian emulator is constructed using only those runs that fall within the plausible region of the parameter space. With each wave, the emulator is improved due to the increased density of simulator runs and regions of the parameter space are iteratively discarded as being implausible. In later waves, the previously strong dominant active inputs will have their effect nullified and hence it is easier to incorporate additional parameters whose influence would have previously been overshadowed (Rodrigues *et al.*, 2017). However, if the entire input space is deemed implausible, or the emulator variance $Var_{D_i}\big(f_i(x)\big)$ is negligible compared to the other forms of uncertainty σ_δ^2 or σ_ϵ^2, then additional waves will not improve the current result.

5.4 Methodology

In this chapter, I employ the linear Bayesian history matching methodology in an attempt to constrain the material properties of the overburden using seismic time-shifts. Specifically, the history matching is focussed on the overburden chalk layers (e.g. layers 3 to 6 in Table 5.1 and Figure 5.1). In keeping with previous Chapters, it is assumed that there is little *a priori* knowledge of each chalk layers material properties and thus large, uniform, independent uncertainty distributions for all their physical parameters. A summary of each parameter's uncertainty range is presented in Table 5.3. These uncertainty ranges were kept suitably similar to those used in the GSA of Chapter 3. It should be noted that the range of uncertainty in the overpressure parameter ΔP_p increases with depth such that it does not exceed the fracture pressure within each layer. The production profile (Figure 2.11) and material properties of the reservoir and underburden are assumed known. In

other words, known to greater degree of accuracy (i.e. much smaller uncertainty) than that of the overburden chalks. Also, all unphysical, or algorithm specific (e.g. coupling rate, mesh type and size, etc.) parameters are assumed optimized.

The observational seismic dataset is generated from a truth case scenario which is taken to be the model created in Section 5.2. The material properties used for this model are shown in Table 5.1. Each of the four overburden chalks are mechanically different but have suitably similar uncertainty ranges for each parameter. The observational data used for the history matching are the overburden layer time-strain measurements $\Delta t_v/t_v$ (e.g. Figure 5.2) and the time-shift offset relationship $d\Delta t/dX$ at near (<6km) and far ($> 6km$) offsets (e.g. Table 5.2). As time-lapse seismic data is time consuming and costly to acquire, shooting data at yearly intervals (or less) is generally unfeasible. Therefore, I assume that $\Delta t_v/t_v$ and $d\Delta t/dX$ observations are available at only three production time-steps. In other words, there is a base survey and three ensuing monitor surveys. In keeping with the results of the GSA in Chapter 3, the monitor surveys are taken at 3, 5 and 10 years into production. I assume that $\Delta t_v/t_v$ observations are available across the entire model domain and are calculated at 500m intervals between X=1km and X=19km. This generates a $\Delta t_v/t_v$ observational data matrix for each chalk layer whose number of observations i is equal to the number of monitor surveys t multiplied by the number of spatial observations x. The $\Delta t_v/t_v$ observational data matrix is demonstrated in Figure 5.5. However, due to the slightly larger computational expense of raytracing, $d\Delta t/dX$ observations are assumed to be available at only 3 CMP locations. These three locations correspond to the same locations used in Chapters 2 and 3. Each CMP gather consists of 50 source receiver pairs, whose offsets range incrementally from zero to 12km. This generates a time-shift-offset dataset, for each chalk layer, whose number of observations i is equal to the total number of monitor surveys t multiplied by the number of spatial observation x (i.e. number of CMP gathers) and the number of linear regression functions m. Therefore, for each chalk layer, the complete observational data matrix ξ becomes a combination of $\Delta t_v/t_v$ and $d\Delta t/dX$ observations.

An initial *wave* of n model runs is performed whose inputs x are selected via maximum Latin Hypercube Sampling (see Chapter 3, Section 3.3.2) of the model space. For each $\Delta t_v/t_v$ and $d\Delta t/dX$ observation i in the data matrix ξ, a Bayesian emulator is created for the equivalent model output $f_i(x)$ using the results from each of the initial wave of n models runs, $D_i = \left[f_i(x^{[1]}), f_i(x^{[2]}), \ldots, f_i(x^{[n]})\right]$. Each emulator is constructed as a function of the active inputs x_A, whilst the variation in $f_i(x)$ caused by the remaining inputs expressed in the nugget term $v_i(x)$. Utilising the results of the GSA, the active variables are assumed to be the Young's Modulus E and the Biot coefficient α of each chalk layer. However, additional parameters such as the Poisson's ratio υ are introduced

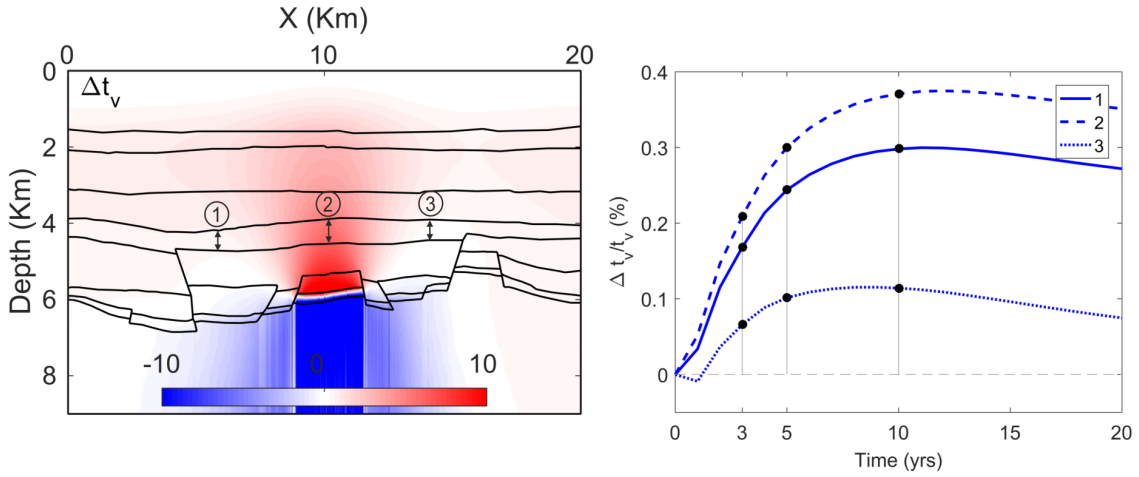

Figure 5.5: Change in two way travel-time Δt_v in milliseconds, after 20 years of production for the model of Table 5.1 shown on the left. The right image shows the time-strain $\Delta t_v/t_v$ results for a single overburden chalk at each production year taken at the three locations shown on the model geometry. The black points on the plot indicate the data used to create the observation data matrix ξ. In practice, the data matrix will contain $\Delta t_v/t_v$ measurements at 500m intervals from X=1km to X=19km along with near and far offset $d\Delta t/dX$ measurements at 3 CMP locations.

in later matching waves. Third order polynomials are used as the set of regression terms $\sum_j \beta_{ij} g_{ij}$. The final set of terms used for each output i determined via Nonlinear Least Squares (NLS) in the *fit* function in MATLAB. If x_A is greater than 2-dimensions, the extended *polyfitn* MATLAB function is used (D'Errico., 2006). The coefficients of the Gaussian process $\sigma^2_{u_i}$ and θ_i in equation 5.2 are determined via a variogram analysis of the outputs in D_i, while the variance of the nugget term $\sigma^2_{v_i}$, is determined by analysis of the residual variance given the emulator trend surface. The process of deriving these emulator terms is explained in greater detail in the following Section 5.4.1. Once created, the emulator is validated using the standardized prediction error diagnostic (equation 5.13).

Each emulator i is used to calculate the implausibility of unevaluated locations x in the model space via equation 5.14. An input x is deemed a potentially satisfactory match to the observed data ξ_i based upon its measure of implausibility. Multiple observations i will result in multiple emulators and hence multiple implausibility measures I_i for each location x. These are combined by taking the third maximum measure I_{M3} for each location x (equation 5.15). An input x is then deemed implausible if $I_{M3} > 3$. When calculating implausibility, it is assumed that the primary cause of the model discrepancy error δ is due to the uncertainty in the rock physics model. The main cause of the observational data error ϵ_i due to seismic repeatability. The process of deriving numerical approximations for the variance of these terms σ^2_δ and σ^2_ϵ, is described in greater detail in the following

Section 5.4.2.

In this study I use an initial set of n=75 runs and two successive matching waves each with 25 additional model runs. In each wave of analysis, all Bayesian emulators are refined and updated. The updated emulators are defined over only the regions of the model space that are deemed non-implausible using only those runs that fall within this current space. Each successive emulator is then used to update our beliefs on implausibility. In this particular study, earlier waves utilise only $\Delta t_v/t_v$ observations whilst $d\Delta t/dX$ measurements are included in later or final matching waves in an attempt to improve the final solution. A workflow describing the seismic history matching procedure is depicted in Figure 5.6.

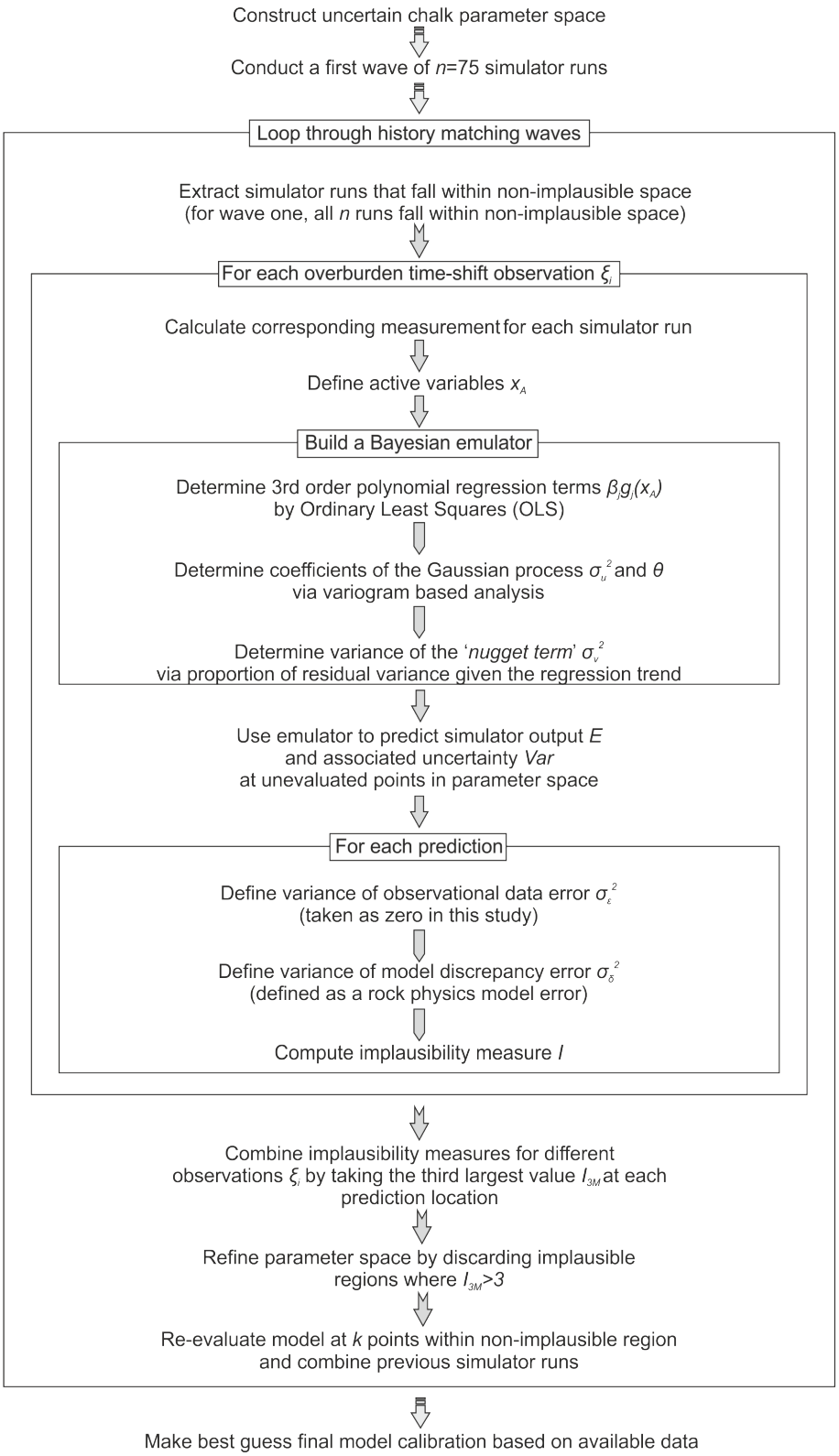

Figure 5.6: Workflow for history matching a hydromechanical model via time-lapse seismic timeshifts

5.4.1 Defining Emulator Terms: σ_u^2, σ_v^2 and θ

Accurately parameterising the covariance function of the Gaussian term $u(x_A)$ can be a difficult task (i.e. determining σ_u^2 and θ). Its shape represents our subjective assessment of the smoothness of the emulator function and the extent of the local deviations (Vernon *et al.*, 2010). The variance of the nugget term σ_v^2 then represents the uncorrelated random noise assumed to be a cause of variation to the inactive inputs which again can be difficult to determine.

In this study I choose to estimate the emulator parameters directly from the data via a semivariogram based analysis. A semivariogram $\gamma_t(L)$ is a discrete theoretical function that represents the spatial variation of a dataset. The function is typically fitted to an experimental semivariogram $\gamma_e(L)$ which measures the variation between pairs of data points $f(x)$ at different spatial distances L,

$$\gamma_e(L) = \frac{1}{2N(L)} \sum_{i=1}^{N(L)} \big[f(x_i + L) - f(x_i)\big]^2, \tag{5.16}$$

where $N(L)$ is the number of data pairs separated by distance L. Many different theoretical semivariograms exist, each with a different shape. Choosing the right model is problem specific and depends on the behaviour and shape of $\gamma_e(L)$. For the purpose of this history matching process, the covariance of $u(x_A)$ is considered to be of Gaussian form (e.g.

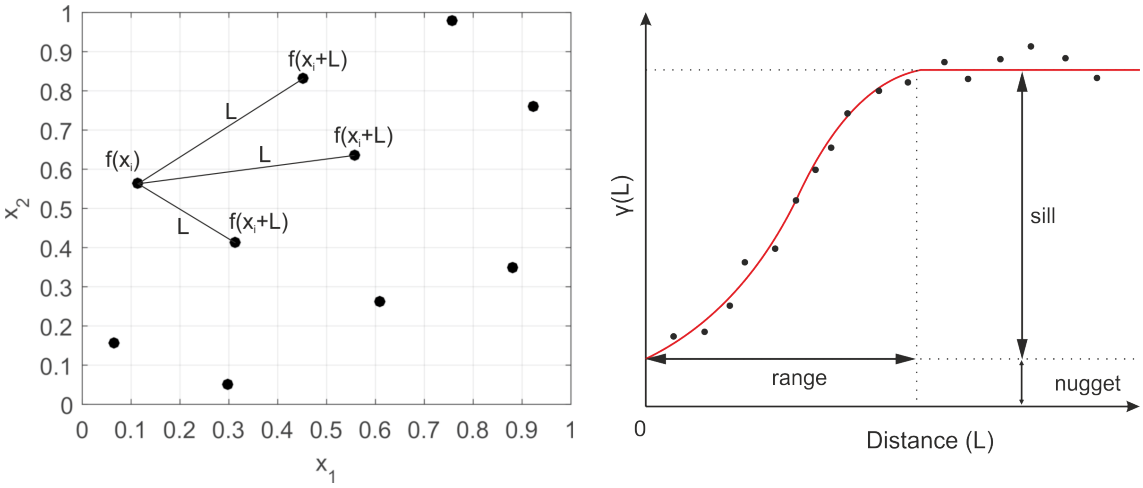

Figure 5.7: The variability $\gamma_e(L)$ between pairs of data points $f(x)$ in a 2-Dimension model space is calculated at different spatial distances L via equation 5.16. An experimental variogram is created by plotting the variability as a function of L (black points in right image). A theoretical function can be fitted to the experimental data to model the relationship (red line in right image). This is known as a theoretical semivariogram $\gamma_t(L)$ and is parameterised in terms of a sill (σ_u^2), range (θ) and nugget (σ_v^2). Typically, multiple pairs of data points at specific distances L do not exist. Therefore it is common practice to discretize L into a series of intervals or bins.

equation 5.2) and hence a Gaussian semivariogram model $\gamma_t(L)$ is used to represent $\gamma_e(L)$. This takes the form

$$\gamma_t(L) = \sigma_v^2 + \sigma_u^2\left[1 - exp\Big(-\frac{L^2}{\theta^2}\Big)\right]. \tag{5.17}$$

A schematic example of an experimental semivariogram and a fitted theoretic Gaussian function is shown in Figure 5.7.

Note that all three unknown emulator terms can be derived from the best fit Gaussian semivariogram. However, calibrating σ_v^2 direct from the sampled data can be considered non-robust. σ_v^2 expresses the semivariogram value at zero distance (i.e. $L = 0$). However, the dataset used to create $\gamma_e(L)$ does not contain duplicate runs where $L = 0$. The relatively small number of runs used in the emulation process means the distances between pairs of points is always quite large and considered insufficiently small enough to robustly determine σ_v^2. Multiple runs in which only the inactive parameters are varied would be good practice for determining σ_v^2. However, this requires significant additional model runs and hence large amounts of computational time. In this study I approximate σ_v^2 as a small proportion of the overall residual variance given the emulator trend (i.e. regression surface), $\sigma_v^2 = \alpha\sigma_{trend}^2$. Previous studies have assumed relatively small values for α (e.g. Vernon *et al.*, 2010, assumes 0.2), of which I mimic and assume $\alpha = 0.2$. For each Bayesian emulator created, the σ_v^2 is determined first then fed into a grid search inversion to find the remaining terms of the theoretical Gaussian semivariogram (i.e. σ_u^2 and θ).

5.4.2 Defining Uncertainties: δ and ϵ

For the purpose of this study, it is assumed that the majority of the model discrepancy error δ is caused by the uncertainty in the stress-dependant rock physics model $dV/d\sigma'$. An inaccurate rock physics model would lead to significant discrepancies between the model and the system even if the true physical properties of the system are inserted into the model. To model time-shift information, a constant, linear rock physics model is used. Each lithological layer has a simple, linear, isotropic stress velocity relationship in which $dV/d\sigma' = 0.004km.s^{-1}.MPa^{-1}$.

To derive an appropriate uncertainty in $dV/d\sigma'$ I utilise the inversion results of Chapter 4. They showed that even slight discrepancies between somewhat similar rock physics models can cause significant differences to predicted time-lapse velocity changes. This ambiguity is increased by orders of magnitude if models are approximated without velocity-stress core data. Taking this into consideration, I create three different scenarios. The first where $dV/d\sigma'$ is known with no uncertainty, a second where velocity-stress core data is available, then finally a third scenario in which velocity-stress core data is unavailable.

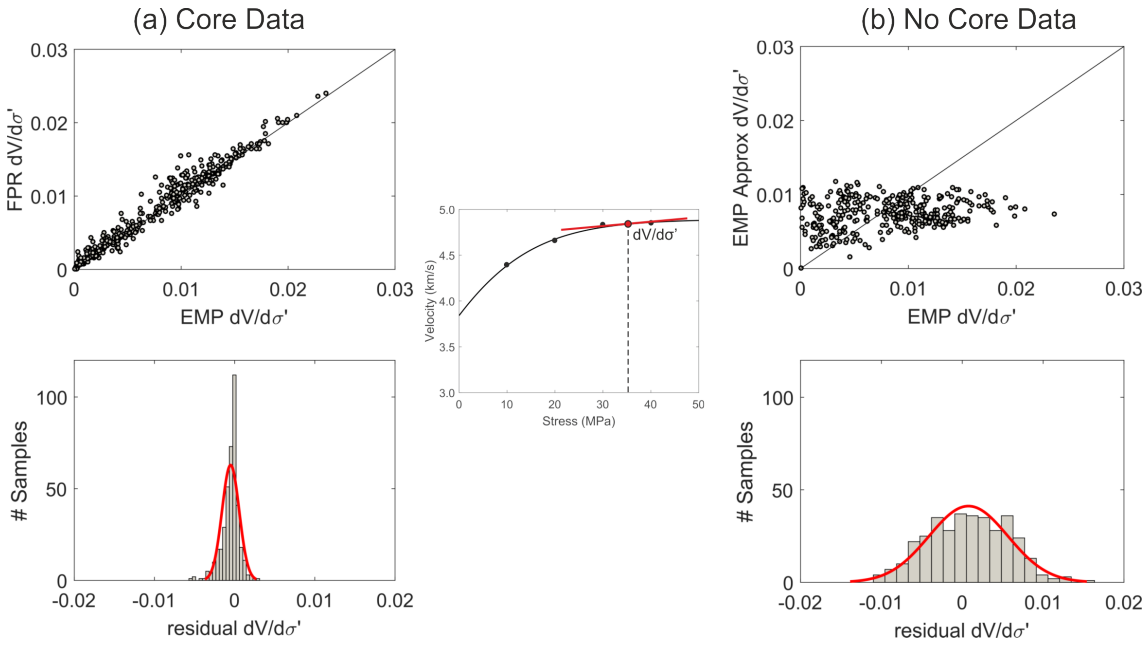

Figure 5.8: Crossplots showing the difference in the instantaneous velocity-stress relationship $dV/d\sigma'$ at 35MPa (the average *in situ* stress of the overburden chalk) predicted by different rock physics models the suite of core samples of Chapter 4. The corresponding residual distributions are shown as histograms along with their best fitting Gaussian functions, whose mean and standard deviation are presented in Table 5.4. Two scenarios are presented, (a) one which crossplots the predictions of two of the most robust models, the Empirical (EMP) and First principle (FPR) model and (b) the results of the EMP model and those derived from the EMP clay-poro regression surfaces of Table 4.3 (i.e. no velocity-stress core data). An example of a single core P-wave velocity-stress dataset along with an inverted rock physics model is also shown.

These three different scenarios create varying levels of rock physics model uncertainty and hence provides a thorough examination of its effect on seismic history matching.

To quantify the varying levels of uncertainty, I compare the predictions of different models when subject to the same velocity-stress core data. Considering 35MPa to be the average *in situ* stress of the overburden chalks, an instantaneous velocity-stress relationship (i.e. $dV/d\sigma'$) can be calculated for each inverted model of each core sample. For the scenario in which core data is available, I assume the uncertainty to stem from the discrepancy in $dV/d\sigma'$ predicted by the two most robust models, the Empirical (EMP) and First principle (FPR) model. For the scenario in which no core data is available, I compare the results of the EMP model to those from the model derived from clay-porosity regression surfaces of Table 4.3, Chapter 4. By exploring the distribution of the $dV/d\sigma'$ residuals, an approximate rock physics model error can be determined for each scenario. The residual distribution for the two scenarios is shown Figure 5.8 along with a best fit normal distribution, whose variance is given in Table 5.4.

To relate the variance of the $dV/d\sigma'$ error to a corresponding model discrepancy vari-

Scenario	$dV/d\sigma'$		δ	
	E	σ	E	ψ
Known	0.004	0	0	0
Core	0.004	0.0012	0	0.3
No core	0.004	0.0052	0	1.3

Table 5.4: The standard deviation σ of the rock physics model $dV/d\sigma'$ derived from the residual distributions shown in Figure 5.8 and their corresponding effect on the model discrepancy error δ. δ is assumed to have zero mean whilst its standard deviation dependent on the model output (i.e. not constant). ψ relates to a model output dependant standard deviation in which $\sigma_\delta = \psi E(\Delta t_v/t_v)$ and $\sigma_\delta = \psi E(d\Delta t/dX)$. Note the units of $dV/d\sigma'$ are in $km.s^{-1}.MPa^{-1}$.

ance σ_δ^2, which is defined in terms of seismic time-shifts, I employ a numerical approach. I compute 1000 different truth case scenarios whose rock physics models are sampled from a normal distribution with $E(dV/d\sigma') = 0.004$ and $Var(dV/d\sigma')$ equivalent to those stated in Table 5.4 and analyse the resultant time-shift distributions. As expected, the results show the standard deviation of the model discrepancy error σ_δ to be dependant on the model output $f_i(x)$ and hence will differ for each observation i. In other words, the larger the production related stress change, the larger the error in $\Delta t_v/t_v$ and $d\Delta t/dX$ caused by the rock physics model. Therefore, I define σ_δ as being relative to the model output i.e. $\sigma_\delta = \psi E(\Delta t_v/t_v)$ and $\sigma_\delta = \psi E(d\Delta t/dX)$, where ψ is the coefficient of variation. Representative values of ψ are determined from the 1000 model ensemble and are given in Table 5.4. Note that the results show that similar values of ψ hold true for both $\Delta t_v/t_v$ and $d\Delta t/dX$ outputs.

As the observational dataset ξ used for history matching is forward modelled directly from the simulator results, it can be considered that there is zero measurement error ϵ. However, in reality this is not the case as seismic repeatability (i.e. the ability to replicate acquisition and processing of the monitor survey) generates significant error. Although omitted from this particular study its potential implications are deliberated in the discussion.

5.5 Results

Here I present the seismic history matching results in which I attempt to constrain the material properties of the overburden chalk layers using a set of modelled seismic observations. The history matching methodology is first tested on a simple scenario in which the material properties of only a single layer are assumed uncertain. During this analysis, the process of constructing the emulator is validated via a diagnostic evaluation. The matching procedure is performed utilising only $\Delta t_v/t_v$ observations but considers all three levels

of rock physics model error. The history matching study is then extended for the case of multiple layers, in which I attempt to constrain the properties of all four overburden chalk layers. $d\Delta t/dX$ measurements are then included in later waves of the multi-layer matching procedure in an attempt to further constrain the solution. Finally, the results of the history matching are used to make a final model calibration.

5.5.1 Single Layer Case - Near-offsets

In this scenario only the material properties of chalk layer 5 are considered uncertain, whilst the properties of the other overburden chalks are assumed known (i.e. set to their truth value, Table 5.1). The range of uncertainty for each material parameter is shown in Table 5.3 and an initial set of 75 model runs generated from this model space. As only

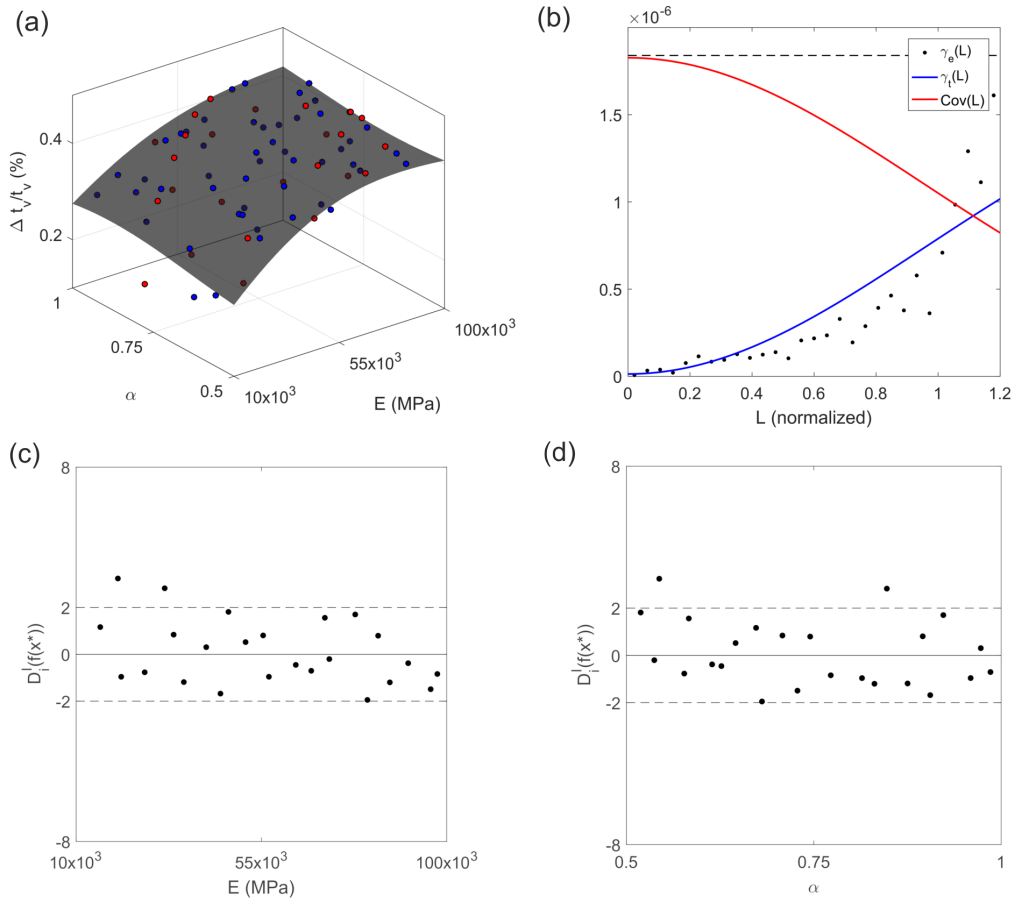

Figure 5.9: The 2-D emulator prediction $E_D(f(x))$ shown in (a) along with the corresponding 50 model runs used to generate the emulator as blue points. The experimental and theoretical variograms, along with the final covariance function, used to generate the emulator terms shown in (b). The 25 validation runs are shown as red points in (a) and their standardized prediction error $D^I\big(f(x^*)\big)$ shown in (c) and (d). Most of the prediction errors fall within the acceptable -2< $D^I\big(f(x^*)\big)$ <2 region.

a single layer is assumed uncertain only the properties of this single layer are varied in each run whilst the active parameters x_A are assumed to be the Young's Modulus E and Biot coefficient α of the corresponding chalk. The observational data vector ξ used in the history matching contains only the $\Delta t_v/t_v$ observations for the single chalk layer.

Emulator Validation

To validate the emulator process, I use the standardized prediction error $D^I\big(f(x^*)\big)$ (equation 5.13) as a diagnostic. This test requires a set of validation runs whose inputs x^* differ from those used to create the emulators. To avoid the computational expense of additional simulations, the validation runs are generated by randomly selecting 25 runs from the initial set of $n = 75$ simulations and the emulators created using the remaining 50 runs.

The diagnostic results are shown in Figure 5.9, which correspond to a single, representative emulator created for a single model output $f_i(x)$. This particular output is the $\Delta t_v/t_v$ measurement taken at location 2 in Figure 5.5 after 10 years of production. The model runs and the emulator prediction $E_D(f_i(x))$ are shown along with the experimental and theoretical variograms used to generate the emulator terms. The diagnostic results show that the emulator does a relatively good job at predicting the models behaviour. Most of the prediction errors fall within the acceptable -2< $D^I\big(f(x^*)\big)$ <2 region. Large prediction errors do appear at low E values which highlights that the emulator is potentially poorly defined within this region. However, adding the validation runs should help further constrain the emulator within this region. Although only a single emulators diagnostic results are shown, the results are representative of the entire collection of emulators created for each $\Delta t_v/t_v$ output i.

History Matching

The history matching results are shown in Figure 5.10 as implausibility maps I_{M3} of the x_A space. When the rock physics model is assumed known (i.e. $\sigma_\delta^2 = \psi = 0$), a large proportion of the x_A space can be discounted as implausible. Therefore, it is possible to constrain the uncertainty in E and α using the time-shift data. The region of the model space highlighted by the emulator as being most plausible coincides with the actual properties of the chalk layer in the truth scenario. However, the inclusion of addition simulator runs (i.e. waves) does not appear to help reduce the plausible model subspace.

When the uncertainty in the rock physics model is included in the implausibility measure, it becomes difficult to confidently discard any region of the x_A space as being implausible. This is the case even when the relatively conservative error $\psi = 0.3$ is considered. As

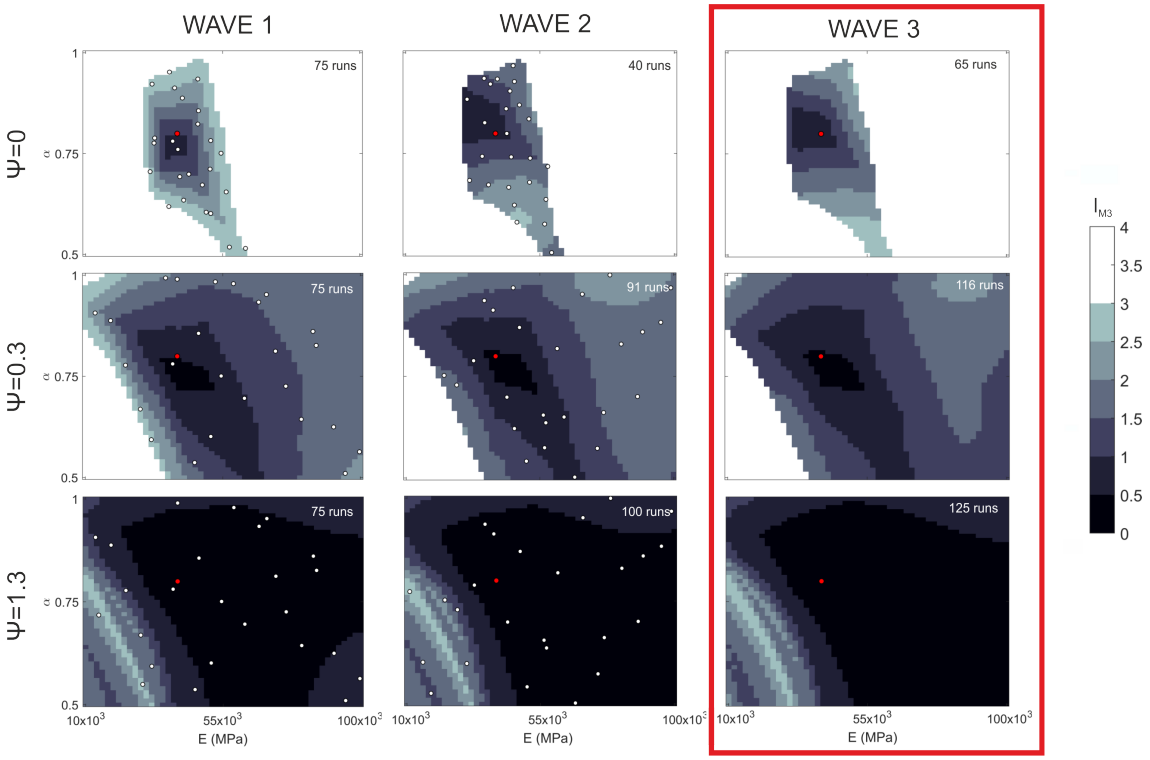

Figure 5.10: Chalk layer 5 history matching results in the form of combined implausibly maps I_{M3} of the active parameter space x_A. Shown are the results for each wave of analysis along with the varying extremities of the model discrepancy error ψ (e.g. Table 5.4). The red point indicates the properties of the truth model used to generate the observational seismic data, whilst the white points indicating the locations of future model runs used in the next wave of analysis. Also presented are the total number of simulations used to create the emulators in each wave (i.e. number of runs in matrix D). An input location is deemed implausible if $I_{M3} > 3$. Note that the data matrix ξ contains only $\Delta t_v/t_v$ observations.

a result, it becomes difficult to confidently constrain the uncertainty in E and α. Again, the inclusion of additional simulator runs do not help reduce the plausible model space.

5.5.2 Multi-layer Case - Near-offsets

I extend the case of a single layer to multiple layers in which I assume the properties of all four overburden chalks are uncertain. This generates a larger, fourfold model space whose ranges are shown in Table 5.3. The inputs for each simulator run are generated from this new model space, where the parameters of each chalk layer are varied. The observational data vector ξ again contains only $\Delta t_v/t_v$ observations.

History Matching

Firstly, I repeat the process of Figure 5.10 by attempting to constrain the material properties of the same chalk layer (i.e. chalk layer 5). I assume the same active parameters

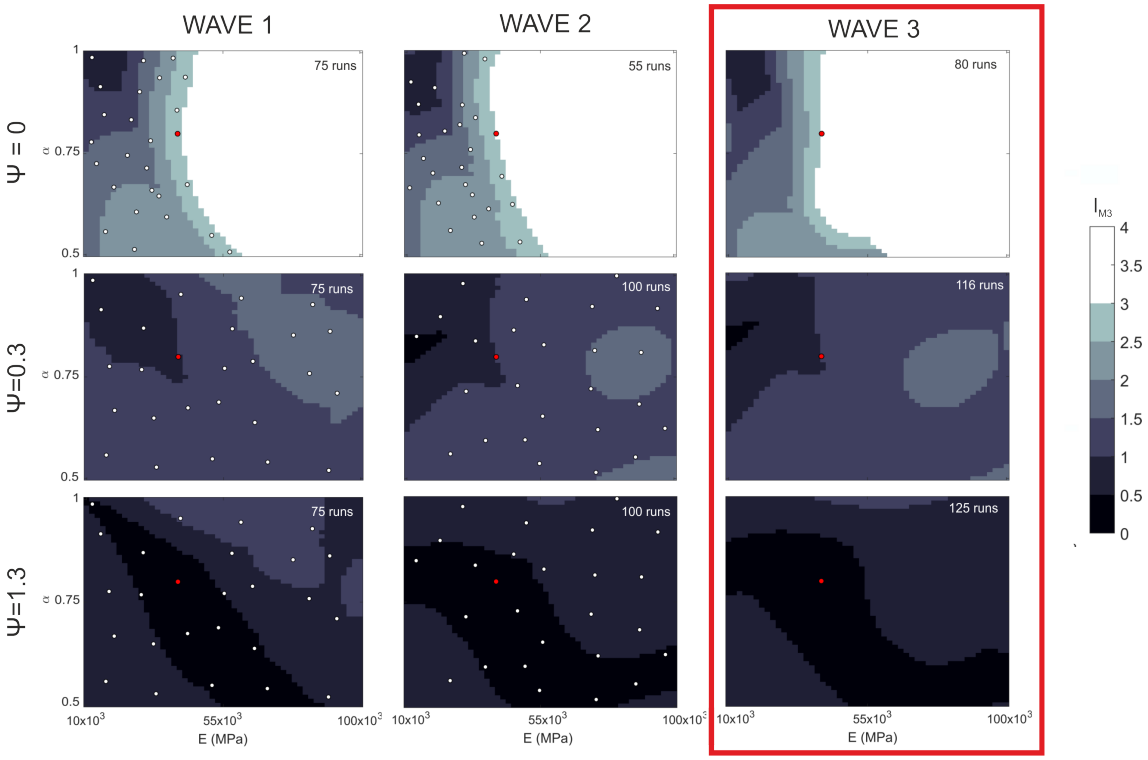

Figure 5.11: Chalk layer 5 history matching results in the form of combined implausibly maps I_{M3} of the active parameter space x_A. In this matching scenario all overburden chalk layers are uncertain and hence their properties altered for each simulator run. For more information regarding this plot refer to the caption of Figure 5.10.

in which to build the emulators (i.e. E and α) and the same $\Delta t_v/t_v$ observational data matrix ξ. The results are shown in Figure 5.11. A much smaller portion of the parameter space is identified as being implausible. Figure 5.11 also shows that the most plausible properties of the chalk to be different to those used to create the data. However, the truth model properties still fall within the plausible range. The plausible subregion of the parameter space does appear to be further constrained by additional waves of analysis, although, the true model properties still fall outside the most plausible region. When the uncertainty in the rock physics model is introduced, again no areas of the parameter space can be deemed implausible.

It has been shown in this Thesis that the hydromechanical model is complex and highly nonlinear. Therefore, attempting to history match the model holistically may be more robust than analysing and matching local regions. With this in mind, I attempt to history match all four overburden layers simultaneously. I assume that the $\Delta t_v/t_v$ model outputs are influenced by the E and α values of all four chalks layers. This increases the number of active parameters from 2 to 8 and hence each Bayesian emulator defined over an 8 dimensional parameter space. The observational data matrix ξ increases fourfold and

becomes a combination of the $\Delta t_v/t_v$ results for each chalk. The final history matching results (i.e. after three waves) are shown in Figure 5.12 as 2-D I_{M3} projections of the 8-dimensional parameter space. Panels above the leading diagonal assume there is no rock physics model error whilst panels below the diagonal assume the conservative error of $\psi = 0.3$. The results for the larger error, $\psi = 1.3$ are not shown due to its significantly large variance. A total of 10000 random input combinations are shown on these plots, the runs with the lowest implausibility plotted last to ensure they are visible. It is clear that after 3 matching waves with a total of 125 simulator runs, it is difficult to confidently constrain the uncertainty in any of the 8 active parameters even when there is no rock physics model uncertainty. It appears possible to find plausible models over the entire range of each parameter.

It is likely that 125 runs is not sufficient to accurately predict the complex model

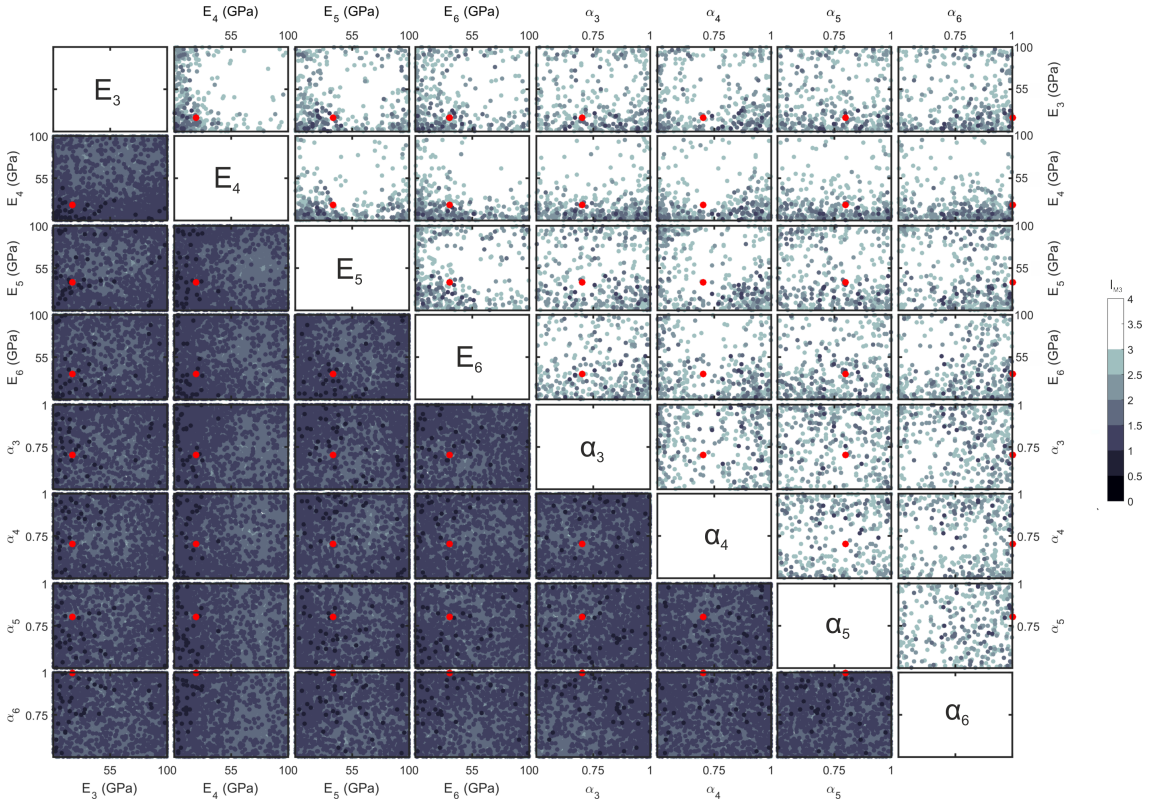

Figure 5.12: Multi-layer history matching results in the form of 2-D projections of the 8-dimensional model space consisting of the E and α parameters of each of the four calks. Plotted are the final (i.e. wave 3) implausibility measures I_{M3} of 10000 random input combinations. The models with the lowest implausibility plotted last to ensure they are visible in the plot. Panels above the leading diagonal assume no rock physics model error whilst the panels below, a conservative error of $\psi = 0.3$ (see Table 5.4). An input location is deemed implausible if $I_{M3} > 3$. The red point indicates the properties of the truth model used to generate the observational seismic data. Note that the data matrix ξ contains only $\Delta t_v/t_v$ observations.

behaviour over such a large parameter space. For that reason, I utilise the same 125 runs and half the number of active parameters. Previous results have shown that the Young's Modulus E to be the most constrained by the matching process and thus likely to be the most influential parameter (e.g. Figures 5.10 and 5.11). Therefore, the active parameter subset is reduced to just the E parameters of each chalk, whilst the Biot coefficient α is considered inactive. The final history matching results are shown in Figure 5.13. The results show vast improvements to Figure 5.12 where clear subregions of the x_A space appear implausible. Also, the most plausible models appear more constrained to certain subregions. However, as with the other results, the inclusion of the rock physics model error saturates the results which makes it difficult to constrain the uncertainty in the material properties when considered.

5.5.3 Multi-layer Case - Near and Far Offsets

In an attempt to improve the history matching procedure and further constrain the material properties of the overburden chalks, I introduce the time-shift offset behaviour $d\Delta t/dX$ into the set of seismic observations ξ. Therefore, for each chalk layer, the complete observational data matrix ξ becomes a combinations of $\Delta t_v/t_v$ and $d\Delta t/dX$ observations.

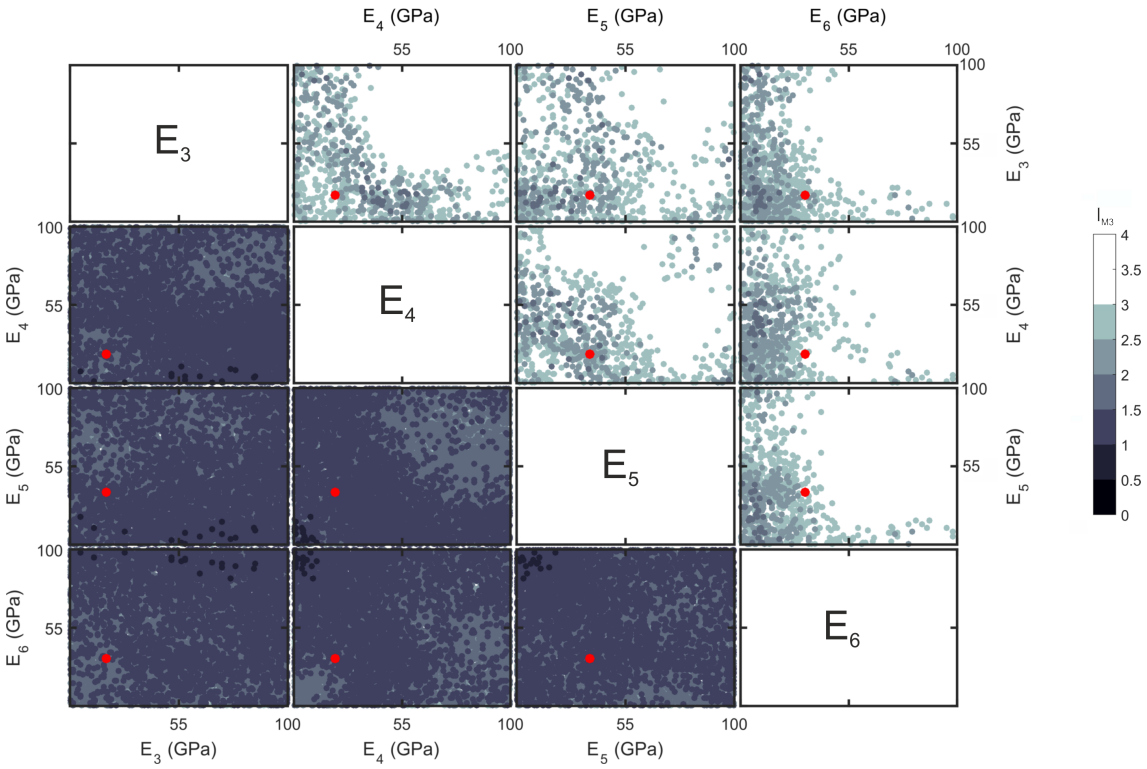

Figure 5.13: Multi-layer history matching results in the form of 2-D projections of the 4-dimensional model space consisting of the E parameters of each of the four chalks. For more information regarding this plot refer to the caption of Figure 5.12.

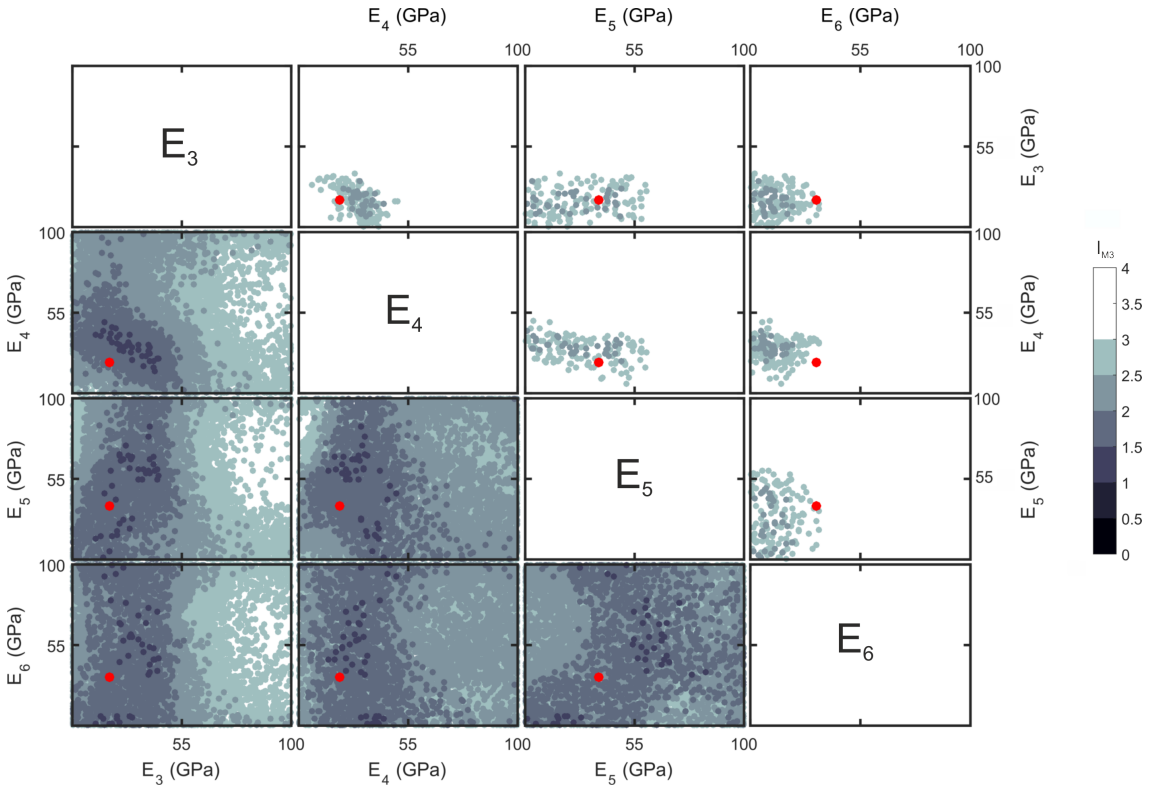

Figure 5.14: Wave 3 multi-layer history matching results in the form of 2-D projections of the 4-dimensional model space consisting of the E parameters of each of the four calks. Plotted are I_{M3} measures of 10000 random input combinations. The models with the lowest implausibility plotted last to ensure they are visible in the plot. Panels above the leading diagonal assume no rock physics model error whilst the panels below, a conservative error of $\psi = 0.3$ (see Table 5.4). An input location is deemed implausible if $I_{M3} > 3$. The red point indicates the properties of the truth model used to generate the observational seismic data. The data matrix ξ contains only $\Delta t_v/t_v$ observations for waves 1-2 with $d\Delta t/dX$ observations included in the final third wave.

The results of the GSA show that the same subset of elastic parameters can be considered as causing the majority of the variation in both $\Delta t_v/t_v$ and $d\Delta t/dX$. Therefore, it is reasonable to generate the emulators for the $d\Delta t/dX$ outputs over the same subset of active parameters as those used for $\Delta t_v/t_v$. The subset of active parameters x_A are assumed to be the collection of Young's Modulus E parameters of each of the four overburden chalk layers. Utilising the same 125 simulations as those used in the final wave of the multi-layer scenario in Figure 5.13, the $d\Delta t/dX$ emulators and observations are included in the implausibility I_{3M} calculation. The final results are shown in Figure 5.14. The same 10000 random input combinations are shown on this plot as those used in the $\Delta t_v/t_v$ only case of Figure 5.13. Panels above the leading diagonal assume there is no rock physics model error whilst the panels below the leading diagonal assume the conservative error of $\psi = 0.3$.

The results show a clear improvement in the constraint of the E terms. The majority of the 10000 input combinations are deemed implausible by the emulators leaving the plausible combinations clustered around the true properties used to generate the data. However, the inclusion of the rock physics model uncertainty once again deteriorates the result. Even the assumption of a relatively conservative error (i.e. $\psi = 0.3$) makes it extremely difficult to confidently constrain any of the four E parameters. However, including the $d\Delta t/dX$ measurements does result in the apparent clustering of implausibility measures in such a way that it becomes clear certain sub regions can be deemed more plausible than others.

Consider the ideal scenario in which the rock physics model uncertainty is known and we are able to constrain the E parameters of each layer to the subregions shown in Figure 5.14. Considering this smaller range of possible E values, I assume that the strong dominant influence of E on $\Delta t_v/t_v$ and $d\Delta t/dX$ to be suitably nullified and hence E now becomes an inactive parameter. I generate an additional fourth wave of model runs and create emulators over a new subset of active parameters, in an attempt to constrain their uncertainty. Considering the result of the GSA in Chapter 3, I generate these new emulators over the Biot coefficient α terms and subsequently the Poisson's Ratio υ terms. Unfortunately, none of the original 125 simulations fall within this constrained E space. Therefore, only the simulations generated in the final wave of runs can be used to generate the new emulators. Consequently, I increase the final wave of simulator runs from 25 to 75

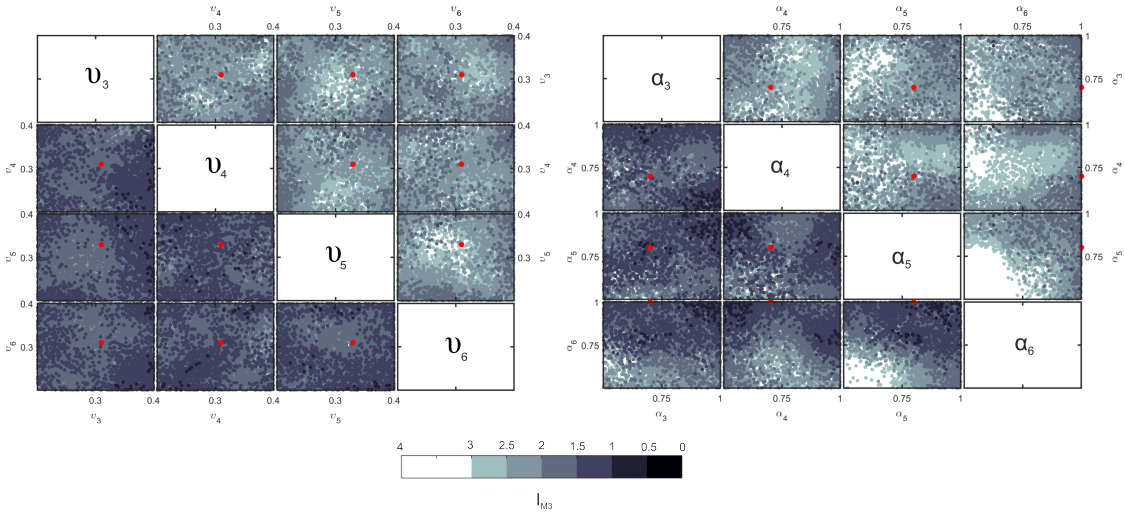

Figure 5.15: Wave 4 history matching results in the form of 2-D projections of two different 4-dimensional model spaces. One consisting of the Biot coefficient α parameters of each chalk and the other consisting of the Poisson's Ratio υ parameters. For more information regarding this plot refer to the caption of Figure 5.14. The data matrix ξ contains only $\Delta t_v/t_v$ observations for waves 1-2 with $d\Delta t/dX$ observations included in the final third and fourth wave.

such that the parameter combinations adequately sample the multi-dimensional parameter space. The implausibility projections are shown in Figure 5.15 and show that it is difficult to confidently constrain either of the α or υ parameters, even when there is no rock physics model uncertainty.

5.5.4 Model Calibration

Utilising the history matching results of the multi-layer case, I make a final model calibration in which I use the Bayesian emulators to make a best guess as to what the properties of the overburden chalks are. The Young's Modulus E of each overburden chalks are assumed to be the values taken from the most plausible set of inputs predicted by the emulators (i.e. the input combination with the lowest I_{M3} in Figure 5.14). As for the other, inactive, parameters, I assume that there is still little, *a priori* information regarding their values and hence approximate their values to be the average of their uncertainty ranges presented in Table 5.3. This includes the Biot Coefficient α and Poisson's ratio υ, as Figure 5.15 shows that it is still difficult to confidently constrain these parameters when included in the emulator process. In total, I make a total of three best guess models, one for each of the three scenarios in which assume varying levels of rock physics model uncertainty.

Figure 5.16 show the change in effective stress and subsidence at the production well predicted by each best guess models after 20 years of production. Also shown is the true stress and strain change taken from the truth case scenario and the total range of possible results based on all the simulations used in the history matching process. It is clear that all three best guess solutions do not do a great job at predicting the future stress change at the production well. Even the input combination predicted when no rock physics model error is included appears to predict a quite different response. However, the predicted models do appear to perform a much better estimation of the production related subsidence which is encouraging. Another promising result, is that by constraining the E parameter space to that shown in Figure 5.14, the possible range of predicted stress and subsidence at the well is greatly reduced. The range of possible change is shown in Figure 5.16 along with the possible range without the constraint in E. However, it is important to note that to constrain the E terms I use the results which assume no rock physics model error. Including the error in the rock physics model makes it extremely difficult to confidently constrain E and hence reduce the predicted range of possible stress and subsidence change.

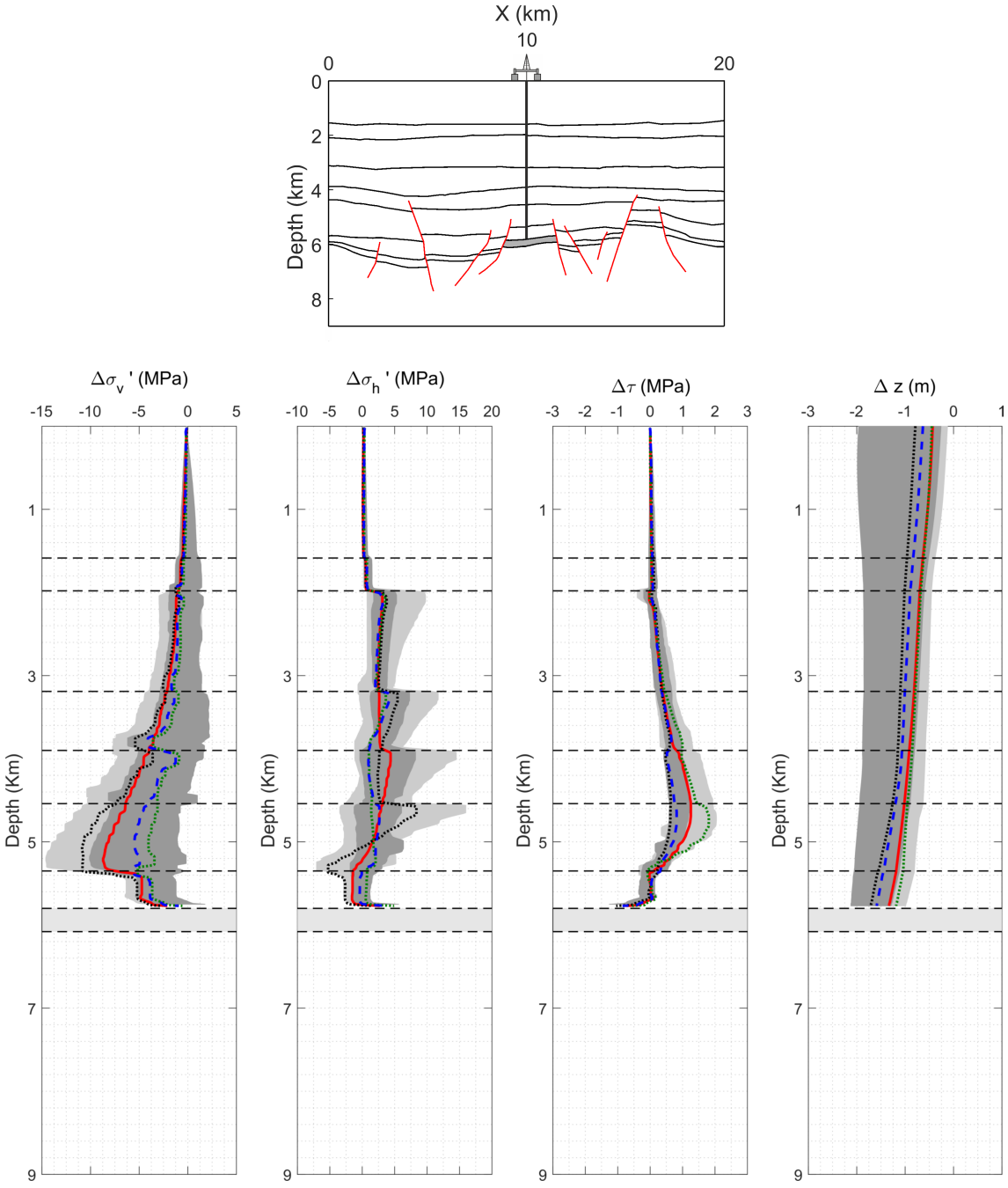

Figure 5.16: Logs showing the change in effective vertical stress $\Delta\sigma'_v$, effective horizontal stress $\Delta\sigma'_h$, shear stress $\Delta\tau$ and subsidence Δz at the production well location (top) after 20 years of production. The solid red line shows the true results whilst the dashed blue ($\psi = 0$), black ($\psi = 0.3$) and green ($\psi = 1.3$) the changes predicted by the best guess models made from the seismic history matching procedure with varying levels of rock physics model uncertainty. The light shaded region indicates the total change possible considering the results of all runs whilst the grey region those runs within a constrained E space. The dashed horizontal lines shown the location of layer boundaries whilst the reservoir layer is shaded.

5.6 Discussion

In this Chapter, using an iterative emulator approach, I have attempted to quantitatively constrain the properties of a hydromechanical model via time-lapse seismic data forward modelled from a truth case scenario. Specifically, the study focuses on constraining the properties of overburden chalks using near-offset (i.e. vertical/normal incident) seismic time-strains $\Delta t_v/t_v$ and shift offset relationships $d\Delta t/dX$ via a small (i.e. feasible) number of simulations.

A preliminarily study, focused on a simple, single layer scenario considering only $\Delta t_v/t_v$ observations, produced encouraging results. After only 3 waves of emulation, which included a total of only 125 simulations, a large proportion (approx. 80%) of the parameter space was deemed unlikely to give a suitable match to the observed data (e.g. Figure 5.10). Also, the region of the parameter space highlighted by the emulators as most likely to provide a good match (i.e. $I_{M3} < 1$) coincides with the true physical properties of the overburden chalk used to generate the data. The results show that the material properties of the chalk can be confidently constrained given the time-lapse seismic data. This is more the case for the Young's Modulus E than the Biot coefficient α, which indicates the majority of the variation in $\Delta t_v/t_v$ is caused by the layers E value.

Extending the study to a more complex multi-layered scenario makes the process slightly less conclusive. Incorporating multiple rock layers and their properties increases the number of inactive parameters and hence their combined influence over the model output (i.e. increasing the models stochasticity). This increases the variance of the emulator nugget term σ_v^2 and hence the overall emulator variance $Var_{D_i}\big(f_i(x)\big)$. The influence of the increased σ_v^2 is demonstrated in Figure 5.11 in which a much smaller percentage of the parameter space is deemed implausible (approx. 55%). Also, the complex nonlinearity of the models behaviour creates a significant bias in which the emulators predict the most plausible layer properties (i.e. $I_{M3} < 1$) to be different to those used to create the data.

Figure 5.11 demonstrates that it is not necessarily accurate to localise the emulation process and ignore the complexity of the interaction between layers. Treating the model holistically is better practice in which the subset of active parameters for a specific model output (i.e. layer) could be a combination of the material properties of multiple different layers. Figure 5.13 assumes the subset of active parameters to be the E values of all four chalks for each $\Delta t_v/t_v$ output. Although a relatively similar proportion of the parameter space is deemed implausible as that in the localised case of Figure 5.11, the results appear less biased. The most plausible input combinations appear to cluster relatively close to the true properties used to create the data. However, it is important to note that generating global emulators can significantly increase the dimensions of the parameter space as you include the properties of multiple layers. Increasing the parameter space for a set number

of simulations will successively increase the distance between pairs of points and thus increases the emulator variance at locations between known points (e.g. Figure 5.4). This is demonstrated in Figure 5.12 where the α terms are assumed active and the emulators created over a large 8-Dimensional space.

Extending the multi-layer scenario to include $d\Delta t/dX$ observations appears to significantly improve the final solution. By incorporating only a small number of $d\Delta t/dX$ measurements into the observational seismic dataset (i.e. at only 3 CMP locations) the number of plausible input combinations reduced from 7% (when only $\Delta t_v/t_v$ observations are used) to 0.8% (e.g. Figure 5.14). Additionally, the plausible set of input combinations appear more tightly clustered within the parameter space making it far easier to constrain our beliefs in each value of E (e.g. Figure 5.14). Also, it is reassuring to find that these plausible input combinations cluster around the true properties used to generate the data. It would be extremely interesting to extend this study to include a significant number more CMP gathers and hence $d\Delta t/dX$ observations to see if this result could be further improved.

Attempting to further constrain addition parameters that are less influential than the Young's Modulus E appears difficult even after its constraint (e.g. Figure 5.12). This could be due to the fact that the E values have not yet been suitably constrained such that its influence becomes such that it is considered an inactive parameter. However, as previously discussed, a small number of simulations makes it difficult to generate accurate emulators over complex multi-dimension spaces. Therefore including additional parameters into the process becomes difficult. Also, it could be considered that because only the far offset $d\Delta t/dX$ outputs appear highly influenced by the Poisson's Ratio υ (e.g. Chapter 3), a greater number of measurements (i.e. more CMPS) are required in order to suitably constrain υ. An interesting extension to this study would be to include addition $d\Delta t/dX$ observations (i.e. include more CMP locations) and attempt to re-emulate over υ.

It is assumed that the main cause of error in the seismic history matching comes from a model discrepancy error δ in the form of a rock physics model uncertainty. Analysing the residual variance between different model approximations (e.g. Figure 5.8), generates relatively large error approximations. Even when a relatively conservative approximation is considered in the implausibility calculation (i.e. $\psi = 0.3$), it becomes extremely difficult to confidently constrain any of the parameters in both the single and multi-layer scenarios (e.g. Figures 5.10, 5.13 etc.). For example, taking Figure 5.14, even when a relatively conservative error approximation (i.e. $\psi = 0.3$) is used, the number of plausible input combinations rises to 60% from 0.8%. The 60% of combinations also appearing scattered across the entire model space making it difficult to confidently constrain any of the E terms. This is because the resultant variance in the model discrepancy error σ_δ^2 is large

in comparison to the emulator variance $Var_{D_i}\big(f_i(x)\big)$. The rock physics model error is expected to be much greater in reality, closer to that of the scenario in which it is assumed no core data is available, as core data is often considered to give a poor representation of the true subsurface behaviour. This significant uncertainty makes it extremely difficult to accurately quantify the change in stress that causes the resultant time-shift. As can be seen in Figure 5.16, because of this lack of knowledge, it is plausible for there to be a change in vertical effective stress at the production well of anything between 0 to 15MPa. This uncertainty is only amplified in the case of $d\Delta t/dX$ measurements which require an anisotropic rock physics model. In this study I have simplified the rock physics relationship to be isotropic, whereas in reality, you would assume the rate of change of velocity with stress to differ depending on the direction (or angle). To make seismic history matching more robust and meaningful, the anisotropic relationship between stress and seismic velocity needs to be much more accurately defined.

It is important to emphasise the significance of the emulator terms σ_u^2 and θ on the emulation process. In this study, I choose to define these terms via a data driven approach based on a variogram analysis (e.g. Figure 5.9). However, computing an experimental variogram over multi-dimensional spaces with a relatively small sample size can result in a non-robust estimation of the spatial variance. Only a small number of data pairs exist at varying distances. Also, the variance of the nugget term σ_v^2 is very roughly approximated. A much more robust methodology would be to conduct repeated simulator runs where only the inactive variables of the model are varied. It should also be noted that the emulator diagnostic checks (e.g. Figure 5.9) were only carried out on the first wave of emulators created for the simple, single layer scenario. Validating each emulator created for each model output would be good practice for a thorough and robust history match. In this case, checking the inversion results for the theoretical variogram of each emulator is encouraged as the grid search inversion is prone to becoming biased to spuriously measurements in the experimental variogram.

As the observational data used for this history matching analysis was forward modelled directly from a modelled truth case scenario, the observational data error ϵ is considered to be zero. In reality, this is not the case. In time-lapse studies the majority of ϵ can be considered a result of seismic repeatability (i.e. the ability to replicate acquisition and processing of the monitor survey). In recent years, due to large advances in technology and processing, this error is getting smaller and smaller. An in depth analysis into seismic repeatability is beyond the scope of this Thesis, however I believe it to be far less influential than the uncertainty introduced by the rock physics model.

Typically, what makes the inclusion of $d\Delta t/dX$ observations in history matching processes difficult is the difficulty in knowing how to quickly, but accurately forward model

them from the hydromechanical model results. Raytracing has its limitations but is often used to generate travel time approximations due to its computational efficiency. Therefore, the uncertainty in the methodology used to generate CMP gathers adds to the model discrepancy error term in the history matching procedure. The most accurate way of modelling anisotropic wave propagation is to use full waveform based techniques such as finite difference approaches. In an ideal situation these techniques would be used to forward model accurate CMP gathers but they are extremely computational expensive which renders them unfeasible. In this study, I utilise the same simplified anisotropic raytracing methodology to forward model the data as I do to forward model the results used in the emulator generation. Therefore, this error has not been considered in this synthetic study but could be significant. Addition research into the difference between predicted $d\Delta t/dX$ from raytracing and full waveform techniques could shine addition light on the magnitude of this uncertainty. However, again I believe this would be far less influential than the uncertainty introduced by the rock physics model.

Although the results of the history matching appear relatively positive, it becomes evident that a lot more work and analysis is required in order to make a suitably accurate final model calibration. The results of this study demonstrate the potential of seismic history matching, although I believe such a relatively small number of simulations and iterations (i.e. waves of analysis), make it difficult for the emulators to accurately imitate such a complex model behaviour. It would be extremely interesting to extend this study to include a significantly more simulations and iterations. The more simulations and iterations, the more information available in which to make a better prediction of the model behaviour. It also enhances the ability to extend the subset of active parameters as it is quite clear their influence is not negligible. It would also be interesting to extend the study to include additional time-lapse seismic observations such as other layer $\Delta t_v/t_v$ measurements and additional $d\Delta t/dX$ measurements from more CMP gathers.

5.7 Summary

- I utilise an in iterative emulator approach to successfully history match a hydromechanical model using seismic time-shifts.
- I demonstrate that it is possible to conduct a successful seismic history match and constrain model parameters with only a small number of model perturbations.
- When the uncertainty in the rock physics model is considered, it is extremely difficulty to confidently constrain any model parameters. Its relatively large error significantly influences the history matching process.
- For a more robust history match, it is good practice to check each created emulator via diagnostic tests. The emulator terms, and how they are derived, will have a significant influence on the emulator performance and hence final solution.
- The more seismic data available, the more successful the history match. Including only a small number of time-shift offset observations into the matching study significantly improved the final result compared to that produced when only vertical time-strain observations were considered.
- The accuracy of the final model calibration will be heavily reliant on the number of model runs and extent of the seismic dataset.

6 . Conclusion

The only thing to do with good advice is to pass it on. It is never any good use to oneself
Oscar Wilde

Although time-lapse seismic data has been used to great success in the history matching of reservoir fluid properties (i.e. saturation in reservoir simulators), it has been used far less effectively for benchmarking geomechanical behaviour. The reason for this is twofold. Firstly, hydromechanical models are typically large, complex and highly nonlinear with considerably large runtimes. Secondly, isolating and extracting quantifiable mechanical information from seismic data is difficult. However, by not attempting to utilise numerical history matching techniques, are we making the most out of the geomechanical information stored in time-lapse seismic data?

In this Thesis I have attempted to answer this question by conducting a synthetic history matching study. I generate a hydromechanical model of a typical high pressure high temperature production scenario in the North Sea and utilise seismic history matching to constrain the properties of the overburden in an attempt to improve the models predictive capabilities.

The results of this Thesis conclude that by using an emulation approach to history matching, it is possible to perform a useful seismic history match with only a small number of model realisations. I manage to successfully constrain the properties of the hydromechanical model to shrink the possible range of stress and strain change along a production well. However, it is apparent that the extent in which the model can be calibrated is limited by the number of model realisations (hence history matching iterations) and the extent of the available seismic data. The complex nonlinearity of the models behaviour means that enhancing the performance of the history match (i.e. reducing the set of acceptable realisations) requires the inclusion of more and more inputs into the emulator process and as much data as possible into the implausibility calculation. The larger, more complex the parameter space, the more runs and iterations required to generate reliable emulators, while the larger the seismic dataset, the greater the number of emulators (and hence seismic forward modelling) required for the implausibility calculation. Considering the computational resources available to the hydrocarbon industry, a feasible number of simulations will most likely be much larger than that defined as feasible in this Thesis. Therefore, an interesting extension to this work would be to increase the number of emulator iterations and enhance the seismic dataset (i.e. additional time-shift offset observations from more CMP gathers) in line with industries available resources (i.e. computing and time) to analyse the extent to which the model can be constrained.

Although the emulator process makes seismic history matching more viable, the most significant obstacle is evidently the difficulty in quantifying the mechanical information from time-lapse seismic data. This is due to the complex nature of a rocks behaviour which limits our understanding of the relationship between stress and seismic velocity (i.e. rock physics modelling). Much research has gone into stress dependant rock physic modelling in which many different relationships, for all types of rock, can be found in literature. This Thesis showed that most models are robust, and do a suitably good job at fitting velocity-stress data taken from core samples in a laboratory environment. However, the problem lies in the accuracy of the relationship required for robust seismic history matching. Even slight discrepancies between different model approximations for the same core sample can cause significantly different time-lapse predictions. This makes it extremely difficult to confidently constrain any properties of the hydromechanical model from seismic data. This issue is complicated by the inability to accurately predict the velocity-stress relationship without available core data or, more importantly, the current belief that velocity-stress core data is not a good representation of the true subsurface behaviour. There is a great need for a much improved understanding of rock behaviour (i.e. rock physics), particularly the relationship between effective stress and seismic velocity and anisotropy. Seismic history matching will, until then, always be limited by our knowledge of rock physics.

It should be noted that as this Thesis was a synthetic study, the measurement and forward modelling errors were assumed to be zero. The seismic data used in the history matching was forward modelled directly from a truth case model using the same techniques as that used on the emulator runs. In reality, these errors are not zero. The difficulty in repositioning sources and receivers, especially in marine scenarios, will ultimately generate seismic repeatability errors. Also, forward modelling seismic data using ray-geometric methods is not a perfect representation of true wave propagation. Often, classical ray theory does not easily handle diffraction and thus requires a smooth velocity model which can introduce bias to the modelled data. This can increase the uncertainty in the form of an additional model discrepancy error. However, recent advances in engineering technologies, numerical algorithms and computation resources are making acquisition repeatability and seismic forward modelling more and more accurate. Although, their uncertainty must be taken into account for a robust history match, it is almost certain that these errors will, or, already are, overshadowed by the uncertainty posed by the rock physics model.

The process of building and parameterising a hydromechanical model is complicated. A large variety of data is required, each with their own varying levels of uncertainty. This makes benchmarking the model extremely important if accurate predictions are to be achieved. This Thesis demonstrates the complex nonlinearity of the models behaviour and the importance of treating the model holistically. Therefore, benchmarking the models

behaviour over the entirety of its domain is important. This makes time-lapse seismic data an essential dataset for such benchmarking due to its field wide observation. If accurate hydromechanical models are ever to be attained, it is undoubtable that time-lapse seismic will play a significant role in their calibration. However, this study has proven using time-lapse seismic data alone in a history matching procedure may limit the accuracy of the final result due to its resolution and large uncertainties. Utilising additional forms of data such as well log information may improve the final results by further reducing the set of potential inputs. An interesting extension to this study would be to include such wireline data into the emulator procedure. The significant improvements seen by incorporating time-shift offset information makes this a viable further study.

In regards to the economic benefits of mechanical seismic history matching, the financial implications of well failure and platform remediation make hydromechanical modelling an essential production monitoring tool. As long as wells keep failing and platforms continue to subside there will always be a financial benefit to forecasting the extent of production induced mechanical effects. Therefore, there will always be a financial incentive to seismic history matching. At this moment in time, the uncertainty in the relationship between stress and seismic velocity makes it extremely difficult to incorporate time-lapse seismic data into a history matching process. This should be taken into consideration before acquiring expensive 4-D seismic datasets for mechanical monitoring purposes. However, if the data is already available, then this Thesis demonstrates a relatively quick and simple seismic history matching process, utilising only a small number of model perturbations, can be used successfully to rank scenarios in terms of their likelihood. Although, it will be difficult to confidently exclude scenarios as implausible, the implausibility measure can aid in qualitative interpretation and decision making. If improvements can be made in rock physics, then seismic history matching of hydromechanical models will become far more financially appealing. However, I do believe that developing automatic emulation based history matching procedures would be a worthwhile process.

It is important to mention that due to current rather large modelling uncertainties, it becomes detrimental to over-parameterise and complicate the rock properties of your model. This will only make it more difficult for the emulator to accurately describe the model behaviour and hence harder to history matching. This becomes even more significant if you consider that only four overburden layers were used in this study with the reservoir interval or faults not included. The more rock properties included, the larger and larger the parameter space becomes for history matching. Simplifying the properties as much as possible will only be beneficial.

It is also important to note that I have not included model geometry uncertainty in this Thesis. The model geometry is made from interpreted seismic data which, as stated,

is an interpretation. Alterations to the mechanical stratigraphy of the model can vastly alter the model predictions. History matching could be an ideal process in which to highlight potential implications with the models geometry. A result in which finds no acceptable match between the model and data could indicate potential flaws in the basic model geometry. This could also be a beneficial process for highlighting the location of faults which have previously gone unseen.

In conclusion, this Thesis demonstrates the potential of seismic history matching for attracting additional mechanical information from time-lapse seismic data. However, significant research is required in rock physics in order to improve it's capability. However, the financial benefits of doing so are significant. Repeating this study on a real dataset would be an exciting extension to this Thesis.

References

Alassi, H.T., 2008. Modeling reservoir geomechanics using discrete element method: Application to reservoir monitoring. *Ph.D. Thesis*, NTNU, Norway.

Al-Harrasi, M., Grattoni, C., Fisher, Q.J. & Lane, M., 2013. Gas condensate flow behaviour within tight reservoirs. *Society of Petroleum Engineers - SPE Middle East Unconventional Gas Conference and Exhibition*, 239-257.

Ali, A.H.A., Brown, T., Delgado, R., Lee, D., Plumb, D., Smirnov, N., Marsden, R., Prado-Velarde, E., Ramsey, L., Spooner, D. & Stone, T., 2003. Watching rocks change-mechanical earth modeling. *Oilfield Review*, **15**(1), 22-39.

Angus, D.A., Verdon, J.P., Fisher, Q.J. & Kendall, J.M., 2009. Exploring trends in microcrack properties of sedimentary rocks: An audit of dry-core velocity-stress measurements. *Geophysics*, **74**(5), 193-203.

Angus, D.A., Fisher, Q.J. & Verdon, J.P., 2012. Exploring trends in microcrack properties of sedimentary rocks: An audit of dry and water saturated sandstone core velocity-stress measurements. *International Journal of Geosciences*, **3**, 822-833.

Angus, D.A., Dutko, M., Kristiansen, T.G., Fisher, Q.J., Kendall, J.M., Baird, A.F., Verdon, J.P., Barkved, O.I., Yu, J. & Zhao, S., 2015. Integrated hydro-mechanical and seismic modelling of the Valhall reservoir: A case study of predicting subsidence, AVOA and microseismicity. *Geomechanics for Energy and the Environment*, **2**, 32-44.

Arts, R.J., Rasolofosaon, N.J.P. & Zinszner, B.E., 1992. Experimental determination of the complete anisotropic viscoelastic tensor in rocks. *SEG Expanded Abstracts*, RP 1.7.

Asef, M.R. & Najibi, A.R., 2013. The effect of confining pressure on elastic wave velocities and dynamic to static Young's modulus ratio. *Geophysics*, **78**(3), D135-D142.

Avseth, P., Mukerji, T. & Mavko, G., 2010. *Quantitative seismic interpretation: applying rock physics tools to reduce interpretation risk.* Cambridge University Press, Cambridge, 7359.

Baird, A.F., Kendall, J.M. & Angus, D.A., 2013a. Frequency dependent seismic anisotropy due to fracture: fluid flow versus scattering. *Geophysics*, **78**(2), WA111-WA122.

Baird, A.F., Kendal, J.M., Verdon, J.P., Wuestefeld, A., Noble, T.E., Li, Y., Dutko, M. & Fisher, Q.J., 2013b. Monitoring increases in fracture connectivity during hydraulic stimulations from temporal variations in shear-wave splitting polarization. *Geophysical Journal International*, **195**(2), 1120-1131.

Ballester, P.J. & Carter, J.N., 2007. A parallel real-coded genetic algorithm for history matching and its application to a real petroleum reservoir. *Journal of Petroleum Science and Engineering*, **59**(3), 157-168.

Bastos, L.S. & OHagan, A., 2009. Diagnostics for Gaussian process emulators. *Technometrics*, **51**(4), 425-438.

Bloch, S., Lander, R.H. & Bonnell, L., 2002. Anomalously high porosity and permeability in deeply buried sandstone reservoirs: Origin and predictability. *AAPG bulletin*, **86**(2), 301-328.

Borre, M.K. & Fabricius, I.L., 2001. Ultrasonic velocities of water saturated chalk from the Gorm field, Danish North Sea: Sensitivity to stress and applicability of Gassmann's equation. *Nordic Petroleum Series V: Research in Petroleum Technology*, 1-18.

Brown, L., 2002. Integration of rock physics and reservoir simulation for the interpretation of time-lapse seismic data at Weyburn field, Saskatchewan. *M.Sc. dissertation*, Colorado School of Mines.

Brown, A.R., 2011. Interpretation of three-dimensional seismic data. *Society of Exploration Geophysicists and American Association of Petroleum Geologists.*

Bruno, M.S., 2002. Geomechanics and decision analysis for migration compaction related casing damage. *SPE Drilling and Completion*, **79519**, 179-188.

Campolongo, F., Saltelli, A. & Cariboni, J., 2011, From screening to quantitative sensitivity analysis: A unified approach. *Computer Physics Communications*, **183**, 978-988.

Carman, P.C. 1937. Fluid flow through a granular bed. *Trans. Inst. Chem*, England, London, **15**, 150-156.

Choi, M.K., Pyrak-Nolte, L.J., & Bobet, A., 2014. The effect of surface roughness and mixed-mode loading on the stiffness ratio K_x/K_z for fractures. *Geophysics*, **79**(5), D319-D331.

Craig, P.S., Goldstein, M., Seheult, A.H. & Smith, J.A., 1997. Pressure matching for hydrocarbon reservoirs: a case study in the use of Bayes linear strategies for large computer experiments. *Case studies in Bayesian statistics*, **3**, 36-93.

Crampin, S., 2005. A review of shear-wave splitting in the compliant crack-critical anisotropic Earth. *Wave Motion*, **41**(1), 59-77.

Crook, A.J.L., Willson, S.M., Yu, J.G. & Owen, D.R.J., 2006. Predictive modelling of structure evolution in sandbox experiments. *Journal of Structural Geology*, **28**(5), 729-744.

De Gennaro, S., Onaisi, A., Grandi, A., Ben-Brahim, L. & Neillo, V., 2008. 4D reservoir geomechanics: a case study from the HP/HT reservoirs of the Elgin and Franklin fields. *First Break*, **26**.

De Gennaro, S., Schutjens, P., Frumau, M., Fuery, M., Ita, J. & Fokker, P., 2010. The role of geomechanics in the development of an HPHT field. *American Rock Mechanics Association*, 10-450.

Dean, R.H., Gai, X., Stone, C.M. & Minkoff, S.E., 2006. A comparison of techniques for coupling porous flow and geomechanics. *Spe Journal*, **11**(1), 132-140.

Donald, J.A. & Prioul, R., 2015. In situ calibrated velocity-to-stress transforms using shear sonic radial profiles for time-lapse production analysis. *The Leading Edge*, 936-942.

Dusseault, M.B., Bruno, M.S. & Barrera, J., 1998. Casing shear: causes, cases, cures. *SPE International Oil and Gas Conference and Exhibition*, China, Society of Petroleum Engineers.

Dvorkin, J., Gutierrez, M.A. & Grana, D., 2014. *Seismic reflections of rock properties*, Cambridge University Press, Cambridge, 324.

Eberhart-Phillips, D., Han, D.H. & Zoback M. D., 1989. Empirical relationships among seismic velocity, effective pressure, porosity, and clay content in sandstone. *Geophysics*, **54**(1), 82-89.

Emerick, A.A. & Reynolds, A.C., 2012. History matching time-lapse seismic data using the ensemble Kalman filter with multiple data assimilations. *Computational Geosciences*, **16**(3), 639-659.

D'Errico, J., 2006. Mathworks: polyfitn, https://uk.mathworks.com/matlabcentral/fileexchange/34765-polyfitn.

Fjær, E. & Kristiansen, T.G., 2009. An integrated geomechanics, rock physics and seismic model. *71st EAGE Conference & Exhibition, Amsterdam.*

Forrester, A., Sobester, A. & Keane, A., 2008. *Engineering design via surrogate modelling: A practical guide.* John Wiley & Sons.

Fuck, R.F., Tsvankin, I., 2009. Analysis of the symmetry of a stressed medium using nonlinear elasticity. *Geophysics*, **74**(5), 79-87.

Furre, A. K., Andersen, M., Moen, A. S. & Tonnessen, R. K., 2007. Sonic log derived pressure depletion predictions and application to time-lapse seismic interpretation. *69th EAGE Annual Meeting*, Expanded Abstracts.

Garcia, A.G., Grandi, A. & McBeth, C., 2010. Time-shift inversion for dynamic reservoir characterization in the Elgin field. *SEG annual Meeting*, Denver.

Garcia, A.G., 2011. Dynamic reservoir characterization from overburden time-lapse strains. *Ph.D. thesis*, Institute of Petroleum Engineering, Heriot-Watt University.

Gommesen, L. & Fabricius, I.L., 2001. Dynamic and static elastic moduli of North Sea and deep sea chalk. *Physics and Chemistry of the Earth, Part A: Solid Earth and Geodesy*, **26**(1-2), 63-68.

Gosselin, O., Aanonsen, S.I., Aavatsmark, I., Cominelli, A., Gonard, R., Kolasinski, M., Ferdinandi, F., Kovacic, L. & Neylon, K., 2003. History matching using time-lapse seismic. *SPE Annual Technical Conference and Exhibition, Society of Petroleum Engineers.*

Greaves, R.J. & Fulp, T.J., 1987. Three-dimensional seismic monitoring of an enhanced oil recovery process. *Geophysics*, **52**(9), 1175-1187.

Gregory, A.R., 1976. Fluid saturation effects on dynamic elastic properties of sedimentary rocks. *Geophysics*, **41**(5), 895-921.

Grochau, M., & Gurevich, B., 2008. Investigation of core data reliability to support time-lapse interpretation in Campos basin, Brazil. *Geophysics*, **73**(2), E59-E65.

Guéguen, Y. & Sarout, J., 2011. Characteristics of anisotropy and dispersion in cracked medium. *Tectonophysics*, **503**, 165-172.

Guilbot, J. & Smith, B., 2002. 4-D constrained depth conversion for reservoir compaction estimation: Application to Ekofisk Field. *The Leading Edge*, **21**, 302-308.

Hall, S., Kendall, J.M., Maddock, L. & Fisher, Q.J., 2008. Crack density tensor inversion for analysis of changes in rock frame architecture. *Geophysical Journal International*, **173**, 577-592.

Han D.H., Nur, A. & Morgan, D., 1986. Effects of porosity and clay content on wave velocities in sandstones, *Geophysics*. **51**(11), 2093-2107.

Hansen, O., Aronsen, H.A. & Østmo, S., 2009. 4D time shifts caused by depleting a HPHT reservoir An example from the Kristin Field. *71st EAGE Conference and Exhibition, Amsterdam, The Netherlands, 8-11 June.*

Hatchell, P.J. & Bourne, S.J., 2005. Rocks under strain: Strain-induced time-lapse time shifts are observed for depleting reservoirs. *The leading Edge*, **24**(12), 1222-1225.

Hawkins, K., Howe, S., Hollingworth, S., Conroy, G., Ben-Brahim, L., Tindle, C., Taylor, N., Joffroy, G. & Onaisi, A., 2007. Production-induced stresses from time-lapse time shifts: A geomechanical case study from Franklin and Elgin fields. *The Leading Edge*, **26**, 655-662.

Hawkins, K., 2008. Defining the extent of the compacting Elgin reservoir by measuring stress-induced anisotropy. *First Break*, **26**(10).

He, T., 2006. P- and S-wave velocity measurement and pressure sensitivity analysis of AVA response. *M.Sc. dissertation*, University of Alberta.

He, Y., Angus, D.A., Blanchard, T., Garcia, A., 2016. Time-lapse seismic waveform modeling and seismic attribute analysis using hydro-mechanical models for a deep reservoir undergoing depletion. *Geophysical Journal International*, **205**, 389-407.

Heidbach, Oliver, Rajabi, Mojtaba, Reiter, Karsten, Ziegler, Moritz, WSM Team, 2016. *World Stress Map Database Release 2016*. GFZ Data Services, http://doi.org/10.5880/WSM.2016.001.

Hemsing, D., 2007. Laboratory determination of seismic anisotropy in sedimentary rock from western sedimentary rock from the western sedimentary basin. *M.Sc. dissertation*, University of Alberta.

Herwanger, J., Palmer, E. & Schiøtt, C.R., 2007. Anisotropic velocity changes in seismic time-lapse data. *SEG Technical Program Expanded Abstracts*, 2883-2887.

Herwanger, J. & Horne, S.A., 2009. Linking reservoir geomechanics and time-lapse seismics: Predicting anisotropic velocity changes and seismic attributes. *Geophysics*, **74**, W13-W33.

Herwanger, J.V., Schiøtt, C.R., Frederiksen, R., Vejæk, O.V., Wold, R., Hansen, H.J., Palmer, E. & Koutsabeloulis, N., 2010. Applying time-lapse seismic methods to reservoir management and field development planning at South Arne, Danish North Sea. *Geological Society, London, Petroleum Geology Conference series*, **7**(1), 523-535.

Herwanger, J. & Koutsabeloulis, N., 2011. *Seismic Geomechanics: How to Build and Calibrate Geomechanical Models Using 3D and 4D Seismic Data*. EAGE.

Hornby, B.E., 1998. Experimental laboratory determination of the dynamic elastic properties of drained shales. *Journal of Geophysical Research: Solid Earth*, **103**(B12), 29945-29964.

Ijasan, O., Torres-Verdn, C. & Preeg, W.E., 2013. Interpretation of porosity and fluid constituents from well logs using an interactive neutron-density matrix scale. *Interpretation*, **1**(2), 143-145.

Iske, A. & Randen, T., 2006. *Mathematical methods and modelling in hydrocarbon exploration and production*. **7**, Springer Science & Business Media.

Jackson D. & Richardson, M., 2007. *High-frequency seafloor acoustics*. Springer Science & Business Media.

Jackson, M., Percival, J., Mostaghimi, P., Tollit, B., Pavlidis, D., Pain, C., Gomes, J., Elsheikh, A.H., Salinas, P., Muggeridge, A. & Blunt, M., 2015. Reservoir modeling for flow simulation by use of surfaces, adaptive unstructured meshes, and an overlapping-control-volume finite-element method. *SPE Reservoir Evaluation & Engineering*, **18**(2), 115-132.

Jaeger, J. C., Cook, N.G. & Zimmerman, R., 2009. *Fundamentals of rock mechanics*. John Wiley & Sons.

Japsen, P., 1998. Regional velocity-depth anomalies, North Sea chalk: a record of overpressure and neogene uplift and erosion. *AAPG Bulletin*, **82**(11), 2031-2074.

Japsen, P., 2000. Investigation of multi-phase erosion using reconstructed shale trends based on sonic data, Sole Pit axis, North Sea. *Global and Planetary Change*, **24**(3), 189-210.

Jing, L. & Hudson, J.A., 2002. Numerical methods in rock mechanics. *International Journal of Rock Mechanics and Mining Sciences*, **39**(4), 409-427.

Jizba, D., 1991. Mechanical and acoustic properties of sandstones and shales. *Ph.D. dissertation*, Stanford University.

Johnston, J., & Christensen, N., 1995. Seismic anisotropy of shales. *Journal of Geophysical Research*, **100**(B4), 5991-6003.

Jones, S.M., 1995. Velocities and quality factors of sedimentary rocks at low and high effective pressures. *Geophysical Journal International*, **123**, 774-780.

Jones, J.C., 2010. *Hydrocarbons-physical properties and their relevance to utilisation*. Book-Boon, London, 1-100.

Kasiri, N. & Bashiri, A., 2010. Comparative study of different techniques for numerical reservoir simulation. *Petroleum Science and Technology*, **28**(5), 494-503.

Kendall, J.M., Fisher, Q.J., Crump, S., Maddock, J., Carter, A., Hall, S., Wookey, J., Valcke, S., Casey, M., Lloyd, G. & Ismail, W., 2007. Seismic anisotropy as an indicator of reservoir quality in siliclastic rocks. *Geological Society of London*, Special Publication, **292**, 123-136.

Khaksar, A., Griffiths, C.M., & McCann, C., 1999. Compressional and shear-wave velocities as a function of confining stress in dry sandstone. *Geophysical Prospecting*, **47**, 487-508.

Khaksar, A., Taylor, P.G., Fang, Z., Kayes, T.J., Salazar, A. & Rahman, K., 2009. Rock strength from core and logs, where we stand and ways to go. *Expanded abstracts, EAGE Conference and Exhibition*, Amsterdam, The Netherlands, 8-11 June, SPE 121972.

King, M., 1966. Wave velocities in rocks as a function of changes in overburden pressure and pore fluid saturants. *Geophysics*, **31**, 50-73.

King, M., 2002. Elastic wave propagation and permeability for rocks with multiple parallel fractures. *International Journal of Rock Mechanics and Mining Sciences*, **39**, 1033-1043.

Kirkstetter, O. & MacBeth, C., 2001. Compliance-based interpretation of dry frame pressure sensitivity in shallow marine sandstone. *Expanded Abstracts: Society of Exploration Geophysics, 71st Annual meeting*, 2132-2135.

Korneev, V. & Glubokovskikh, S., 2013. Seismic velocity changes caused by an overburden stress. *Geophysics*, **78**(5), 25-31.

Kozeny, J., 1927. Über kapillare leitung des wassers im boden: Sitzungsber. *Royal Academy of Science*, **136**, 271-306.

Kudarova, A., Hatchell, P., Brain, J. & Macbeth, C., 2016. Offset-dependence of production-related 4D time shifts: Real data examples and modeling. *SEG International Exposition and Annual Meeting, Dallas, US*, Society of Exploration Geophysicists.

Kvendseth, S.S., 1988. *Giant discovery, A history of Ekofisk through the first 20 years.* Philips Petroleum Company, Norway.

Landrø, M. & Stammeijer, J., 2004. Quantitative estimation of compaction and velocity changes using 4D impedance and traveltime changes. *Geophysics*, **69**, 949-957.

Lei, T., Sinha, B.K., & Sanders, M., 2012. Estimation of horizontal stress magnitudes and stress coefficients of velocities using borehole sonic data. *Geophysics*, **77**(3), WA181-WA196.

Lorinczi, P., Burns, A.D., Lesnic, D., Fisher, Q.J., Crook, A.J., Grattoni, C. & Rybalcenko, K., 2014. Direct and inverse methods for determining gas flow properties of shale. *Society of Petroleum Engineers*, 1-26.

MacBeth, C. & Schuett, H., 2007. The stress dependent elastic properties of thermally induced microfractures in aeolian Rotliegend Sandstone. *Geophysical Prospecting*, 55, 323-332.

Makse H.A., Gland, N., Johnson, D.L. & Schwartz, L.M., 1999. Why effective medium theory fails in granular materials. *Physical Review Letters*, **83**, 5070-5073.

Mallon, A.J. & Swarbrick, R.E., 2008. Diagenetic characteristics of low permeability, non-reservoir chalks from the Central North Sea. *Marine Petroleum Geology*, **25**(10), 1097-1108.

Marcussen, ø., Maast, T.E., Mondol, N.H., Jahren, J. & Bjørlykke, K., 2010. Changes in physical properties of a reservoir sandstone as a function of burial depth - The Etive formation, northern North Sea. *Marine and Petroleum Geology*, **27**(8), 1725-1735.

Marek, B.F., 1979. Permeability loss in depletion of reservoirs. *SPE Annual Technical Conference and Exhibition*, Society of Petroleum Engineers.

Minkoff, S.E., Stone, C.M., Bryant, S., Peszynska, M. & Wheeler, M.F., 2003. Coupled fluid flow and geomechanical deformation modeling. *Journal of Petroleum Science and Engineering*, **38**, 37-56.

Minkoff, S.E., Stone, C.M., Bryant, S. & Peszynska, M., 2004. Coupled geomechanics and flow simulation for time-lapse seismic modeling. *Geophysics*, **69**(1), 200-211.

Morris, M.D., 1991. Factorial sampling plans for preliminary computational experiments. *Technometrics*, **33**(2), 161-174.

Munns, J.W., 1985. The Valhall field: a geological overview. *Marine and Petroleum Geology*, **2**(1), 23-43.

Nagel. N.B., 2001. Compaction and subsidence issues within the petroleum industry: From Wilmington to Ekofisk and beyond. *Physics and Chemistry of the Earth, Part A: Solid Earth and Geodesy*, **26**(1-2), 3-14.

Nasseri, M.H.B., Goodfellow, S.D., Wanne, T. & Young, R.P., 2013. Thermo-hydro-mechanical properties of Cobourg limestone. *International Journal of Rock Mechanics and Mining Sciences*, **61**, 212-222.

Nicolaysen, R. & Svendsen, T., 1991. Estimating the permeability for the Troll Field using statistical methods querying a fieldwide database. *SPWLA 32nd Annual Logging Symposium*, Society of Petrophysicists and Well-Log Analysts.

Nur, A. & Simmons, G., 1969. Stress-induced velocity anisotropy in rock: an experimental study. *Journal of Geophysical Research*, **74**, 6667-6674.

Okiongbo, K.S., 2011. Petrophysical properties of North Sea shales. *Research Journal of Applied Sciences, Engineering and Technology*, **3**(1), 46-52.

Ougier-Simonin, A., Sarout, J. & Guéguen, Y. , 2009. A simplified model of effective elasticity for anisotropic shales. *Geophysics*, **74**, 57-63.

Petropoulos, G. & Srivastava, P. K., 2016. *Sensitivity Analysis in Earth Observation Modelling*. Elsevier Science & Technology Books.

Pianosi, F., Sarrazin, F. & Wagener, T., 2015. A Matlab toolbox for global sensitivity analysis. *Environmental Modelling & Software*, **70**, 80-85.

Pianosi, F. & Wagener, T., 2015. A simple and efficient method for global sensitivity analysis based on cumulative distribution functions. *Environmental Modelling & Software*, **67**, 1-11.

Pianosi, F., Beven, K., Freer, J., Hall, J.W., Rougier, J., Stephenson, D.B. & Wagener, T., 2016. Sensitivity analysis of environmental models: A systematic review with practical workflow. *Environmental Modelling & Software*, **79**, 214-232.

Plona, T. J. & Cook J. M., 1995. Effects of stress cycles on static and dynamic Young's moduli in Castlegate sandstone. *35th Rock Mechanics Symposium, Nevada, US*, 155.

Prioul, R., Bakulin, A. & Bakulin, V., 2004. Nonlinear rock physics model for estimation of 3D subsurface stress in anisotropic formations. *Geophysics*, **69**, 415-425.

Pukelsheim, F., 1994. The three sigma rule. *The American Statistician*, **48**(2), 88-91.

Rao, S. S., 2010. *The Finite Element Method in Engineering*, Elsevier.

Rickett, J., Duranti, L., Hudson, T. & Hodgson, N., 2006. Compaction and 4-D time strain at the Genesis Field. *SEG Technical Program Expanded Abstracts*, 3215-3219.

Rockfield Software Limited, 2012. *ELFEN GeoDB Generic Materials*. Swansea.

Rodriguez-Herrera, A., Koutsabeloulis, N., Onaisi, A., Fiore, J. & Selva, F., 2015. Stress-induced signatures in 4D seismic data: Evidence of overburden stress arching. *85th Annual International Meeting, SEG, Expanded Abstracts*, 5368-5372.

Rodrigues, L.F.S., Vernon, I. & Bower, R.G., 2016. Constraints on galaxy formation models from the galaxy stellar mass function and its evolution. *Monthly Notices of the Royal Astronomical Society*, **466**(2), 2418-2435.

Rojas, M., 2005. Elastic rock properties of tight gas sandstones for reservoir characterization at Rulison field, Colorado. *M.Sc. dissertation*, Colorado School of Mines.

Saleh, H., Fisher, Q., Price, D. & Angus, D., 2017. Trends in micro–crack properties of sedimentary rocks in loading and unloading mechanism. *4th EAGE Workshop on Rock Physics*, Abu Dhabai.

Saltelli, A., Annoni, P., Azzini, I., Campolongo, F., Ratto, M., 2010. Variance based sensitivity analysis of model output. Design and estimator for the total sensitivity index, *Computer Physics Communications*, **181**(2), 259-270.

Sambridge, M., 1999a. Geophysical inversion with a neighborhood algorithm: I, searching a parameter space. *Geophysical Journal International*, **138**, 479-494.

Sambridge, M., 1999b. Geophysical inversion with a neighborhood algorithm: II, appraising the ensemble. *Geophysical Journal International*, **138**, 727-746.

Samier, P., Onaisi, A. & Fontaine, G., 2003. Coupled analysis of geomechanics and fluid flow in reservoir simulation, *SPE Reservoir simulation symposium, Houston, USA*, 3-5 Febuary, SPE 79698.

Sarout, J. & Guéguen, Y., 2008. Anisotropy of elastic wave velocities in deformed shales: Part 2 - Modelling results. *Geophysics*, **73**, 91-103.

Sarout, J., Esteban, L., Delle Piane, C., Maney, B. & Dewhurst, D.N., 2015. Elastic anisotropy of Opalinus Clay under variable saturation and triaxial stress. *Geophysical Journal International*, **198**, 1662-1682.

Sarout, J., Delle Piane, C., Nadri, D., Esteban, L. & Dewhurst, D.N., 2015. A robust experimental determination of Thomsen's δ parameter. *Geophysics*, **80**, 19-24.

Sayers, C.M. & Kachanov, M., 1995. Microcrack induced elastic wave anisotropy of brittle rocks. *Journal of Geophysical Research*, **100**, 4149-4156.

Sayers, C.M., 2002. Stress-dependent elastic anisotropy of sandstones. *Geophysical Prospecting*, **50**, 85-95.

Schneider, F., Potdevin, J.L., Wolf, S. & Faille, I., 1996. Mechanical and chemical compaction model for sedimentary basin simulators. *Tectonophysics*, **263**(1), 307-317.

Schoenberg, M. & Sayers, C.M., 1995. Seismic anisotropy of fractured rock. *Geophysics*, **60**, 204-211.

Schön, J.H., 1996. Physical properties of rocks: Fundamentals and principles of petrophysics. *Handbook of Geophysical Exploration: Seismic Exploration*, Elsevier, London, 583.

Schubnel, A., & Gueguen, Y., 2003). Dispersion and anisotropy of elastic waves in cracked rocks. *Journal of Geophysical Research*, **108**(B2), ESE16.1-ESE16.15.

Settari, A. & Walters, D.A., 2001. Advances in coupled geomechanical and reservoir modeling with applications to reservoir compaction. *Spe Journal*, **6**(3), 334-342.

Shapiro, S., 2003. Elastic piezosensitivity of porous and fractured rocks. *Geophysics*, **68**, 482-486.

Shapiro, S. & Kaselow, A., 2005. Porosity and elastic anisotropy of rocks under tectonic stress and pore-pressure changes. *Geophysics*, **70**(5), N27-N38.

Simmons, G. & Brace, W., 1965. Comparison of static and dynamic measurements of compressibility of rocks. *Journal of Geophysical Research*, **70**, 5649-5656.

Sinha, B.K. & Plona, T.J., 2001. Wave propagation in rocks with elastic-plastic deformations. *Geophysics*, **66**(3), 772-785.

Slagstad, T., Barróre, C., Davidsen, B., & Ramstad, R.K., 2008. Petrophysical and thermal properties of pre-Devonian basement rocks on the Norwegian continental margin. *Geological survey of Norway Bulletin*, **448**, 1-6.

Sobol, I., 1990. Sensitivity analysis for non-linear mathematical models. *Mathematical modelling and computational experiment*, **1**, 407-424.

Spear, R.C. & Hornberger, G.M., 1980. Eutrophication in peel inlet II. Identification of critical uncertainties via generalized sensitivity analysis. *Water Research*, **14**(1), 43-49.

Staples, R., Stevens, T., Leoutre, E., Jolley, S. & Marshall, J., 2005. 4D seismic history matching - the reality. *67th EAGE Conference and Exhibition, Madrid.*

Staples, R., Ita, J., Nash, R., Hague, P. & Burrell, R., 2007. Using 4D seismic data and geomechanical modelling to understand pressure depletion in HPHT fields of the Central North Sea. *69th EAGE Conference and Exhibition*, London, UK.

Sulak, A.M. & Danielsen, J., 1988. Reservoir aspects of Ekofisk subsidence. *Offshore Technology Conference*, 709-716.

Tarantola, S., Giglioli, N., Jesinghaus, J. & Saltelli, A., 2002. Can global sensitivity analysis steer the implementation of models for environmental assessments and decision-making? *Stochastic Environmental Research and Risk Assessment*, **16**(1), 63-76.

Tarantola, A., 2005. *Inverse problem theory and methods for model parameter estimation.* Siam.

Thomsen, L., 1986. Weak elastic anisotropy. *Geophysics*, **51**(10), 1954-1966.

Thurston, R.N. & Brugger, K., 1964. Third-order elastic constants and the velocity of small amplitude elastic waves in homogeneously stressed media. *Physical Review*, **133**(6A), A1604-A1610.

Tod, S.R., 2002. The effects of stress and fluid pressure on the anisotropy of interconnected cracks. *Geophysical Journal International*, **70**(5), N27-N38.

Tura, A., Barker, T., Cattermole, P., Collins, C., Davis, J., Hatchell, P., Koster, K., Schutjens, P. & Wills, P., 2005. Monitoring primary depletion reservoirs using amplitudes and time shifts from high-repeat seismic surveys. *The Leading Edge*, **24**(12), 1214-1221.

van Ditzhuijzen, P.J.D., Berhad, S.S. & de Waal, J.A., 1984. Reservoir compaction and surface subsidence in the Central Luconia gas bearing carbonates. *5th offshore South East Asia Conference*, Singapore, 4-27.

Verdon, J., Angus, D.A., Kendall, J.M. & Hall, S., 2008. The effects of microstructure and nonlinear stress on anisotropic seismic velocities. *Geophysics*, **73**(4), D41-D51.

Verdon, J.P. & Wüstefeld, A., 2013. Measurement of the normal/tangential fracture compliance ratio (Z_N/Z_T) during hydraulic fracture stimulation using S-wave splitting data. *Geophysical Prospecting*, **61**, 461-475.

Vernik, L., Bruno, M. & Bovberg, C., 1993. Empirical relations between compressive strength and porosity of siliciclastic rocks. *International journal of rock mechanics and mining sciences & geomechanics abstracts*, **30**(7), 677-680.

Vernon, I. & Goldstein, M., 2009. Bayes linear analysis of imprecision in computer models, with application to understanding galaxy formation. *6th international symposium on imprecise probability: Theories and applications*, Durham, UK.

Vernon, I., Goldstein, M. & Bower, R.G., 2010. Galaxy formation: a Bayesian uncertainty analysis. *Bayesian Analysis*, **5**(4), 619-669.

Vernon, I., Liu, J., Goldstein, M., Rowe, J., Topping, J. & Lindsey, K., 2016. Bayesian uncertainty analysis for complex systems biology models: emulation, global parameter searches and evaluation of gene functions. *arXiv preprint arXiv:1607.06358*.

Vudovich, A., Chin, L.V. & Morgan, D.R., 1989. Casing deformation in Ekofisk. *Journal of Petroleum Technology*, 729-734.

Wines, D., 2016. A comparison of slope stability analyses in two and three dimensions. *The journal of the Southern African Institute of Mining and Metallurgy*, **116**, 399-406.

Wiprut, D. & Zoback, M.D., 2000. Fault reactivation and fluid flow along a previously dormant normal fault in the northern North Sea. *Geology*, **28**(7), 595-598.

Wookey J., 2012. Direct probabilistic inversion of shear wave data for seismic anisotropy. *Geophysical Journal International*, **189**(2), 1025-1037.

Wright, W.A., 1967. Prediction of bulk moduli and pressure-volume-temperature data for petroleum oils. *Asle Transaction*, **10**(4), 349-356.

Yousef, B. & Angus, D.A., 2016. When do fractured media become seismically anisotropic? Some implications on quantifying fracture properties. *Earth and Planetary Science Letters*, **444**, 150-159.

Zang, J. & Reederm, R.J., 1999. Comparative compressibilities of calcite-structure carbonates: Deviations from empirical relations. *American Mineralogist*, **84**(5-6), 861-870.

Zimmerman, R.W., Somerton, W.H. & King, M.S., 1986. Compressibility of porous rocks. *Journal of Geophysical Research*, **91**, 12765-12777.

Zoback, M. D., 2010, *Reservoir Geomechanics*. Cambridge University Press, Cambridge, 449.